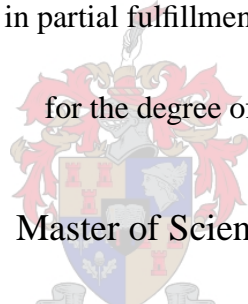


A characterization of beam shaping devices and a  
tunable Raman laser

by

Anton du Plessis

Thesis presented in partial fulfillment of the requirements



for the degree of

Master of Science

at the University of Stellenbosch

Supervisors:

Dr. E.G. Rohwer

Prof. H.M. von Bergmann

April 2003

## Declaration

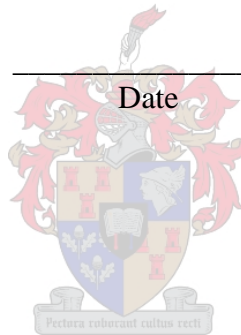
I, the undersigned, hereby declare that the work contained in this thesis is my own original work and that I have not previously in its entirety or in part submitted it at any university for a degree.

---

Signature

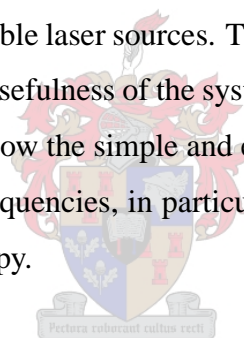
---

Date



# Abstract

The efficient manipulation of various nonlinear optical processes frequently requires the shaping of the laser beams used for these processes. Three beam shaping techniques were investigated in this thesis. The focussing of Gaussian laser beams was investigated analytically, in order to efficiently manipulate the focussed beam characteristics. The beam-shaping characteristics of a diffractive optical element (DOE) was investigated numerically, which illustrates the beam-shaping capability of the DOE, and identifies the critical parameters in experimental situations. The use of a waveguide as beam shaping device was investigated analytically and experimentally, and characterized for use with the available tunable laser sources. A Raman laser, or Raman shifter, employs stimulated vibrational Raman scattering to generate laser radiation at shifted frequencies. The waveguide was successfully applied as a beam shaping device in the Raman laser system, for optimisation of the process. The Raman laser system was investigated experimentally and characterized for use with the available tunable laser sources. The successful generation of laser radiation at shifted frequencies illustrates the usefulness of the system for generating tunable red-shifted frequencies. The results of this work allow the simple and efficient application of the Raman laser to generate laser radiation at shifted frequencies, in particular tunable infrared laser radiation which is desirable for molecular spectroscopy.



# Opsomming

Nie-liniêre optiese prosesse kan meer effektief benut word deur die vervorming van die laserbundels wat gebruik word in die prosesse. In hierdie tesis word drie laserbundel-vervormings tegnieke ondersoek. Die fokussing van Gaussiese laserbundels word analities ondersoek, om die gefokusseerde bundel se eienskappe effektief te manipuleer. Die bundel-vervormings eienskappe van 'n diffraktiewe optiese element word numeries ondersoek, wat die effektiwiteit van die bundelvervorming en die sensitiewe parameters in die sisteem uitwys. Die gebruik van 'n golfgeleier as 'n bundelvervormings tegniek word ook analities en eksperimenteel ondersoek, en gekarakteriseer vir gebruik met die gegewe golflengte-verstelbare laser sisteme. 'n Raman laser, wat gestimuleerde vibrasionele Raman verstrooiing gebruik om laser lig te genereer by Stokes-verskuifde frekwensies, word ondersoek. Die golfgeleier word effektief gebruik as 'n bundelvervormings tegniek in die Raman laser, om die bogenoemde nie-liniêre proses te optimeer. Die Raman laser was eksperimenteel ondersoek en gekarakteriseer vir gebruik met die gegewe golflengte-verstelbare lasers. Laser lig by verskuifde golflengtes is suksesvol gegenereer, wat die bruikbaarheid van die sisteem illustreer. Van belang is spesifiek verstelbare infrarooi laser lig, wat gebruik kan word in die laser-spektroskopie van molekules. Die resultate van hierdie werk lei tot die eenvoudige en effektiewe gebruik van die Raman laser, om langer golflengtes in die infrarooi gebied te genereer met 'n gegewe laser in die sigbare gebied.



# Acknowledgements

I would like to thank the following people:

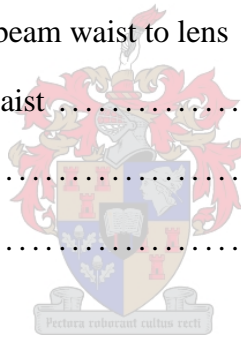
- Dr. E.G. Rohwer for his excellent supervision and guidance of this work and for countless discussions which have contributed to the success of this project.
- Prof. H.M. von Bergmann for his supervision of this project.
- Dr. A. Forbes for providing opportunities for collaboration, which led to interesting and fruitful research.
- Prof. P.E. Walters for many discussions about the experimental measurements.
- Mr. U.G.K. Deutschländer for his help with the practical aspects of the work.
- All my colleagues, in particular Christine, Torsten and Pieter, whose interest in my work was inspiring and helpful.
- The members of the Laser Research Institute, who were always willing to listen to my talks.
- My parents, for their understanding and support.
- Elize for a great amount of love, motivation and support.



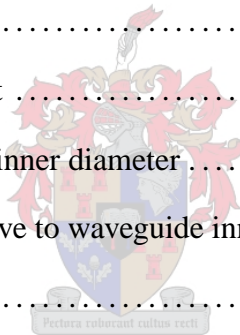
My studies were partially funded by the National Research Foundation (NRF) and by De-fencetek. My vacation work at Scientific Development and Integration (SDI) during 2001 played a large role in my development. The lasers used in this project were made available by the National Laser Centre (NLC). The Raman cell was sponsored by SDI.

# Contents

<b>Introduction</b> .....	<b>1</b>
<b>1 Focussing</b> .....	<b>3</b>
1.1 Introduction .....	3
1.2 Theoretical investigation .....	5
1.3 Experimental investigation .....	8
1.4 Parameter sensitivity testing .....	11
1.4.1 Wavelength .....	12
1.4.2 Distance from initial beam waist to lens .....	13
1.4.3 Size of initial beam waist .....	14
1.4.4 Lens focal length .....	15
1.5 Conclusions .....	16
<b>2 Diffractive optical elements</b> .....	<b>17</b>
2.1 Introduction .....	17
2.2 Numerical model .....	18
2.3 Modelling of a diffractive optical element .....	22
2.4 Beam shaping design .....	25
2.5 Parameter sensitivity testing .....	28
2.5.1 Wavelength .....	28
2.5.2 Non-Gaussian initial beam .....	30



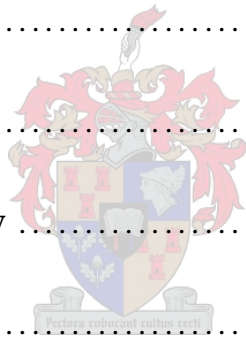
2.5.3	Initial beam size .....	33
2.5.4	Initial beam phase .....	35
2.5.5	Initial Gaussian beam offset axially.....	37
2.5.6	Radial offset .....	39
2.5.7	Focal length of lens .....	42
2.6	Conclusions .....	44
<b>3</b>	<b>Waveguides .....</b>	<b>45</b>
3.1	Introduction .....	45
3.2	Injection requirements .....	46
3.2.1	Incident beam transverse mode .....	47
3.2.2	Directional alignment .....	48
3.2.3	Beam waist alignment .....	50
3.2.4	Choice of waveguide inner diameter .....	50
3.2.5	Beam waist size relative to waveguide inner diameter.....	51
3.2.6	Experimental method .....	52
3.3	Waveguide propagation .....	54
3.4	Parameter sensitivity testing .....	57
3.4.1	Length of waveguide .....	57
3.4.2	Radius of waveguide.....	58
3.4.3	Wavelength of radiation.....	59
3.4.4	Index of refraction .....	60
3.4.5	Conclusions .....	61
3.5	Experimental investigation .....	62
3.5.1	Introduction .....	62
3.5.2	Dye laser.....	62



3.5.3	Optically pumped parametric oscillator .....	67
<b>4</b>	<b>Stimulated Raman Scattering .....</b>	<b>68</b>
4.1	Introduction .....	68
4.2	Theoretical description .....	69
4.2.1	First-order Stokes formation .....	69
4.2.2	The Raman gain coefficient .....	71
4.2.3	Higher-order Stokes formation .....	72
4.2.4	Four-wave mixing effects .....	73
4.2.5	Threshold .....	74
4.3	Design of the Raman laser .....	75
4.3.1	Beam shaping .....	75
4.3.2	Gaseous medium .....	75
4.3.3	Wavelength range .....	76
4.3.4	Competition between Stokes orders .....	77
<b>5</b>	<b>Experimental characterization .....</b>	<b>78</b>
5.1	The Raman laser system .....	78
5.2	Dye laser at 440nm .....	79
5.2.1	Experimental conditions .....	79
5.2.2	Observation of SRS .....	79
5.2.3	Pressure dependence .....	81
5.2.4	Temporal dependence .....	84
5.3	Dye laser at 540nm .....	86
5.3.1	Experimental conditions .....	86
5.3.2	Observation of SRS .....	86
5.3.3	Pressure dependence .....	88



5.3.4	Threshold investigation .....	89
5.4	Optically pumped parametric oscillator .....	91
5.4.1	Experimental conditions .....	91
5.4.2	Tunability and energy measurements .....	92
5.4.3	Observation of SRS .....	93
5.4.4	Low Stokes output .....	94
5.5	Nd:YAG at 355 nm .....	95
5.5.1	Experimental conditions .....	95
5.5.2	Pressure dependence .....	97
5.6	Raman laser conclusions .....	100
<b>Conclusions .....</b>		<b>102</b>
<b>Bibliography .....</b>		<b>103</b>
<b>A Gaussian beam terminology .....</b>		<b>105</b>
<b>B Scanning slit measurement .....</b>		<b>107</b>
<b>C Phase profile calculation .....</b>		<b>108</b>
<b>D Use of Schott cutoff filters .....</b>		<b>109</b>



# List of Figures

Figure 1.1	Illustration of the parameters in the Gaussian beam focussing situation. ....	5
Figure 1.2	Measurement of the transverse intensity profile of the beam at the laser exit aperture - experimental data points and Gaussian fit. ....	9
Figure 1.3	Measurement of the transverse intensity profile of the focussed beam waist - experimental data points and Gaussian fit. ....	10
Figure 1.4	Calculations of the focussed waist size (left axis / solid line) and the distance of this focus from the lens (right axis / dashed line) as a function of wavelength. This investigation is for $w_{01} = 0.3740$ mm, $z_1 = 0.5$ m, $f = 0.3$ m. ....	12
Figure 1.5	Calculations of the focussed waist size (left axis / solid line) and the distance of this focus from the lens (right axis / dashed line) as a function of initial distance $z_1$ . This investigation is for $w_{01} = 0.3740$ mm, $f = 0.3$ m, $\lambda = 632.8$ nm. ....	13
Figure 1.6	Calculations of the focussed waist size (left axis / solid line) and the distance of this focus from the lens (right axis / dashed line) as a function of initial beam waist size $w_{01}$ . This investigation is for $z_1 = 0.5$ m, $f = 0.3$ m, $\lambda = 632.8$ nm. ....	14
Figure 1.7	Calculations of the focussed waist size (left axis / solid line) and the distance of this focus from the lens (right axis / dashed line) as a function of lens focal length $f$ . This investigation is for $w_{01} = 0.3740$ mm, $z_1 = 0.5$ m, $\lambda = 632.8$ nm. ....	15
Figure 2.1	Propagation calculation with the Rayleigh-Sommerfeld diffraction formula. The contribution of a single point in the initial field $U_0(x_0, y_0)$ to a single point in the final field $U_1(x_1, y_1)$ is illustrated. ....	18
Figure 2.2	The phasor notation for complex fields ....	19
Figure 2.3	Simple wedge-shaped window system. The propagation direction is chosen left to right. ....	22
Figure 2.4	Schematic illustration of the cross-section of a spherical lens. ....	23
Figure 2.5	Schematic illustration of the cross-section of a diffractive optical element. ....	23
Figure 2.6	A typical binary DOE profile: the height is given in $\mu\text{m}$ and the radius in mm. ...	24
Figure 2.7	Transmission efficiency of a typical DOE as a function of the number of ablated levels. ....	24
Figure 2.8	The DOE design: initial Gaussian intensity profile and desired super-Gaussian intensity profile. ....	25

Figure 2.9	Comparison between the design profile and the numerically calculated profile. .	26
Figure 2.10	Propagation of the beam between 1 and 3 m after the DOE, demonstrating the ideal beam shaping situation with the flat-top profile near 2 m. ....	27
Figure 2.11	The flat-top intensity profile of different laser wavelengths at the focal distance.	29
Figure 2.12	Intensity profiles of the incident beam for different mixing factors. ....	30
Figure 2.13	Intensity profiles of the final beam at the focal distance for different mixing factors. ....	31
Figure 2.14	The beam shaping propagation of a mixed beam of mixing factor 10. ....	32
Figure 2.15	The beam shaping propagation of an initial beam size of 6 mm. ....	34
Figure 2.16	The beam shaping propagation of an initial beam size of 8 mm. ....	34
Figure 2.17	Schematic illustration of the phase profiles of a Gaussian beam at different positions around the waist position. ....	35
Figure 2.18	Intensity profiles of the final beam at the focal distance for different phase mismatch values. ....	36
Figure 2.19	Intensity profiles of the final beam at the focal distance for different axial offset values. ....	37
Figure 2.20	The beam shaping propagation due to an axial offset of +1 m: beam waist position 1 m before the DOE. ....	38
Figure 2.21	Three-dimensional representation of the desired intensity profile in the ideal case. ....	39
Figure 2.22	Three-dimensional representation of the intensity profile due to a radial offset of the initial beam: $\Delta x = 1.4$ mm. ....	39
Figure 2.23	The beam shaping propagation of a radially offset beam, offset in the $x$ -direction: $\Delta x = 0.35$ mm. ....	40
Figure 2.24	The peak deviation of the final intensity profile at the focal distance, as a function of radial offset amount. ....	41
Figure 2.25	Illustration of the effect of the final intensity profile due to different lenses used in conjunction with the DOE: the different profiles are at the focal distance of each lens. ....	42
Figure 2.26	Quantification of the final intensity profile (flat-top intensity peak - hollow square points; beam radius - solid circular points) due to different lenses used in conjunction with the DOE: the different profiles are at the focal distance of each lens. ....	43
Figure 3.1	Schematic illustration of ideal injection into the waveguide cavity. ....	46

Figure 3.2	Transverse intensity profile of Helium-Neon laser after waveguide transmission: transmission factor of 80%. The line was drawn to enhance the visual appearance. ....	47
Figure 3.3	Photograph of the mode pattern of the waveguide-transmitted Helium-Neon laser beam in good alignment. ....	49
Figure 3.4	Photograph of the mode pattern of the waveguide-transmitted Helium-Neon laser beam with slight misalignment. ....	49
Figure 3.5	Schematic illustration of injection into the waveguide: focussed waist size too large. ....	51
Figure 3.6	Schematic illustration of injection into the waveguide: focussed waist size too small. ....	51
Figure 3.7	Schematic illustration of injection into the waveguide: focussed waist size optimal. ....	52
Figure 3.8	Schematic illustration of ray propagation in a waveguide. ....	54
Figure 3.9	The theoretical transmission of a typical waveguide as a function of focussed waist radius. ....	56
Figure 3.10	The transmission as a function of focussed beam radius, for different waveguide lengths: 0.1, 1, 10 m. ....	57
Figure 3.11	The transmission as a function of focussed beam radius, for different waveguide radii: dimensions of typical glass capillary tubes were used. ....	58
Figure 3.12	The transmission as a function of focussed beam radius for different wavelengths. ....	59
Figure 3.13	The transmission as a function of focussed beam radius for different indices of refraction. ....	60
Figure 3.14	Measured intensity profile of dye laser after the Raman laser configuration, including windows and waveguide, total transmission $\sim 60\%$ . ....	64
Figure 3.15	Photograph of the mode pattern of dye laser after the Raman laser configuration, including windows and waveguide, total transmission $\sim 60\%$ . ....	64
Figure 3.16	Transmission of empty waveguide as a function of incident pulse energy, using the dye laser at 540 nm and 10 Hz repetition rate. ....	65
Figure 3.17	Transmission of empty waveguide as a function of repetition rate, using the dye laser at 540 nm and 2.1 mJ incident pulse energy. ....	66
Figure 3.18	Photograph of the beam spot of the OPPO laser tuned to $\lambda = 440$ nm, illustrating the poor beam quality. ....	67

Figure 4.1	Quantum-transition diagram representing Stokes-shifted Raman scattering.....	70
Figure 4.2	Quantum-transition diagram representing three orders Stokes-shifted Raman scattering.....	72
Figure 4.3	Schematic illustration of the frequency-shifting process of three orders of Stokes formation.....	73
Figure 4.4	Illustration of the wavelength regions attainable with the dye laser at around 440 nm, including the corresponding tunability ranges.....	76
Figure 4.5	Schematic illustration of two methods of reaching a certain wavelength region with the Raman laser, by first or second Stokes formation.....	77
Figure 5.1	Schematic illustration of the experimental setup.....	78
Figure 5.2	Measured intensity profile of the second Stokes radiation at 694 nm.....	80
Figure 5.3	Photograph of the mode pattern of the second Stokes radiation at 694 nm.....	80
Figure 5.4	Measured Stokes pulse energy as a function of hydrogen pressure.....	81
Figure 5.5	Measured first Stokes pulse energy as a function of pressure for two pump pulse energies.....	82
Figure 5.6	Measured second (and possibly third) Stokes pulse energy as a function of pressure for three pump pulse energies.....	83
Figure 5.7	Measurements of the partially depleted pump pulse, the corresponding first Stokes pulse and the second (and possibly third) Stokes pulse.....	84
Figure 5.8	Measurements of the pump pulse with and without hydrogen, illustrating the partial depletion of the pump pulse due to SRS.....	85
Figure 5.9	Photograph of first Stokes formation at 696 nm, due to a dye laser pump at 540 nm.....	87
Figure 5.10	Measurements of the first Stokes pulse energy as a function of pressure, for different incident dye laser energies.....	88
Figure 5.11	Measurements of the Stokes pulse energy as a function of incident dye laser pulse energy, illustrating the effective threshold of SRS. The two measurements correspond to different alignment situations.....	89
Figure 5.12	Measured pulse-to-pulse deviation as a function of incident energy (solid circular points), illustrating unstable operation near the threshold. The corresponding Stokes energy is also shown (hollow square points).....	90
Figure 5.13	Measurements of the OPPO pulse energy as a function of wavelength: the blue, green and red indicated regions correspond to the resonator windows used.....	92

Figure 5.14 Measurements of the temporal dependence of the first Stokes formation at 799 nm, using the OPPO as pump laser at 600 nm..... 93

Figure 5.15 Photograph of Raman laser operation using the frequency-tripled Nd:YAG. Three orders of Stokes are visible, as well as the fluorescence of the 355 nm pump. .... 96

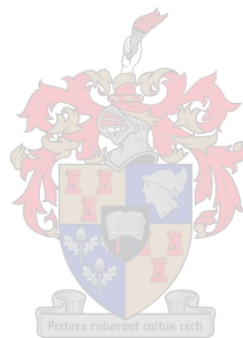
Figure 5.16 Measured Stokes energy as a function of pressure: 1 mJ incident energy. .... 97

Figure 5.17 Measured Stokes energy as a function of pressure: 1.5 mJ incident energy. .... 98

Figure 5.18 Measured Stokes energy as a function of pressure: 3 mJ incident energy. .... 99

Figure 5.19 Illustration of Gaussian intensity profile and the beam size  $w$ ..... 105

Figure 5.20 Schematic illustration of the Gaussian beam parameters. .... 106



# Introduction

All nonlinear optical processes are highly intensity-dependent. This dependence does not, by definition, have a physical threshold value, but does have an *effective threshold*<sup>1</sup> in practical situations. The efficient manipulation of nonlinear processes requires, amongst other things, the shaping of the laser beams used in the process. The laser beam's transverse intensity profile, compared to this effective threshold value, determines the efficiency of the process.

If the laser beam to be used has a peak intensity less than the effective threshold value, no nonlinear effects will be observed. In this case, one possibility is to focus the beam with a lens such that the transverse profile becomes narrower and the peak intensity higher, until the threshold value is reached. In Chapter 1, the effect of various parameters on the focussed beam size is investigated. Laser beam focussing is applied in many optical situations, and one example of a nonlinear process which employs focussing is sum frequency generation in a heatpipe system.

If the laser beam to be used has a peak intensity above the effective threshold, but a uniform efficiency of the nonlinear process is required transversely across the beam, a flat-top beam profile may be used. Such a flat-top beam profile can be obtained very efficiently by using a diffractive optical element (DOE) to transform a Gaussian beam into a super-Gaussian, or flat-top beam. The characteristics of such a DOE, which has been designed and manufactured, was investigated numerically for collaborators in industry. This is discussed in Chapter 2. The DOE under consideration will be used to generate a flat-top beam for the uniform irradiation of a gaseous medium. The process involved is a form of selective photochemistry through multiphoton dissociation.

Another popular beam-shaping technique is the use of a waveguide: the laser beam is focussed into a waveguide, in which the high intensity focus region is maintained over the entire length of the waveguide, through low-loss waveguide propagation. This is the subject of Chapter 3. This method of beam shaping was also experimentally characterized for use with the available tunable laser sources. The reason for this investigation is the use of the waveguide as beam shaping device in the Raman laser: the process involved is stimulated Raman scattering.

The beam shaping techniques mentioned above were investigated analytically, numerically and experimentally. Since efficient use of the waveguide requires optimal focussing characteristics, the results of the focussing investigation could be used to optimise the use of the waveguides. The waveguides were characterized and subsequently successfully applied in the Raman laser system.

---

<sup>1</sup> This is discussed in more detail in section 4.2.5.

The Raman laser system is a simple, cost-effective solution for generating laser radiation at shifted wavelengths, with a given pump laser system. This is particularly desirable for applications such as molecular spectroscopy, due to the shortage of tunable, pulsed laser sources in the near IR. A nonlinear process, namely stimulated Raman scattering, is utilized to generate laser radiation at shifted wavelengths. The nonlinear medium in this case was molecular hydrogen, and specifically vibrational Raman scattering of the  $Q(1)$  transition was employed. The gaseous medium allows the use of the hollow waveguide as a beam shaping device. The theoretical description of the stimulated Raman scattering process can be found in Chapter 4.

The goal of the Raman laser investigation was to characterize the system, for use as a tunable laser source in the near IR, with the given tunable laser sources and experimental resources. Successful wavelength conversion was demonstrated with the various pump laser systems and the effect of various parameters on the output was investigated. The experimental challenges in using each of the pump laser systems were identified. The typical operating characteristics, using the given pump laser systems, were quantified. These results are contained in Chapter 5. The results of this work pave the way for the successful and simple application of the system as a tunable laser source in the near IR.



# Chapter 1

## Focussing

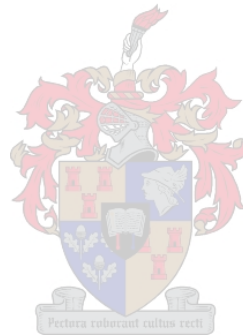
### 1.1 Introduction

The focussing of a Gaussian laser beam by a thin lens is the simplest and most well-known beam shaping technique. A complete description of Gaussian laser beam focussing can be found in most laser or optics textbooks, and will not be repeated here. Instead, the necessary terminology is presented in Appendix A.

The importance of a good understanding of Gaussian beam focussing in the context of this thesis stems from the fact that different laser beams needed to be focussed to a certain waist size, for optimal injection into the waveguide of the Raman laser. Different waveguides were investigated, which implies different required focussed waist sizes. The usual method of solving this problem is to calculate the position at which a certain lens should be placed, in order to generate the required focussed beam waist size from a given initial waist size. This is called mode matching and is described in detail in [1]. However, this method is unsuitable in this case due to two reasons. The first reason is the fact that the original laser beam waist size and position was not known accurately, and differed for the different laser beams used. The second reason is a practical one - the quality of the injection into the waveguide can be judged extremely well by measuring the transmission of the empty waveguide. This method involves changing certain parameters which increase or decrease the focussed waist size. In this way, optimal injection may be achieved. The waveguide characteristics are discussed in Chapter 3.

The knowledge of the effect induced on the focussed waist size, by small changes of each of the different focussing parameters, is thus required. Theoretically, suitable relations were derived from the Gaussian Beam Solution of the Paraxial Wave Equation and the ABCD law for Gaussian beams [2]. A typical experimental focussing system for focussing into the waveguides used in this thesis was investigated experimentally. The applicable parameter sensitivity tests, using the above-mentioned theoretical relations, were done for the typical focussing situation, in order to apply the same knowledge to the waveguide problem.

Besides the advantage of a more efficient focussing setup for the waveguide, this knowledge may also be applied to a multitude of different situations. Two simple examples are: Raman laser operation without the waveguide and heatpipe system operation, of which both employ focussing into the respective nonlinear media.



## 1.2 Theoretical investigation

This theoretical investigation of Gaussian laser beam focussing by a thin lens involves the derivation of suitable relations, from the Gaussian Beam Solution of the Paraxial Wave Equation and the ABCD law for Gaussian beams [2], in order to investigate the effect on the focussed beam size and position of this focus, as a function of the various other parameters. The various parameters of interest in the Gaussian beam focussing situation are the following:

1. Wavelength of laser radiation  $\lambda$
2. Size of initial beam waist  $w_{01}$
3. Distance of lens from initial waist position  $z_1$
4. Lens focal length  $f$
5. Distance to new waist position  $z_2$
6. Size of new beam waist  $w_{02}$

These parameters are illustrated in Figure 1.1. The complex beam parameters of interest ( $q_1, q_2, q_3, q_4$ ), which will be discussed later, are also indicated.

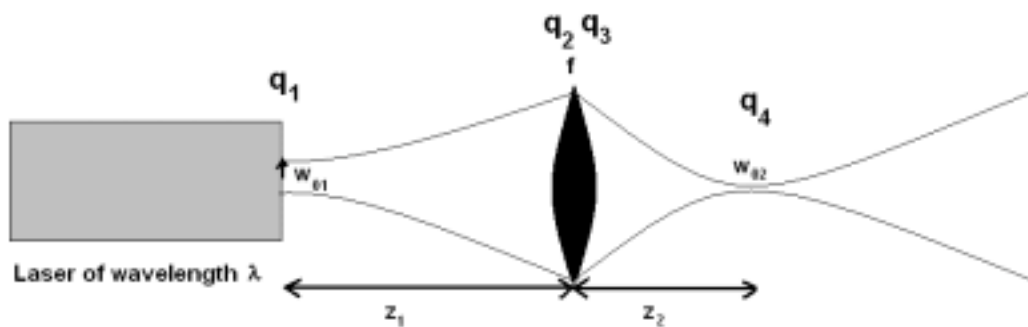


Figure 1.1: Illustration of the parameters in the Gaussian beam focussing situation.

In experimental situations, there are many possible permutations of this beam propagation situation, depending on which parameters are known and which need to be calculated. In this theoretical investigation, it is assumed that the laser wavelength  $\lambda$ , the initial beam waist  $w_{01}$ , the first distance  $z_1$  and the lens focal length  $f$  are all known. The new beam waist size  $w_{02}$  and the second distance  $z_2$  can then be calculated. This choice allows for parameter sensitivity testing - in order to investigate the effect of small changes of the known parameters on the unknown parameters. As has been mentioned before, the knowledge of the qualitative effect of changes of the various parameters on the new beam waist size can then be applied to an experimental situation.

The beam propagation problem can be solved by using the ABCD law for Gaussian beams. In this description, a complex beam parameter  $q$  is defined for every point in the beam path. The  $q$  parameters of interest in this derivation are illustrated in Figure 1.1. The general definition of the complex beam parameter  $q$  is given by:

$$\frac{1}{q} = \frac{1}{R} - \frac{i\lambda}{\pi w^2} \quad (1.1)$$

where

$R$  is the radius of curvature of the wavefront

$\lambda$  is the wavelength

$w$  is the beam size at the given position

By choosing the parameter at the initial beam waist as  $q_1$ , the parameter at the lens  $q_2$  can be calculated due to the free-space propagation of a distance  $z_1$ :

$$q_2 = q_1 + z_1 \quad (1.2)$$

The parameter  $q_3$ , due to the effect of the thin spherical lens, is given by:

$$\frac{1}{q_3} = \frac{1}{q_2} - \frac{1}{f} \quad (1.3)$$

Finally, parameter  $q_4$ , due to further propagation of the second distance  $z_2$ , is given by:

$$q_4 = q_3 + z_2 \quad (1.4)$$

Elimination of  $q_2$  and  $q_3$  from the Equations 1.2-1.4 yields the relation between  $q_1$  and  $q_4$  in terms of the distances  $z_1$  and  $z_2$ .

$$\begin{aligned} q_4 &= \frac{1}{\frac{1}{q_1+z_1} - \frac{1}{f}} + z_2 \\ &= \frac{q_1 f + z_1 f}{f - q_1 - z_1} + z_2 \\ (q_4 - z_2)(f - q_1 - z_1) &= q_1 f + z_1 f \end{aligned} \quad (1.5)$$

At the initial and final beam waist positions, the wavefront radius of curvature  $R = \infty$  and the parameters are given by:

$$q_1 = \frac{i\pi w_{01}^2}{\lambda} \quad (1.6)$$

$$q_4 = \frac{i\pi w_{02}^2}{\lambda} \quad (1.7)$$

Thus  $q_1$  and  $q_4$  are purely imaginary and  $f$ ,  $z_1$  and  $z_2$  are real. By grouping the real and imaginary parts in Equation 1.5, one obtains:

$$q_1 f - q_4 f - q_1 z_2 + z_1 q_4 = z_1 z_2 - z_1 f - z_2 f - q_1 q_4$$

and the left and right hand sides have to be zero. This leads to the following equations:

$$q_1 (f - z_2) - q_4 (f - z_1) = 0 \quad (1.8)$$

and

$$(f - z_1)(f - z_2) = f^2 + q_1 q_4 \quad (1.9)$$

The derivation up to this point can be found in [3]. Using these relations, equations will now be derived by which the focussed beam waist  $w_{02}$  and the distance from the lens to this focus  $z_2$  can be calculated, if the parameters  $\lambda$ ,  $w_{01}$ ,  $z_1$  and  $f$  are all known.

Equations 1.6 and 1.7 are substituted in Equation 1.8:

$$\begin{aligned} \frac{i\pi w_{01}^2}{\lambda} &= \frac{i\pi w_{02}^2 (f - z_1)}{\lambda \frac{S}{(f - z_2)}} \\ w_{02} &= w_{01} \frac{(f - z_2)}{(f - z_1)} \end{aligned} \quad (1.10)$$

Similarly, in Equation 1.9:

$$\begin{aligned}
 (f - z_1)(f - z_2) &= f^2 + \frac{i\pi w_{01}^2}{\lambda} \frac{i\pi w_{02}^2}{\lambda} \\
 z_2(z_1 - f) &= z_1 f - \frac{\pi^2 w_{01}^2 w_{02}^2}{\lambda^2} \\
 z_2 &= \frac{z_1 f - \frac{\pi^2 w_{01}^2 w_{02}^2}{\lambda^2}}{z_1 - f}
 \end{aligned} \tag{1.11}$$

Equation 1.10 can be rearranged to yield:

$$z_2 = f - (f - z_1) \frac{w_{02}}{w_{01}} \tag{1.12}$$

Equating the left hand sides of Equations 1.11 and 1.12 and solving for  $w_{02}$ :

$$\begin{aligned}
 \frac{z_1 f - \frac{\pi^2 w_{01}^2 w_{02}^2}{\lambda^2}}{z_1 - f} &= f - (f - z_1) \frac{w_{02}}{w_{01}} \\
 (z_1 - f) f + (z_1 - f)^2 \frac{w_{02}}{w_{01}} &= z_1 f - \frac{\pi^2 w_{01}^2 w_{02}^2}{\lambda^2} \\
 w_{02}^2 \frac{(z_1 - f)^2}{w_{01}^2} + \frac{\pi^2 w_{01}^2}{\lambda^2} &= f^2 \\
 w_{02} &= \frac{f}{\sqrt{\frac{(z_1 - f)^2}{w_{01}^2} + \frac{\pi^2 w_{01}^2}{\lambda^2}}}
 \end{aligned} \tag{1.13}$$

This gives the final beam waist  $w_{02}$  as a function of  $\lambda$ ,  $w_{01}$ ,  $z_1$  and  $f$ . Using this value for  $w_{02}$ , the distance of this waist position from the lens ( $z_2$ ) can be calculated using either Equation 1.11 or 1.12.

### 1.3 Experimental investigation

Focussing of a Gaussian laser beam was investigated experimentally, using a low power cw Helium-Neon laser, due to its low beam quality factor<sup>2</sup>. The experimental setup was identical to that of the previous section, with  $\lambda = 632.8 \times 10^{-9}$  m,  $z_1 = 0.500$  m and  $f = 0.30$  m.

The exact size and position of the laser beam's initial beam waist, which is inside the laser resonator, is unknown. An approximation was made to overcome this obstacle. The beam size was measured experimentally at the laser exit aperture and this was approximated as the position and size of the initial beam waist. In most cases of interest, this is a relatively good first approximation. The beam size at the new focus  $w_{02}$  was also measured experimentally. The

<sup>2</sup> A low beam quality factor refers to a good Gaussian character of the beam, refer to Appendix A.

position of this focus was determined by visual inspection of the beam spot size on paper, by moving the paper along the beam path. These experimental parameters were chosen to represent a typical focussing situation, which closely corresponds to the focussing setups used in the Raman laser. Many different focussing situations exist and all these cannot be dealt with here.

The measurements were taken with the scanning slit method. This measurement method is discussed in Appendix B. It is well known that this method of beam profile measurement is extremely simple, accurate and fast [4].

The measured transverse intensity profiles at the laser exit and at the new focus are given in Figures 1.2 and 1.3 respectively.

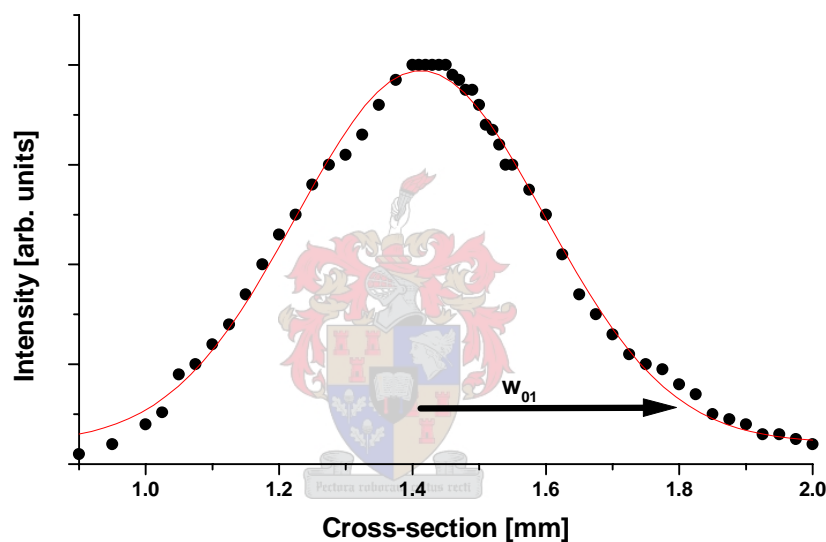


Figure 1.2: Measurement of the transverse intensity profile of the beam at the laser exit aperture - experimental data points and Gaussian fit.

The beam sizes of the measured profiles were found with a Gaussian fit procedure<sup>3</sup>. The initial beam waist was found to be:

$$(w_{01})_{measurement} = 0.37 \text{ mm}$$

<sup>3</sup> Microcal Origin 5.0. This Gaussian fit procedure gives the radius at  $\frac{1}{e^2}$  of the peak, corresponding to the beam size  $w$  as defined in Appendix A.

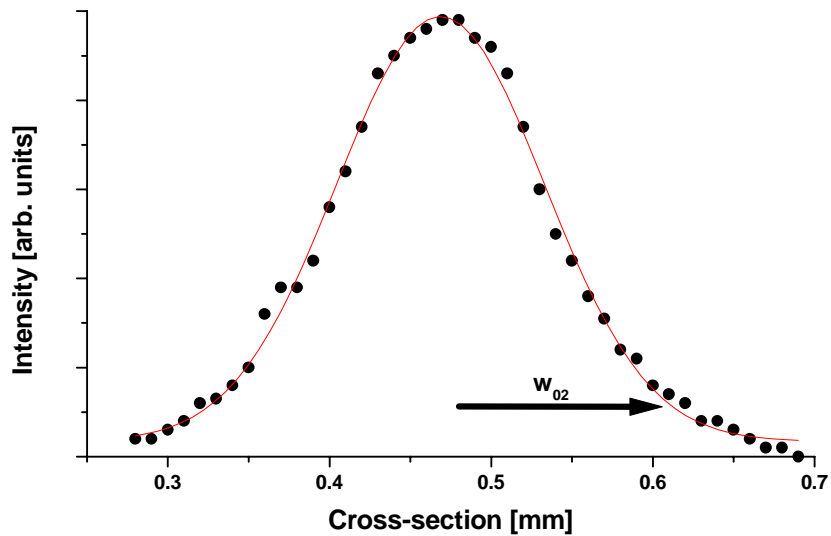


Figure 1.3: Measurement of the transverse intensity profile of the focussed beam waist - experimental data points and Gaussian fit.

Theoretical calculations using this value for  $w_{01}$ ,  $f = 0.30$  m,  $z_1 = 0.500$  m and  $\lambda = 632.8$  nm, Equations 1.13 and 1.12 yield:

$$w_{02} = 0.16 \text{ mm}$$

$$z_2 = 0.33 \text{ m}$$

The measured beam size at the focussed beam waist as given in Figure 1.3, by Gaussian fit, was found to be:

$$(w_{02})_{\text{measurement}} = 0.13 \text{ mm}$$

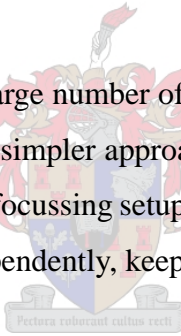
The experimental results compare favourably with the theoretical predictions, even though the mentioned approximations about the initial waist size and position were made. In reality, the initial beam waist size is smaller than that measured, due to divergence from the resonator. A smaller initial beam waist size results in a larger focussed waist size, which may be seen in Section 1.4.3. Thus, the realistic situation is such that the measured waist size should be smaller than that calculated, and thus good correspondence was found between theory and experiment.

## 1.4 Parameter sensitivity testing

The functional dependences of  $w_{02}$  and  $z_2$  on the known parameters, using Equations 1.13 and 1.12, allow parameter sensitivity testing to be done. This theoretical parameter sensitivity testing is limited by the analytical model derived above, which was derived in the Paraxial approximation. This requires the beam divergence to be small, and therefore the beam size should be much larger than a wavelength<sup>4</sup>. The parameters investigated were:

1. Wavelength  $\lambda$
2. Size of initial beam waist  $w_{01}$
3. Distance of lens from initial waist position  $z_1$
4. Lens focal length  $f$

For a complete investigation, a large number of permutations of variations of these parameters may be investigated. However, a simpler approach leads to sufficiently useful conclusions. This approach is to analyse the typical focussing setup investigated experimentally in the previous section, and vary each parameter independently, keeping the other parameters constant.



---

<sup>4</sup> Beam divergence  $\theta = \frac{\pi\lambda}{w_0}$ .

### 1.4.1 Wavelength

Since laser beams of different wavelengths were focussed into the waveguide of the Raman laser, knowledge of the effect induced on the focussed waist due to different wavelengths was required.

The dependence of the focussed beam waist size  $w_{02}$  and the position of this focus  $z_2$  on the wavelength  $\lambda$  is presented in Figure 1.4. The wavelength range investigated is up to 1000 nm. All the laser beams of interest in this thesis (for focussing) lie near the visible region, namely  $\sim 350 - 1000$  nm. The so-called geometrical optics limit is reached as  $\lambda \rightarrow 0$ , and this is demonstrated very clearly: the focussed waist size becomes infinitely small and the distance of this focus position from the lens becomes the focal length of the lens. The *experimental value* which is indicated shows the position on the focussed waist size function, for the Helium-Neon laser beam at  $\lambda = 632.8$  nm. This corresponds to the experimental investigation of the previous section. It can be seen that the focussed waist size dependence on wavelength is highly linear in the visible region, generating smaller waist sizes for shorter wavelengths. In the visible wavelength region, the distance of the focus from the lens as a function of wavelength is very nearly linear and decreases for shorter wavelengths.

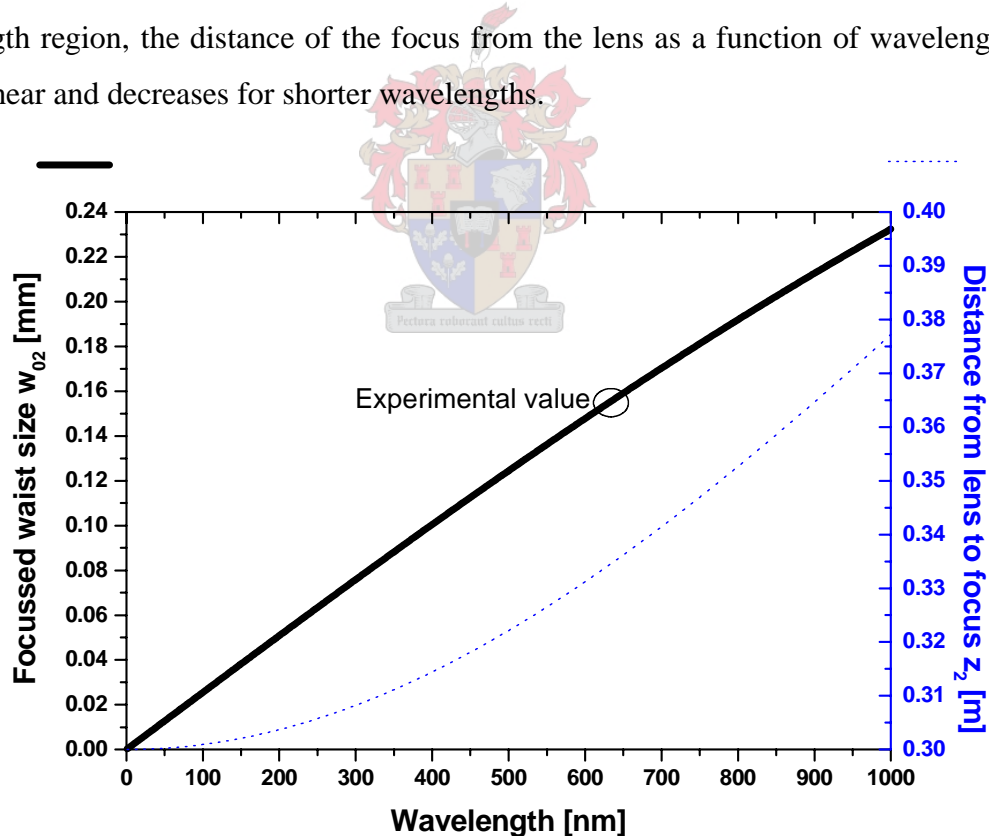


Figure 1.4: Calculations of the focussed waist size (left axis / solid line) and the distance of this focus from the lens (right axis / dashed line) as a function of wavelength. This investigation is for  $w_{01} = 0.3740$  mm,  $z_1 = 0.5$  m,  $f = 0.3$  m.

### 1.4.2 Distance from initial beam waist to lens

In typical focussing situations, the focussing lens may be placed at different distances from the laser. For this reason, the effect of a change of this distance  $z_1$  on the focussed waist size  $w_{02}$  and distance from the lens  $z_2$  is investigated. The effect is illustrated in Figure 1.5, with initial distances  $z_1$  up to 5 m, which is extreme in most experimental situations.

It can be seen that with the present choice of parameters corresponding to the indicated *experimental value*, the focussed waist size is near its maximum value. By decreasing the distance from the laser to the lens, a maximum focussed waist size is reached, after which this waist size decreases again slightly. It can be seen that a smaller focussed waist size may be obtained by increasing the initial distance of the lens from the laser, which is a result of practical value. However, a large increase in the initial distance eventually results in a larger incident beam on the lens, due to divergence. Since the lens has a finite size, a limit is reached which is called the *lens aperture limit* in this thesis. It can also be noted that the distance from the lens to the focus position  $z_2$  strives to the geometrical focus distance of 0.3 m as  $z_1$  is increased.

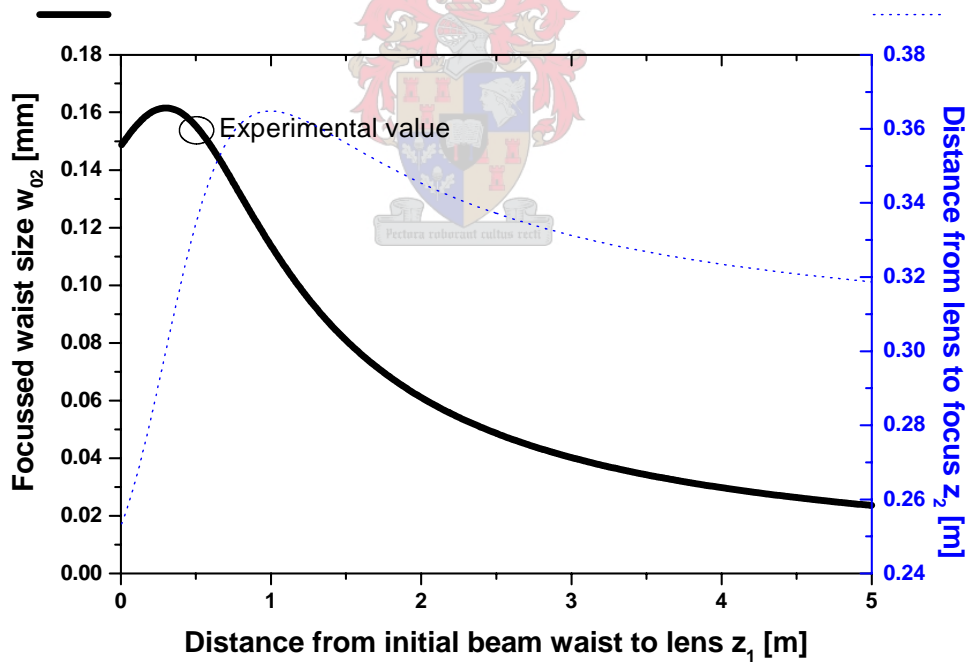


Figure 1.5: Calculations of the focussed waist size (left axis / solid line) and the distance of this focus from the lens (right axis / dashed line) as a function of initial distance  $z_1$ . This investigation is for  $w_{01} = 0.3740$  mm,  $f = 0.3$  m,  $\lambda = 632.8$  nm.

### 1.4.3 Size of initial beam waist

In general, lasers have different initial waist sizes, which are defined by the mirrors used in their resonator configurations. The effect of a different initial beam waist size is illustrated in Figure 1.6. In the region of the *experimental value*, which corresponds to the experimentally measured waist size of the Helium-Neon laser, a larger initial waist size results in a smaller focussed beam waist size, and vice versa. Since different lasers usually have different resonator parameters, the initial beam size of different laser beams usually differ. Therefore this functional dependence illustrates the effect of a different laser beam used in an identical focussing situation. The *lens aperture limit* is reached for very large and very small values of initial waist size, and again it can be seen that the distance  $z_2$  strives to the geometrical focus distance 0.3 m as the initial beam waist size increases. The initial beam waist size of  $w_{01} \rightarrow 0$  is the calculated value for an infinitely small initial waist size, which is beyond the *lens aperture limit* and not practically achievable in any laser resonator.

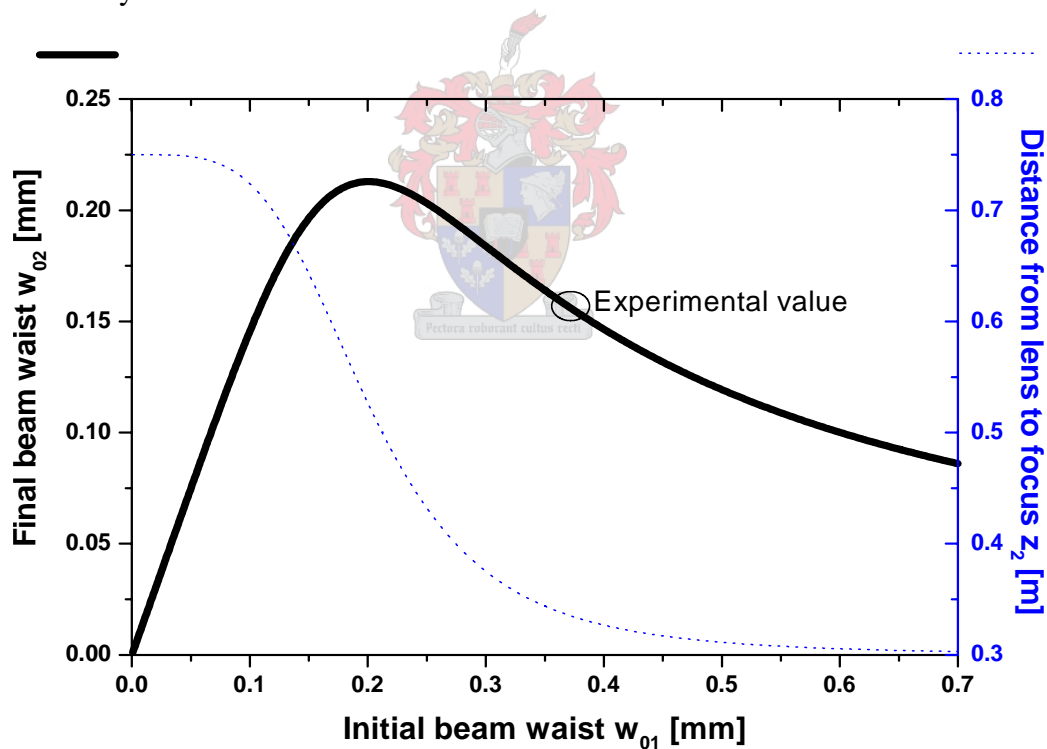


Figure 1.6: Calculations of the focussed waist size (left axis / solid line) and the distance of this focus from the lens (right axis / dashed line) as a function of initial beam waist size  $w_{01}$ . This investigation is for  $z_1 = 0.5$  m,  $f = 0.3$  m,  $\lambda = 632.8$  nm.

### 1.4.4 Lens focal length

Different lenses may be used, in order to change the focussed waist size of the given laser beams. This effect of different focal length lenses on the focussed waist size and distance is illustrated in Figure 1.7. This shows that a linear region exists, in which shorter focal lengths focus the beam to smaller beam waists. The *experimental value* of the typical focussing situation lies in this region. At much longer focal lengths, the focussed beam waist size reaches a peak at a certain value. This can be explained by the fact that such long focal lengths, in conjunction with the given divergence properties of the incident beam, are no longer able to focus the beam and at even longer focal lengths, the beam will diverge rather than converge. In the diverging section, the beam waist size  $w_{02}$  represents the corresponding virtual waist size. This virtual waist is located at a point to the left of the lens, which is denoted by a negative value of  $z_2$ .

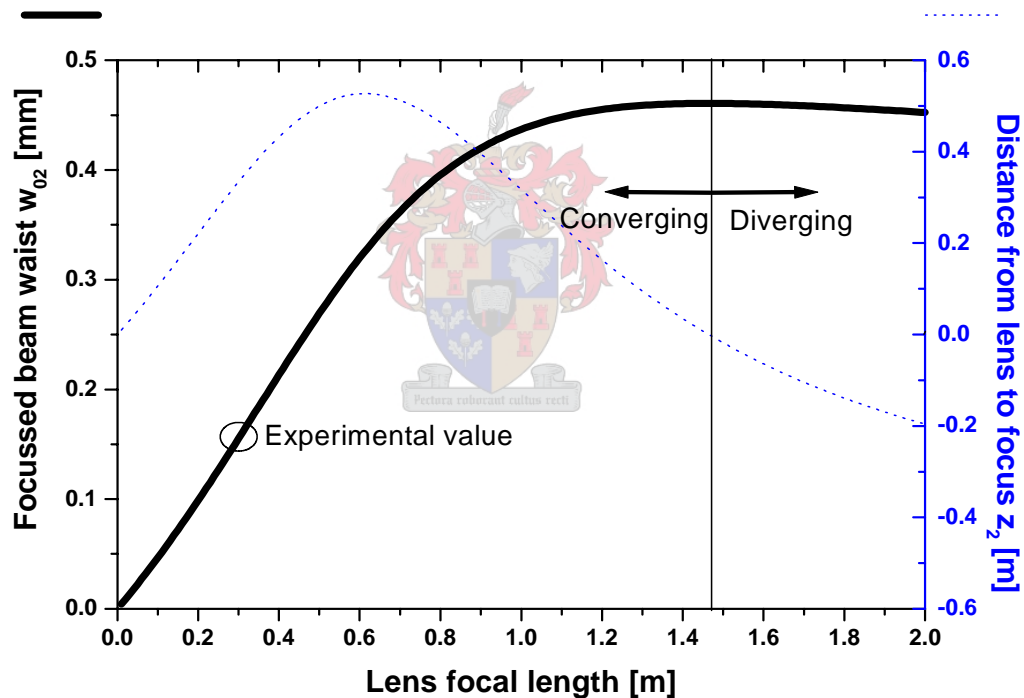


Figure 1.7: Calculations of the focussed waist size (left axis / solid line) and the distance of this focus from the lens (right axis / dashed line) as a function of lens focal length  $f$ . This investigation is for  $w_{01} = 0.3740$  mm,  $z_1 = 0.5$  m,  $\lambda = 632.8$  nm.

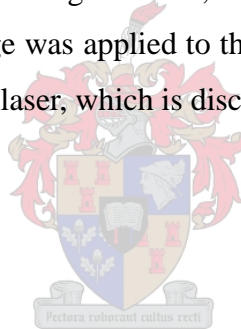
## 1.5 Conclusions

These parameter tests were done for a specific experimental setup of a Helium-Neon laser beam. The conclusion of these parameter tests with respect to the region of interest, a small deviation from the given typical focussing situation values, can be summarized as follows:

- A shorter wavelength results in a smaller focussed waist
- A larger distance from initial waist to lens results in a smaller focussed waist
- A larger initial beam waist results in a smaller focussed waist
- A shorter focal length lens results in a smaller focussed waist

These conclusions may now be used as general rules for application to experimental focussing conditions. The effects of changes of the initial distance  $z_1$  and the focal length lens  $f$  may be used to increase or decrease the focussed waist size, in a given experimental setup. The effects of changes of the wavelength  $\lambda$  and the initial waist size  $w_{01}$ , which result from the use of different laser beams in the same focussing situation, have been identified.

Experimentally, this knowledge was applied to the focussing of different laser beams into the hollow waveguide of the Raman laser, which is discussed in Section 3.5.



# Chapter 2

## Diffractive optical elements

### 2.1 Introduction

Diffractive Optical Elements (DOEs) are optical elements which consist of zones which diffract the incoming light, and the light from the different zones interferes to form the desired wavefront. This is in contrast to other elements such as lenses, which work on the principle of refraction. DOEs do have limited refractive properties, but the contribution due to the diffracted light is much larger. DOEs may transfer all the incident beam energy into the required wavefront.

DOEs are a relatively new generation of optical components. They can almost perfectly simulate any type of lens, mirror or diffraction grating. They can be transmissive or reflective, and have the advantage of higher damage thresholds and higher transmission efficiencies than regular components. These advantages make DOEs ideal for various laser applications. The basic technique of DOE manufacture is by an iterative series of mask projection and etching steps, which result in a binary surface profile. The manufacturing techniques have improved greatly in the last decade, due to improved laser photolithographic techniques [5]. The design of DOEs has also simplified and improved due to improvements of the design algorithms. High precision replication methods such as UV embossing and injection molding have led to the reduced cost of DOEs. The replicated DOEs typically cost only 10 - 20% as much as the original DOE [6]. The greatest advantage of DOEs is the fact that any structure shape may be manufactured, including complicated elements such as asymmetric aspherics. These advantages lead to the popular use of DOEs as beam shaping optics.

A specific DOE has been designed and manufactured by a partner in industry, for use as a beam shaping optic. The beam shaping design is to transform a Gaussian  $CO_2$  laser beam to a flat-top profile. In this work, a purely numerical investigation of the beam shaping characteristics of this DOE was done, based on scalar diffraction theory. An investigation of the effects of deviations from the design parameters serve to identify the critical parameters. This knowledge may be applied in experimental situations to facilitate more efficient use of the DOE.

## 2.2 Numerical model

The principle of diffractive optics is that any optical element can be simulated by simply modifying a beam's relative phase values, i.e. by introducing a phase element. The transmitted beam subsequently undergoes interference and generates the required profile. Such phase elements are relatively simple to model using numerical methods. A computer program was written which calculates scalar diffraction propagation, using the Rayleigh-Sommerfeld diffraction formula. This program was used to model the beam shaping effects of the DOE under consideration.

The Rayleigh-Sommerfeld diffraction formula can be used to calculate the field  $U_1$  due to the field  $U_0$ . Thus it can be used as a propagation formula, or propagator. In the simplest case, the initial and final fields are chosen parallel to each other and perpendicular to the propagation direction, the  $\hat{z}$ -axis. This is demonstrated in Figure 2.1.

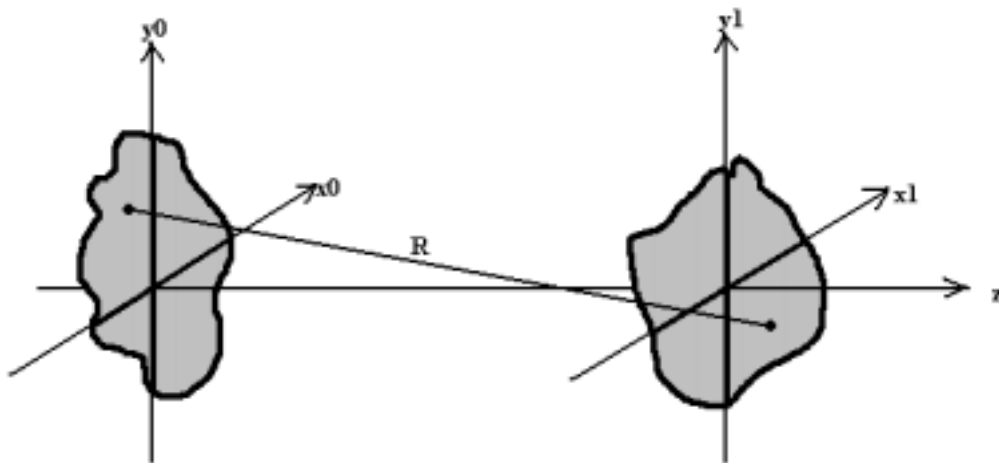


Figure 2.1: Propagation calculation with the Rayleigh-Sommerfeld diffraction formula. The contribution of a single point in the initial field  $U_0(x_0, y_0)$  to a single point in the final field  $U_1(x_1, y_1)$  is illustrated.

The quantities of interest are:

Initial field point:  $U_0(x_0, y_0, z_0)$

Final field point:  $U_1(x_1, y_1, z_1)$

$$R = \frac{U_1(x_1, y_1, z_1)}{(x_1 - x_0)^2 + (y_1 - y_0)^2 + (z_1 - z_0)^2}$$

The contribution of the initial field  $U_0(x_0, y_0, z_0)$  to the final field at a specific point  $U_1(x_1, y_1, z_1)$  is given by the Rayleigh-Sommerfeld diffraction formula [7],[8]:

$$U_1(x_1, y_1, z_1) = \frac{1}{i\lambda} \iint_{x_0 y_0} U_0(x_0, y_0, z_0) \frac{e^{ikR}}{R} \cos(n, R) dS$$

The field amplitude at a point in the final field is given by integration over all the initial field points. In this representation,  $n$  is the normal to the surface  $U_0$  at the point  $(x_0, y_0, z_0)$ .

Keep in mind that the two planes are chosen parallel to each other and perpendicular to the direction of propagation which is chosen as the  $\hat{z}$ -direction. Thus we can set

$$z_0 = 0$$

$$z_1 = z$$

This yields the simpler form of the Rayleigh-Sommerfeld diffraction formula:

$$U_1(x_1, y_1, z) = \frac{1}{i\lambda} \iint_{x_0 y_0} U_0(x_0, y_0, 0) \frac{e^{ikR}}{R} \cos(n, R) dS$$

The complex-valued fields are usually represented by a phasor:

$$U = |U| e^{i\phi}$$

This can also be represented as follows, refer to Figure 2.2:

$$U = a + ib \tag{2.1}$$

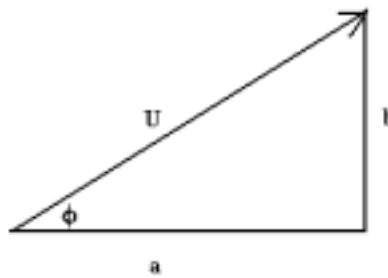


Figure 2.2: The phasor notation for complex fields

The intensity and phase is given by:

$$I = |U|^2 = a^2 + b^2 \tag{2.2}$$

$$\Phi = \arctan\left(\frac{b}{a}\right) \tag{2.3}$$

The coupling of the real and imaginary parts of the fields in the intensity and phase profiles is an important fact, which was used to validate the model as follows. Various well-known examples, such as Gaussian propagation in free space, were calculated by this program. The corresponding analytical solutions, which give the expected intensity profiles in each case, were compared to the results from the numerical program. If the calculated intensity profile was found to be correct, by comparison to the analytical solution, this implies the correctness of the phase profile, due to the above-mentioned coupling.

Now, using the convention of Equation 2.1 we can define the initial and final fields respectively as:

$$U_0 = a + ib$$

$$U_1 = c + id$$

The Rayleigh-Sommerfeld formula is given, as before:

$$U_1(x_1, y_1, z) = \frac{1}{i\lambda} \iint_{U_0} U_0(x_0, y_0, 0) \frac{e^{ikR}}{R} \cos(n, R) dS$$

Where the final field point is in the  $z_1 = z$  plane and  $z_0 = 0$ ,  $R$  is defined as:

$$\begin{aligned} R &= \sqrt{(x_1 - x_0)^2 + (y_1 - y_0)^2 + (z_1 - z_0)^2} \\ &= \sqrt{(x_1 - x_0)^2 + (y_1 - y_0)^2 + z^2} \end{aligned}$$

Due to the perpendicular fields, the cosine factor simplifies to:

$$\cos(n, R) = z/R$$

Changing the integral to a summation can be done by the following transformations:

$$\begin{aligned} \iint_{x_0, y_0} dS &= \begin{matrix} dx & dy \\ \times & \times \end{matrix} \rightarrow \Delta x \Delta y \\ &\rightarrow \begin{matrix} x_0 & y_0 \end{matrix} \end{aligned}$$

Now we can rewrite the Rayleigh-Sommerfeld diffraction formula in a form suitable for numerical calculation:

$$\begin{aligned}
 U_1 &= \frac{1}{i\lambda} \int_{x_0}^{x_0} \int_{y_0}^{y_0} U_0(x_0, y_0, 0) \frac{\cos kR + i \sin kR}{R} \frac{z}{R} \Delta x \Delta y \\
 &= \frac{z}{i\lambda} \int_{x_0}^{x_0} \int_{y_0}^{y_0} U_0 \times \frac{\cos(kR) + i \sin(kR)}{R^2} \Delta x \Delta y \\
 &= \frac{z}{i\lambda} \int_{x_0}^{x_0} \int_{y_0}^{y_0} (a + ib) \times \frac{\cos(kR) + i \sin(kR)}{R^2} \Delta x \Delta y
 \end{aligned}$$

We can find the value at the point  $U_1(x_1, y_1, z)$  by calculating the real and imaginary components of the summation separately. This is given by:

$$\begin{aligned}
 c &= \frac{z}{\lambda} \int_{x_0}^{x_0} \int_{y_0}^{y_0} \frac{a \sin kR + b \cos kR}{R^2} \Delta x \Delta y \\
 d &= \frac{z}{\lambda} \int_{x_0}^{x_0} \int_{y_0}^{y_0} \frac{b \sin kR - a \cos kR}{R^2} \Delta x \Delta y
 \end{aligned}$$

Thus,  $U_1 = c + id$  is calculated numerically and from this, the intensity and phase is calculated as described above. By doing this calculation for every point in the final field, the entire distribution can be found.

As mentioned above, various well-known propagation examples were calculated, of which the results could be directly compared to analytical models. In this way, the program code was validated. Due to the finite size of the arrays representing the fields, certain physical limitations of the model exist. These limitations were investigated and it was found that extremely short propagation distances and small array sizes lead to incorrect results. This was quantified for the examples investigated, and may be found in [9]. Another physical limitation is the calculation time, which increases almost exponentially with array size.

The numerical model was also compared to a commercial optical modelling package, and found to be superior in certain cases. For this reason, this numerical model was the preferred method for investigating the beam shaping propagation of the DOE.

A more detailed account of this work can be found in my seminar entitled *Optical modelling using diffraction theory* [9].

## 2.3 Modelling of a diffractive optical element

The effect of a phase element can be described by the phase change induced by the element. Consider a simple wedge-shaped window system, such as Figure 2.3.

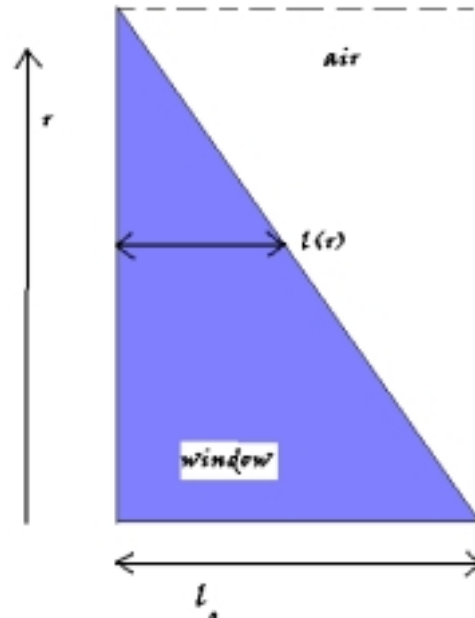


Figure 2.3: Simple wedge-shaped window system. The propagation direction is chosen left to right.

The window thickness as a function of radial distance is given by  $l(r)$ , the total propagation distance through the system is  $l_0$ . We know that  $l(r) \leq l_0$ . The window's index of refraction is  $n$  and the index of refraction of air is 1. This gives the phase change as:

$$\begin{aligned}
 \Delta\phi &= k n_{\text{window}} l_{\text{window}} + k n_{\text{air}} l_{\text{air}} \\
 &= k n l(r) + k (l_0 - l(r)) \\
 &= k (n - 1) l(r) + k l_0
 \end{aligned} \tag{2.4}$$

Since the second term in Equation 2.4 is simply a constant phase addition, independent of radial position, it can be neglected here. We are only interested in the relative phase difference between different points in the beam cross-section, not total phase difference relative to the initial phase. This gives for the relative phase change:

$$\Delta\phi(r) = k (n - 1) l(r) \tag{2.5}$$

where

$$k = \frac{2\pi}{\lambda} \quad (2.6)$$

Equations 2.5 and 2.6 give a transform between the phase change induced by an element and the physical profile height which corresponds to such a change. This makes it possible to design physical optics, if the required phase change is known. Also note that *any phase value* can be described by the modulated phase value in the interval  $[0, 2\pi]$ . Thus, any physical optic can be reduced to a modulated element with maximum height:

$$l(r)_{\max} = \frac{\Delta\phi(r)_{\max}}{k(n-1)} = \frac{2\pi\lambda}{2\pi(n-1)} = \frac{\lambda}{n-1}$$

Thus, a phase value in  $[0, 2\pi]$  corresponds to a distance (or element thickness) in  $[0, \frac{\lambda}{n-1}]$ .

This principle can be explained by a simple lens example. The phase difference induced by a thin spherical lens of focal length  $f$  is given by:

$$\Delta\phi = \frac{-kr^2}{2f} \quad (2.7)$$

The cross-sectional profile of such a spherical lens is shown schematically in Figure 2.4.



Figure 2.4: Schematic illustration of the cross-section of a spherical lens.

By modulating the phase induced by this lens to values in  $[0, 2\pi]$ , a typical DOE profile is generated, with maximum profile height given by  $l(r)_{\max} = \frac{\lambda}{n-1}$ . The resulting profile is shown in Figure 2.5.

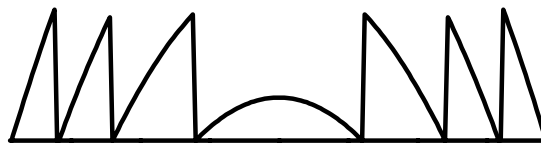


Figure 2.5: Schematic illustration of the cross-section of a diffractive optical element.

This example illustrates the application of a lens as a DOE, but the advantage of DOEs is that any required transverse profile may be created in the same way.

DOEs are generally produced by lithography - by ablating layers of material, using masks, until the desired profile remains. This will of course be a *binary element* with a step-like appearance, since the number of ablated levels is finite. A typical DOE cross-section is given in Figure 2.6. It can be shown that a DOE with as few as 16 levels of ablation can achieve nearly 100%

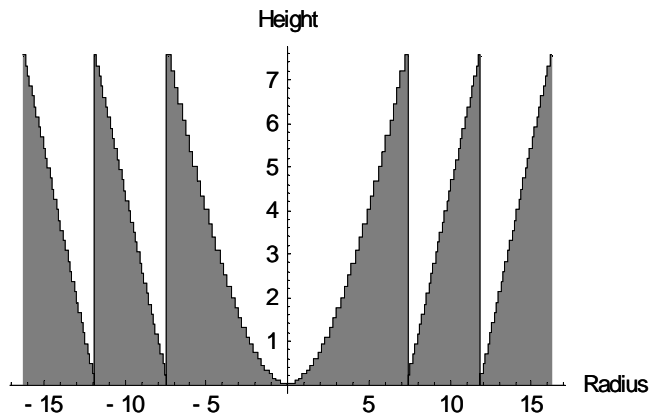


Figure 2.6: A typical binary DOE profile: the height is given in  $\mu\text{m}$  and the radius in mm.

efficiency. This efficiency refers to the fraction of incident light which is transformed, without scattering losses, into the first diffraction order, the desired beam profile. This is demonstrated in Figure 2.7 [5].

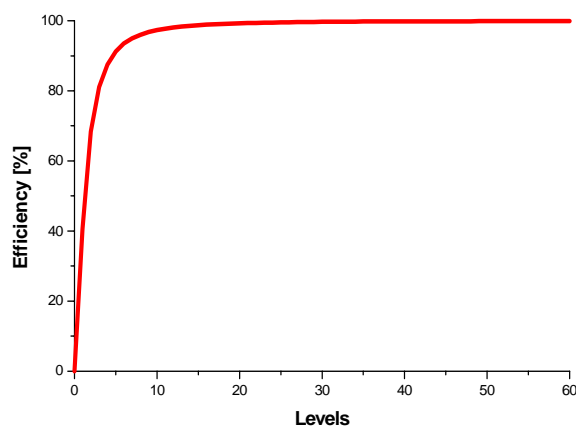


Figure 2.7: Transmission efficiency of a typical DOE as a function of the number of ablated levels.

## 2.4 Beam shaping design

The DOE under investigation here was designed to generate a super-Gaussian or *flat-top* beam profile. This beam profile has advantages in many applications which have a threshold intensity value. In this case, the design is for  $CO_2$  laser beam shaping, for more efficient target-gas irradiation, and is to be used in a selective photochemistry process. The design parameters, referred to as the *ideal case*, were:

- Pure Gaussian ( $TEM_{00}$ ) input beam
- Input beam waist size  $w_0 = 7$  mm
- Input beam positioned radially in the centre of the DOE. ( $\Delta r = 0$ )
- The DOE positioned axially at the waist of the beam. ( $z = 0$ )
- Wavelength:  $\lambda = 10.6$   $\mu\text{m}$
- DOE placed on focussing lens of focal length:  $f = 2.1$  m
- Final beam shape created at focal distance of lens:  $z = 2.1$  m

The desired flat-top profile should theoretically have a beam radius  $w \approx 5$  mm and a flat-top intensity approximately 22% higher than the initial Gaussian peak intensity. This is demonstrated in Figure 2.8.

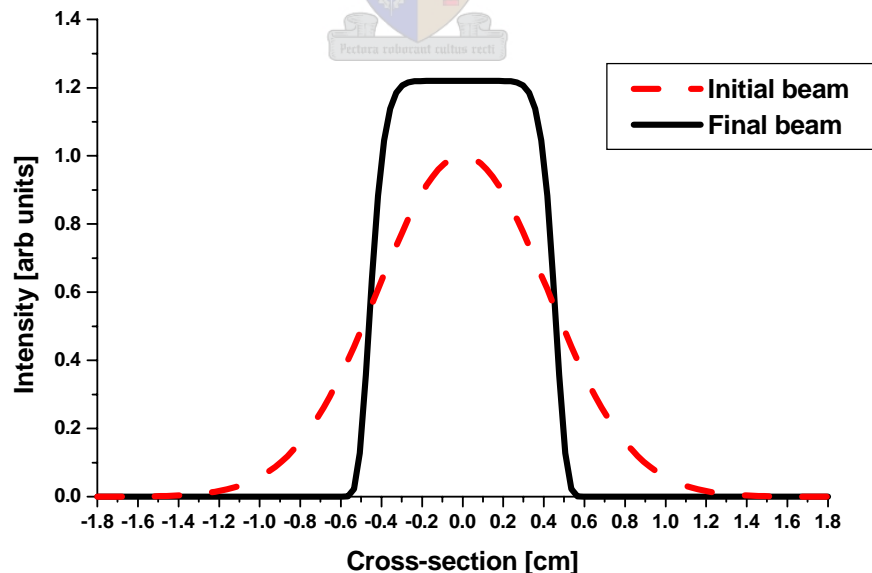


Figure 2.8: The DOE design: initial Gaussian intensity profile and desired super-Gaussian intensity profile.

The numerical calculations were all done by modelling the DOE as a phase element, using phase data obtained from Scientific Development and Integration (SDI). The calculation of the beam profile in the ideal case showed a deviation from the desired flat-top profile, due to the imperfect DOE design methods. These design methods are based on simplifications to the scalar diffraction theory, such as Fourier transform methods. Figure 2.9 shows the calculated intensity profile at the focal distance, in comparison to the design profile of a pure super-Gaussian of the 5th order<sup>5</sup>.

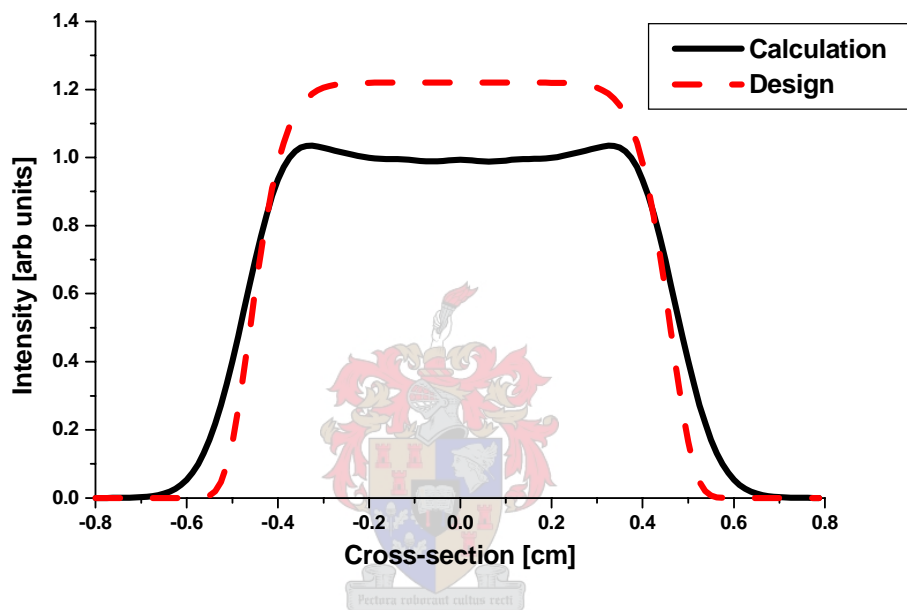


Figure 2.9: Comparison between the design profile and the numerically calculated profile.

<sup>5</sup> This definition may be found in Appendix A.

Calculation of the beam profile in the ideal case was done for various propagation distances, and the resulting beam shaping propagation is demonstrated in Figure 2.10. It can be seen that the flat-top profile is disrupted soon after the focal distance around 2 m. Depending on the application, this may be undesirable and a second element may be introduced which again modifies the phase such that the flat-top beam profile may be maintained over a longer propagation distance.

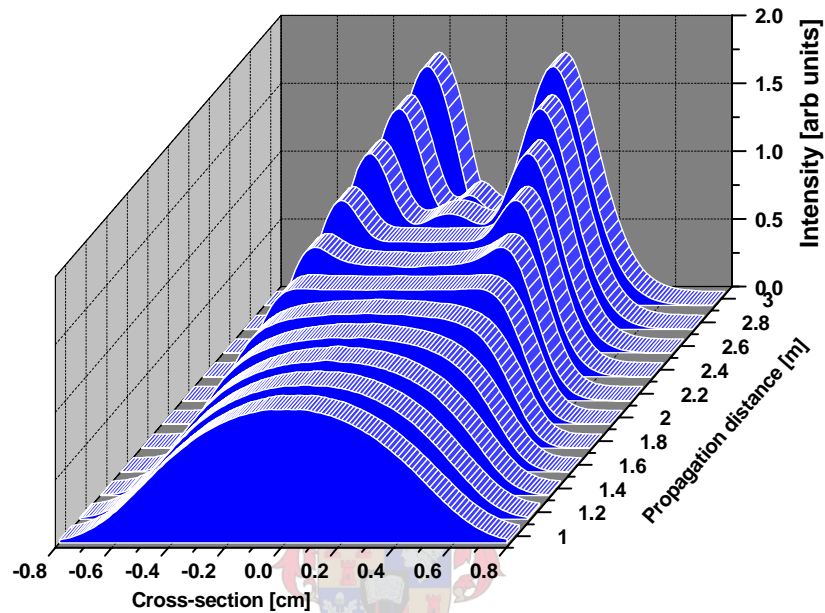


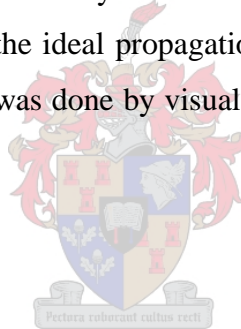
Figure 2.10: Propagation of the beam between 1 and 3 m after the DOE, demonstrating the ideal beam shaping situation with the flat-top profile near 2 m.

## 2.5 Parameter sensitivity testing

Numerical modelling of the beam shaping capability of the DOE was done for various deviations from the design parameters. This identifies the parameters which are critical in an experimental situation, such that efficient use of the DOE may be facilitated. The parameter deviations investigated were:

- Wavelength  $\lambda$
- Non-ideal Gaussian initial beam
- Initial beam size change, independent of beam phase  $w_0$
- Initial beam phase change, independent of beam size  $\Delta\phi$
- Initial Gaussian beam offset axially in the propagation direction  $\Delta z$
- Initial beam offset from centre of DOE radially  $\Delta r$
- Effect of different focal length lenses  $f$  on final beam character

Propagation comparisons were made by calculating the intensity profile at various distances and comparing this propagation to the ideal propagation given in Figure 2.10. Comparison of intensity profiles in the focal plane was done by visual inspection of the various profiles on the same intensity scale.



### 2.5.1 Wavelength

The effect of wavelength on the beam shaping was investigated and was found to have a negligible effect in the region of  $CO_2$  laser wavelengths. The change in the phase profile induced by the DOE due to a different wavelength was taken into account. The reason for this is the wavelength dependence of the transformation between DOE profile height ( $h$ ) and phase profile ( $\Delta\phi$ ), from Equations 2.5 and 2.6:

$$\Delta\phi = \frac{2\pi}{\lambda}(n - 1)h$$

What is neglected here, is the fact that the index of refraction of the material changes slightly for different wavelengths. It is thus assumed that the index of refraction is constant in the wavelength region of interest, which is a good approximation. The results of this investigation are given by plotting the final beam shape at the focal distance, as shown in Figure 2.11. This shows identical beam profiles for the wavelengths tested:  $\lambda = 9.2824, 9.5524$  and  $10.6000 \mu\text{m}$ . This choice of wavelengths is a good representation of the available  $CO_2$  laser wavelengths, which range from  $9.1265$  to  $11.0165 \mu\text{m}$ .

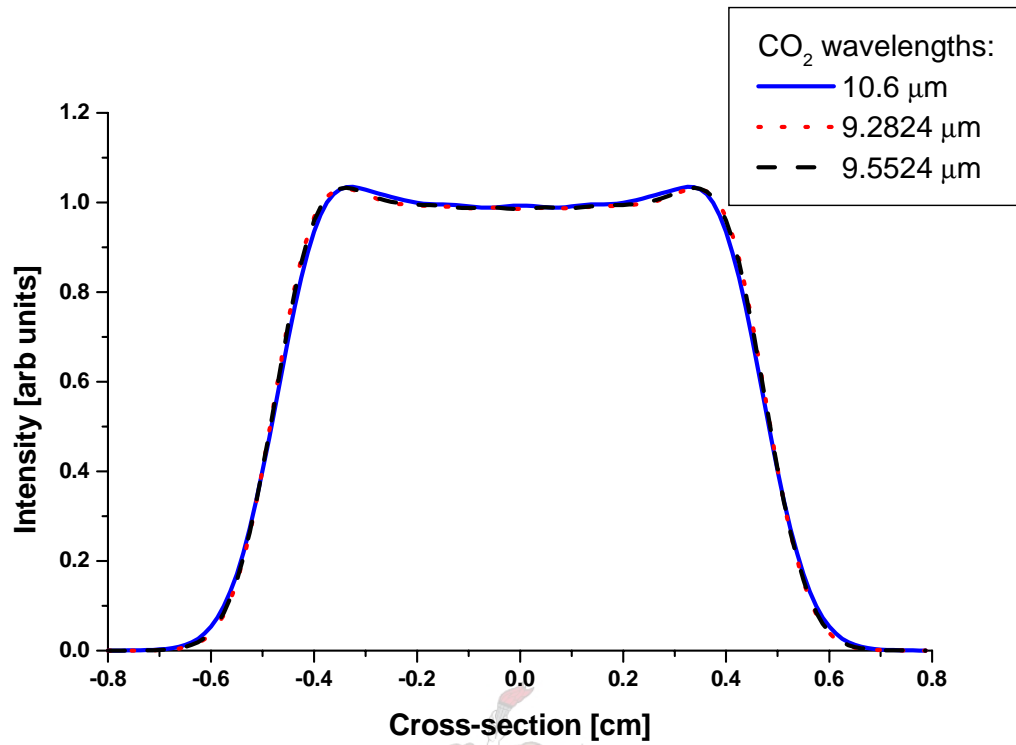


Figure 2.11: The flat-top intensity profile of different laser wavelengths at the focal distance.

In conclusion, the propagation and beam shaping capability of the DOE is insensitive to different CO<sub>2</sub> laser wavelengths. The advantage of this is that any CO<sub>2</sub> laser wavelength may be shaped efficiently by the given DOE.

## 2.5.2 Non-Gaussian initial beam

As has been mentioned, the design assumes an ideal Gaussian beam. In practice, laser beams are never ideally Gaussian. In order to model this, the resonator modes  $TEM_{00}$  and  $TEM_{10}$  were mixed and the simulation was done with this *mixed* beam. In this work, the  $TEM_{10}$  mode refers to the cylindrically symmetrical case where  $TEM_{10}$  and  $TEM_{01}$  are degenerate: the so-called *doughnut* mode<sup>6</sup>.

The mixed beam is described by a *mixing factor*, such that a high mixing factor corresponds to a nearly Gaussian beam. The definition of the mixing factor is as follows: a mixing factor of  $n$  translates to  $n$  parts  $TEM_{00}$  and 1 part  $TEM_{10}$ . The beam profiles of the initial mixed beams of mixing factors 0, 1, 2 and 10 are shown in Figure 2.12.

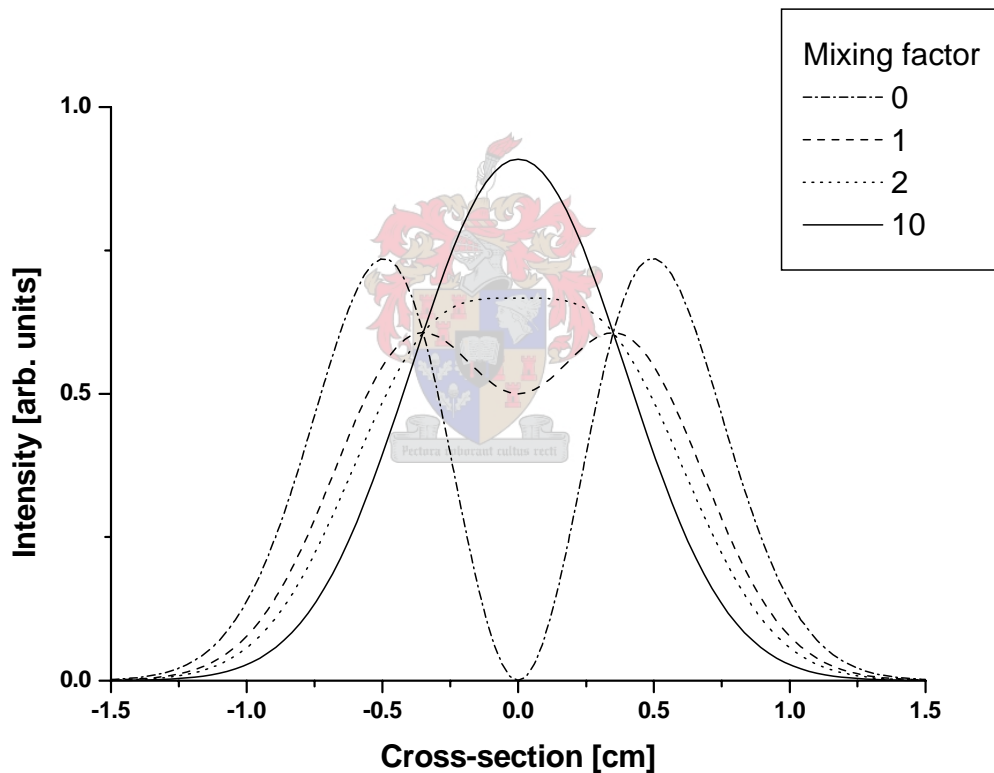


Figure 2.12: Intensity profiles of the incident beam for different mixing factors.

<sup>6</sup> In order to normalize this the intensity profile was multiplied by factor 0.5. Energy conservation was observed.

The propagation was done to the focal distance for each of these mixed beams, and the resulting profiles are shown in Figure 2.13. For mixed beams which differ greatly from the Gaussian profile, the beam shaping is inefficient. However, the mixing factor of 10 corresponds closely to the desired beam profile at the focal distance.

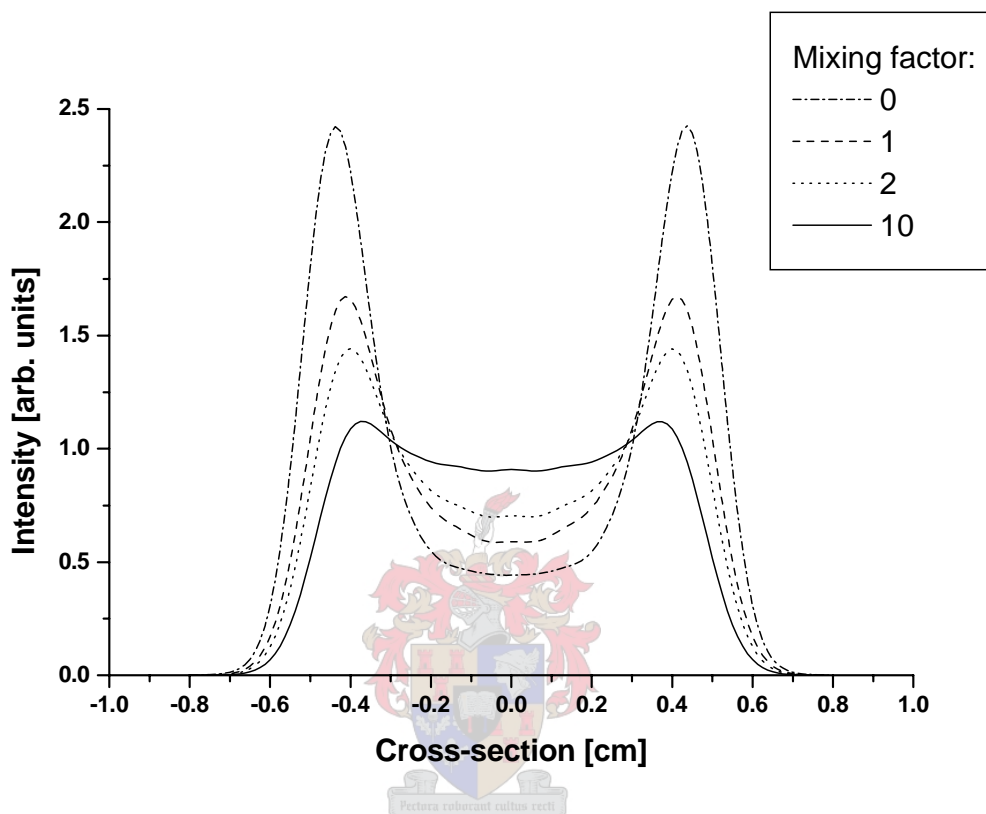


Figure 2.13: Intensity profiles of the final beam at the focal distance for different mixing factors.

The beam shaping propagation of the mixed beam of mixing factor 10 is shown in Figure 2.14. This mixed beam has a theoretical beam quality of  $M^2 = 1.2$ . This was calculated at the initial beam waist position, according to the transformation

$$W = Mw$$

where  $W$  is the beam size of the mixed beam profile, according to a Gaussian fit, and  $w$  is the beam waist size of the corresponding (unmixed) Gaussian profile. The beam quality factor is introduced in Appendix A. This leads to:

$$M^2 = \frac{W^2}{w^2}$$

This is a good numerical approximation of real  $CO_2$  laser beams, since commercial  $CO_2$  lasers have typical beam quality factors in the range  $M^2 = 1.1 \rightarrow M^2 = 1.4$ .

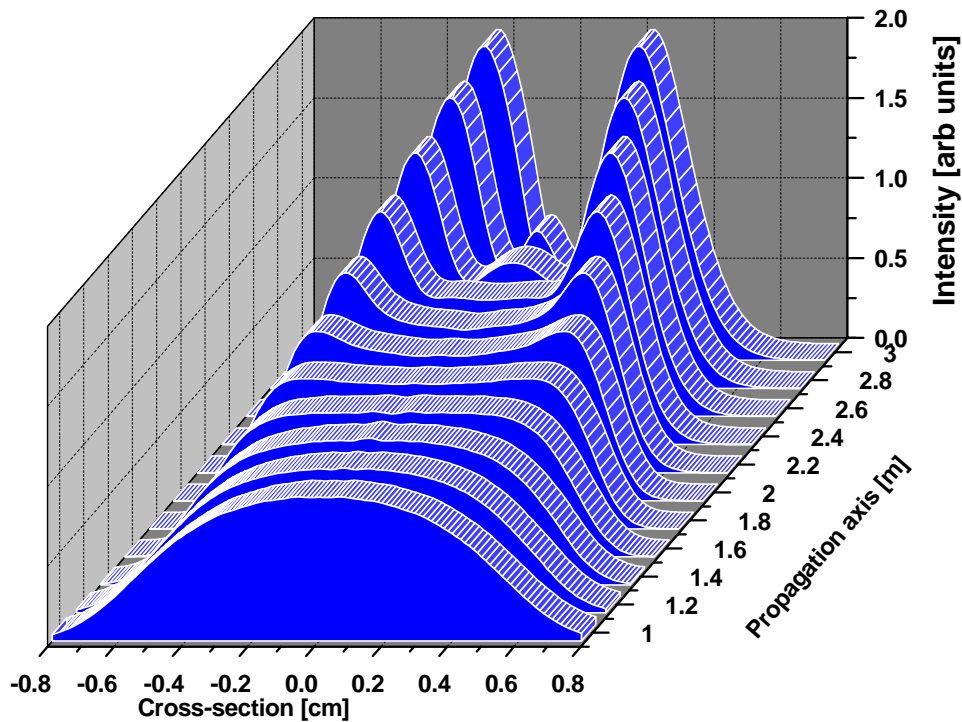


Figure 2.14: The beam shaping propagation of a mixed beam of mixing factor 10.

This figure should be compared to the ideal propagation shown in Figure 2.10. From this comparison, it can be concluded that the propagation of the non-ideal beam is similar to the ideal case, generating a flat-top profile at a distance slightly closer than expected. This flat-top profile is also wider and lower than in the ideal case.

### 2.5.3 Initial beam size

The reason for the interest in the effect of a variation of the beam size, is due to the fact that this parameter may change easily during operation of the laser. Besides the deviation of the inherent laser beam size, an optical system would likely be used to produce the  $w_0 = 7$  mm beam for application to the DOE. This system is liable to variations and a qualitative description of the effect of this on the beam shaping is desirable.

In this section, it must be noted that as the beam width changes, the peak intensity remains 1 and the phase remains flat (zero phase). This is not in accordance with Gaussian propagation of a  $w_0 = 7$  mm beam and thus energy conservation, but the result here is qualitative. It is meant only to show how the propagation will change for a different size beam, and thus demonstrate the sensitivity of the beam shaping process to beam size changes.

The propagation of a smaller initial beam size ( $w_0 = 6$  mm) is given in Figure 2.15. The propagation of a larger initial beam size ( $w_0 = 8$  mm) is given in Figure 2.16. If these figures are compared to the ideal beam shaping shown in Figure 2.10, the qualitative effect can be deduced. A smaller beam generates the flat-top at a larger distance from the DOE. Similarly, a larger initial beam generates the flat-top at a closer distance than expected.

These deviations are extreme ( $w_0 = 7 \pm 1$  mm), and smaller deviations of the initial beam size (which is more likely) result in beam shaping characteristics which are closer to the desired ideal case. It may be concluded that the beam size has an influence on the position of the desired flat-top beam profile. This effect may be attributed to the focussing characteristics and should be investigated.

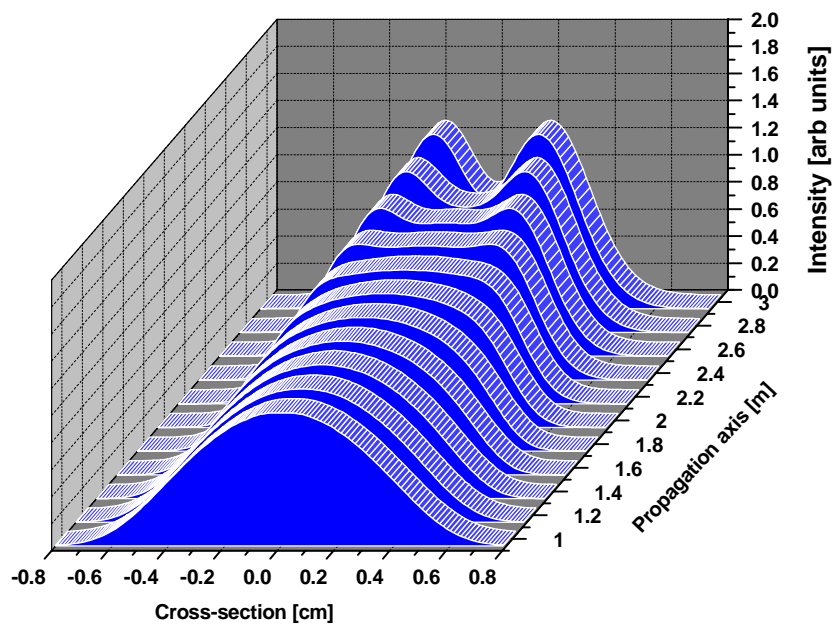


Figure 2.15: The beam shaping propagation of an initial beam size of 6 mm.

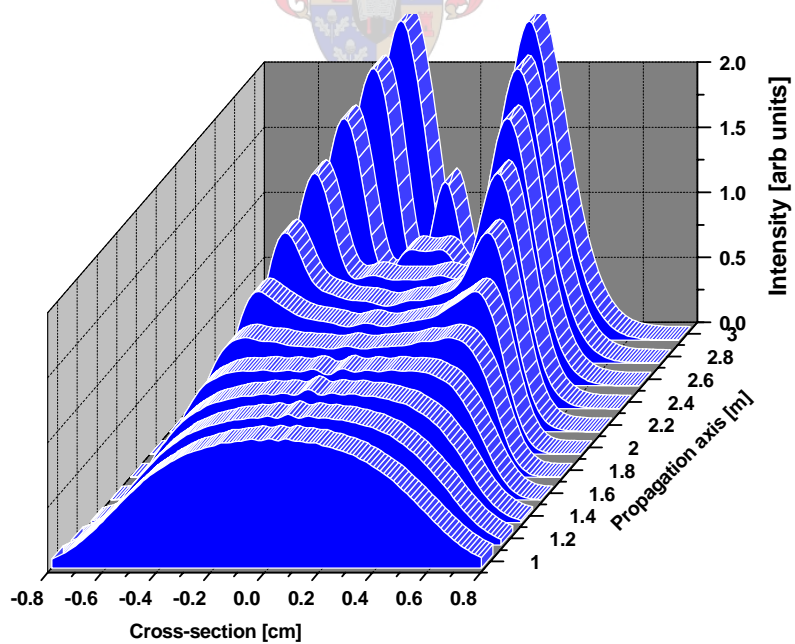


Figure 2.16: The beam shaping propagation of an initial beam size of 8 mm.

### 2.5.4 Initial beam phase

This investigation refers to changing the phase of the beam such that it corresponds to a Gaussian which is not at its beam waist (as is the design parameters). This illustrates the sensitivity of the DOE position relative to the beam waist position, independent of beam size. The beam size is in all cases taken as exactly  $w_0 = 7$  mm. The term *phase mismatch*, which I define here and denote as  $\Delta\phi$ , refers to the position in the beam path of an ideal Gaussian beam, such that the phase of the tested beam is given by Gaussian paraxial propagation theory, for a Gaussian beam which is at this position. A schematic illustration of this is given in Figure 2.17: a negative phase mismatch  $\Delta\phi < 0$  refers to a beam before the waist position and a positive phase mismatch  $\Delta\phi > 0$  refers to a beam after the waist position. The method of calculation of these phase profiles is given in Appendix C.

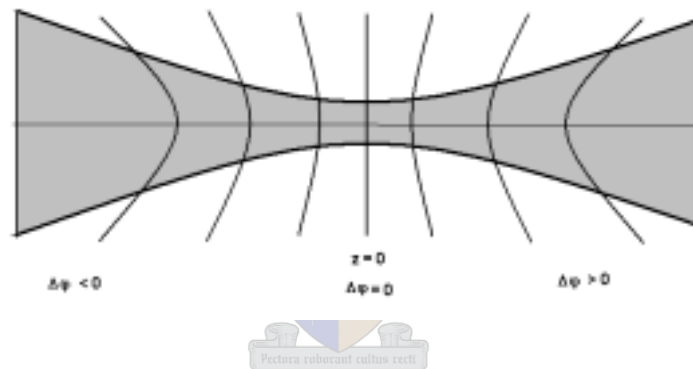


Figure 2.17: Schematic illustration of the phase profiles of a Gaussian beam at different positions around the waist position.

The resulting dependence of the final beam shape on the initial beam phase mismatch ( $\Delta\phi$ ) is given in Figure 2.18. It can be seen in the figure that a positive phase mismatch results in a flat-top beam profile which is lower and slightly wider. If the mismatch is negative, the final beam profile develops peaks and becomes narrower. It must be mentioned that this investigation was done with phase mismatches up to 10 m. Such phase mismatches are much larger than practically possible in most experimental situations, which are limited by the size of the laboratory. This leads to the conclusion that within regular situations ( $\Delta\phi < 2$  m), a phase mismatch is tolerable and the effect on the final beam profile is negligible.

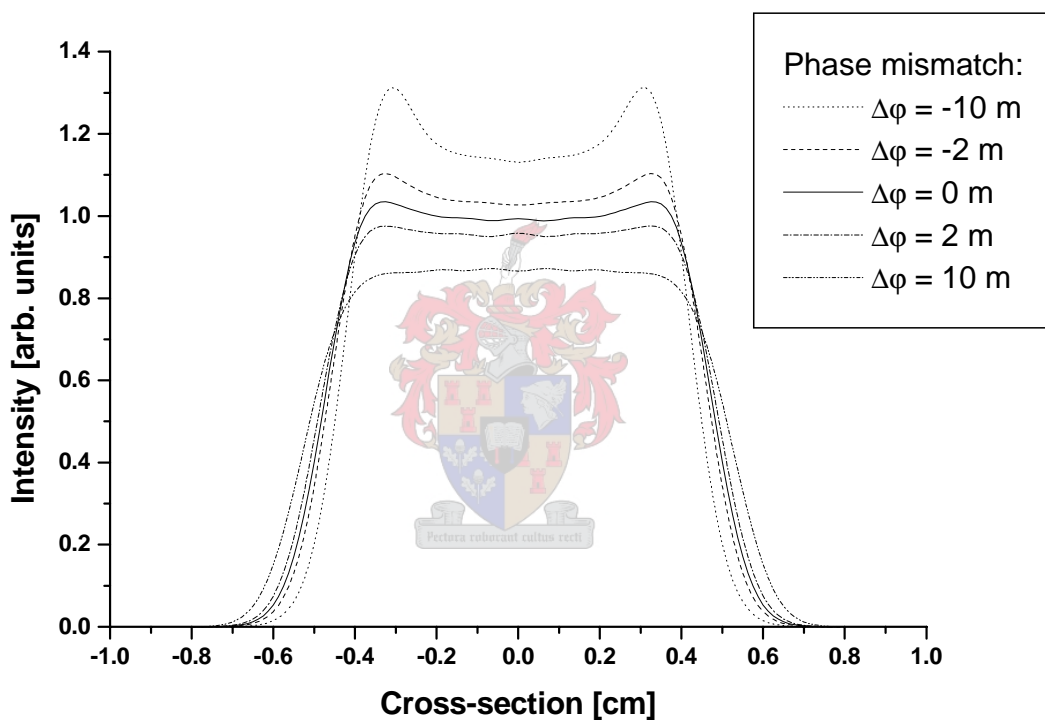


Figure 2.18: Intensity profiles of the final beam at the focal distance for different phase mismatch values.

### 2.5.5 Initial Gaussian beam offset axially

The effect of an axial offset  $\Delta z$  (in the direction of propagation) of the Gaussian beam with respect to the DOE determines the sensitivity of the axial positioning of the DOE with respect to the beam waist position. In this case the initial Gaussian beam has a waist size  $w_0 = 7$  mm, but this beam is offset axially with respect to the DOE. Thus, for an axial offset  $\Delta z$ , the beam size and phase profile changes according to Gaussian propagation theory. The calculations for the beam size and phase at the DOE are from the Gaussian Beam Solution to the Paraxial Wave Equation [2], as is described in Appendix A. A negative offset ( $\Delta z < 0$ ) refers to a beam which is converging and has not yet reached its beam waist before striking the DOE. A positive offset ( $\Delta z > 0$ ) refers to the case of a Gaussian beam diverging from its waist position when striking the DOE.

Figure 2.19 shows the final beam profile as a function of initial Gaussian beam axial offset  $\Delta z$ .

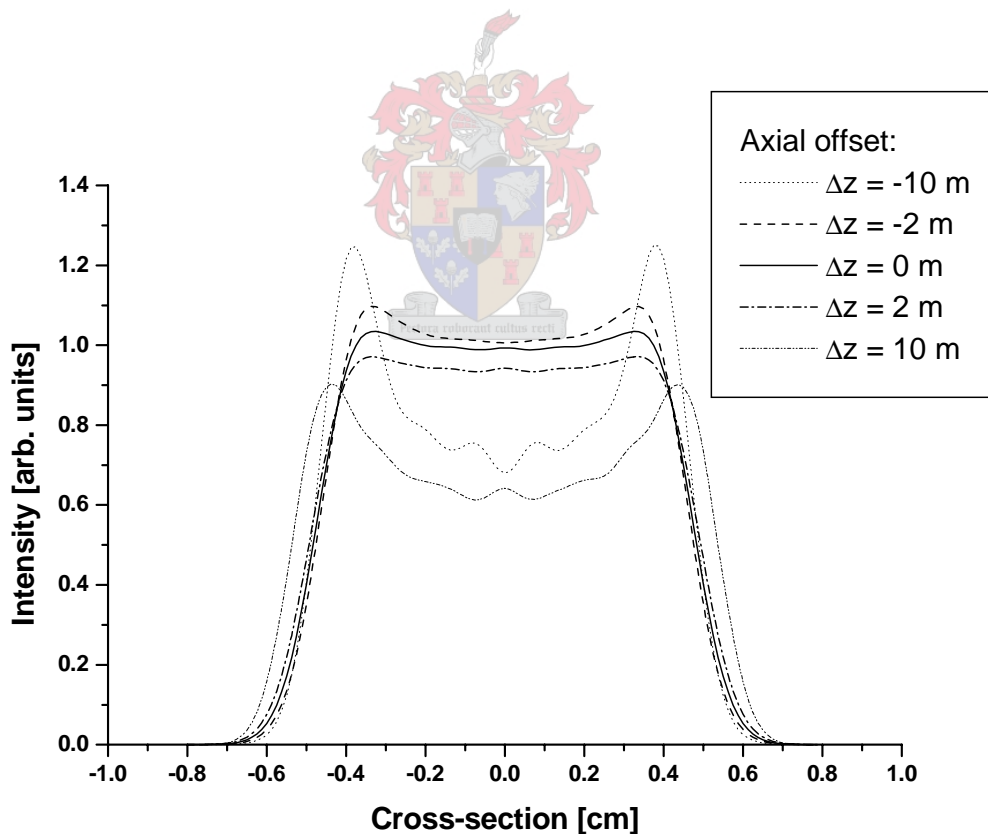


Figure 2.19: Intensity profiles of the final beam at the focal distance for different axial offset values.

As can be seen in Figure 2.19, only extremely large offset values change the desired profile appreciably. Over offset distances such as 2 m, which are extreme in most practical situations, the difference in profile is negligible. The effect of an axial offset of  $\Delta z = +1$  m on the beam shaping propagation is demonstrated in Figure 2.20.

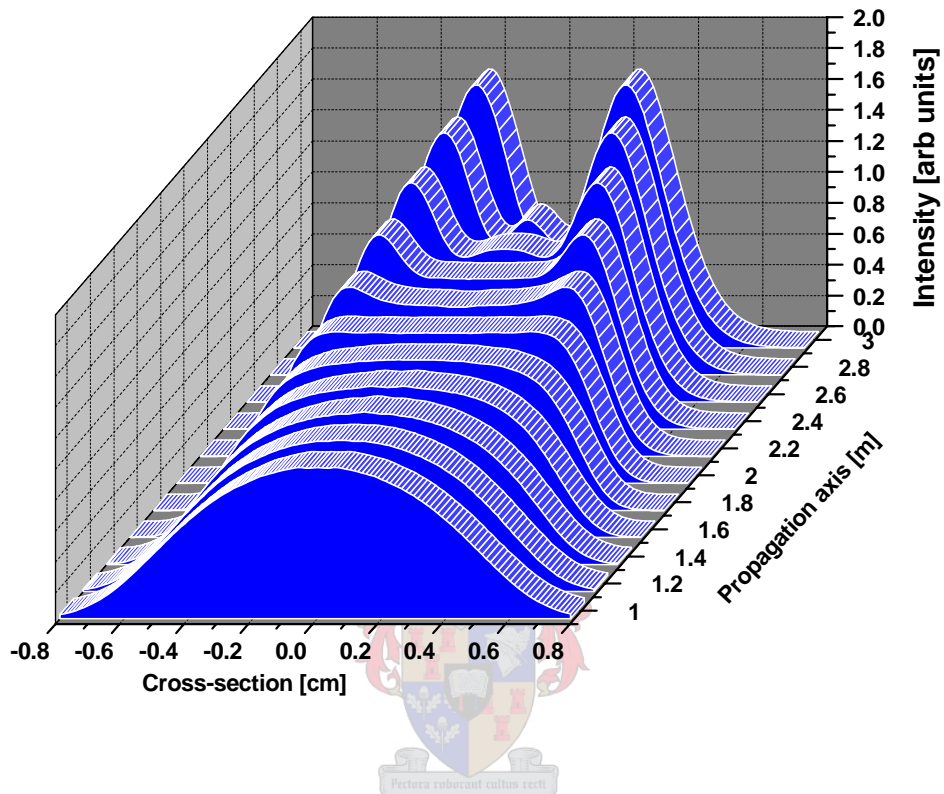


Figure 2.20: The beam shaping propagation due to an axial offset of +1 m: beam waist position 1 m before the DOE.

By comparison to Figure 2.10, this shows that an axial offset has a negligible effect on the beam shaping characteristics, in practical situations.

### 2.5.6 Radial offset

The effect of a radial offset of the initial beam on the DOE was investigated, because precise central positioning may be difficult to achieve in a practical situation. The final beam shape, at the focal distance, is investigated as a function of initial beam offset. Figures 2.21 and 2.22 show the three-dimensional intensity profile of the ideal case and an offset case, respectively. The offset in this case was in the  $x$ -axis, an offset amount of

$$\Delta x = 0.2w_0 = 0.2(7 \text{ mm}) = 1.4 \text{ mm}$$

This offset amount of  $\Delta x = 1.4 \text{ mm}$  should be seen in context of the beam waist size of 7 mm and the DOE radius of 15 mm. Note that the circular symmetry simplifies investigations: an offset in any radial direction results in a peak deviation in that direction.

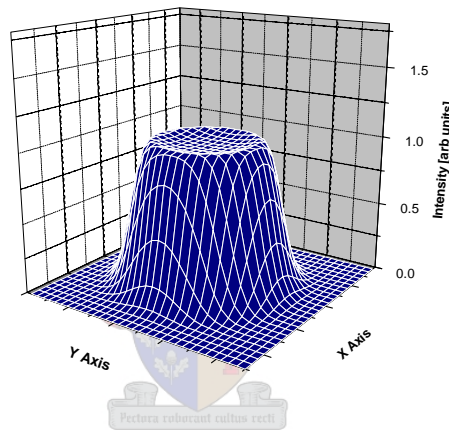


Figure 2.21: Three-dimensional representation of the desired intensity profile in the ideal case.

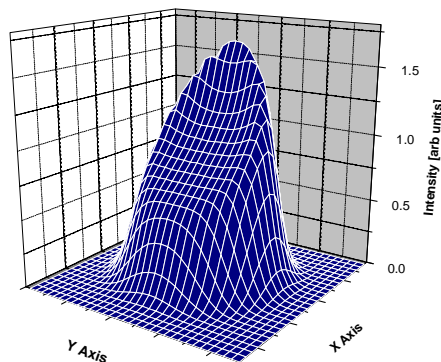


Figure 2.22: Three-dimensional representation of the intensity profile due to a radial offset of the initial beam:  $\Delta x = 1.4 \text{ mm}$ .

The propagation of a beam which is offset in the  $x$ -direction by an amount of  $\Delta x = 0.05w_0 = 350\mu\text{m}$  is shown in Figure 2.23. The propagation is similar to the ideal case, except for the slope induced by the radial offset. This slope was found to increase as a function of offset amount. The cross-sectional direction is also the  $x$ -axis.

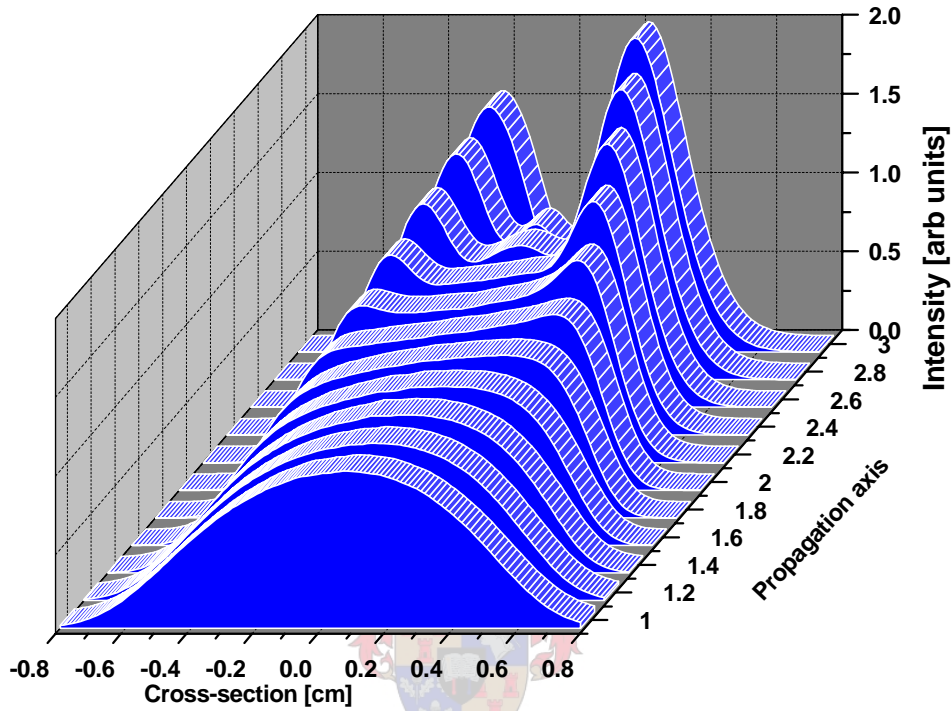


Figure 2.23: The beam shaping propagation of a radially offset beam, offset in the  $x$ -direction:  $\Delta x = 0.35$  mm.

The slope induced on the final beam profile results in a beam peak in the direction of the offset. This peak intensity, in comparison to the ideal flat-top intensity, was used to quantify the beam shape disruption as a function of offset amount: this called the *peak deviation*. The peak deviation is given by the difference between the disrupted beam peak intensity and the ideal flat-top beam peak intensity. Various simulations were done for different offsets and the results are presented graphically in Figure 2.24. The dependence of peak deviation as a function of offset amount was found to be almost linear in the region investigated.

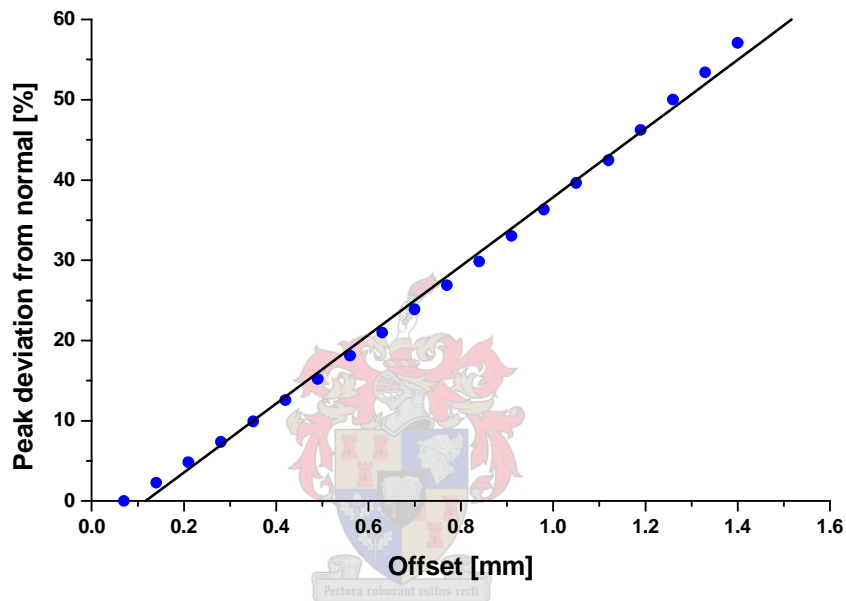


Figure 2.24: The peak deviation of the final intensity profile at the focal distance, as a function of radial offset amount.

It can be concluded that extremely small radial offset amounts (of the order of a few hundred  $\mu\text{m}$ ) easily disrupt the beam shaping capability of the DOE. The results presented in this section may be used to define the maximum offset amount tolerable in a given application. Furthermore, it has been shown that radial positioning of the DOE with respect to the beam path is extremely critical and specialized optical alignment techniques may be required.

### 2.5.7 Focal length of lens

The DOE was designed to be placed on top of a focussing lens. The design is such that for different focal length lenses, different flat-top peak intensities and widths are generated. The resulting profiles in the focal plane, after using different lenses, is demonstrated qualitatively in Figure 2.25. The effect is such that a short focal length lens will, over a short distance<sup>7</sup>, generate a very high peak intensity flat-top profile, with a narrow beam width. Similarly, a longer focal length lens generates a wider and lower top-hat profile at a larger distance from the DOE.

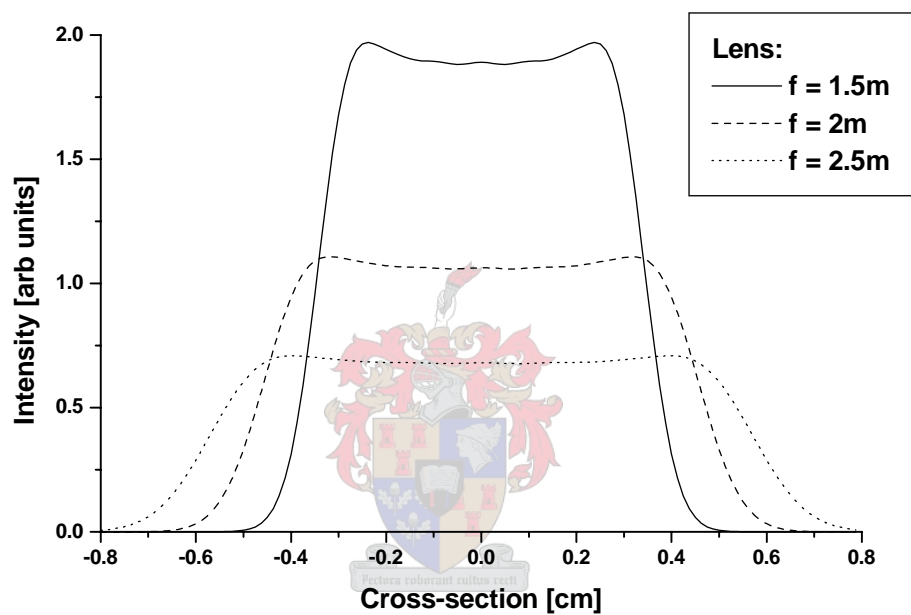


Figure 2.25: Illustration of the effect of the final intensity profile due to different lenses used in conjunction with the DOE: the different profiles are at the focal distance of each lens.

<sup>7</sup> This distance corresponds to the focal length of the lens used.

The data from various simulations has been processed and the results are presented in Figure 2.26. These results quantify the final beam shape at the focal distance (flat-top peak intensity and beam radius) as a function of lens focal length. This can be used in practice to decide on the most suitable lens for a given application, if the appropriate beam size and flat-top peak intensity can be estimated.

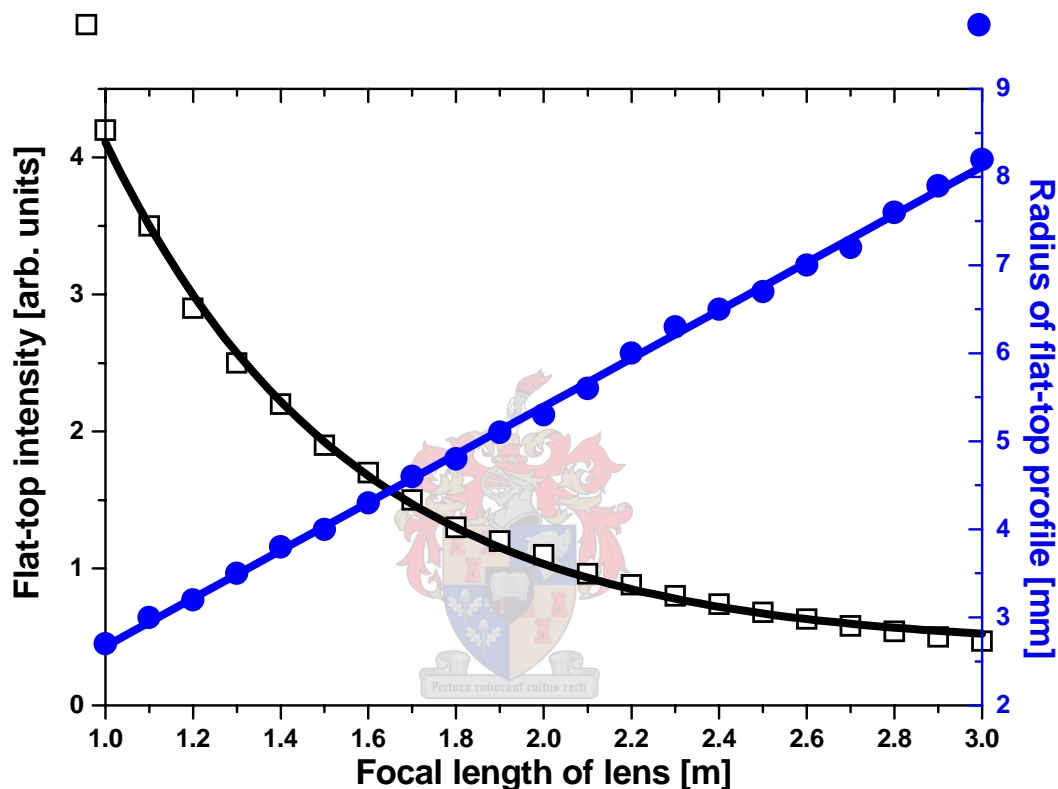


Figure 2.26: Quantification of the final intensity profile (flat-top intensity peak - hollow square points; beam radius - solid circular points) due to different lenses used in conjunction with the DOE: the different profiles are at the focal distance of each lens.

## 2.6 Conclusions

Various parameters which may influence the beam shaping characteristics of a given DOE were investigated numerically. The conclusions of these numerical parameter investigations can be summarized as follows. The wavelength has been found to have an effect on the beam shaping, but in the regime of  $CO_2$  laser wavelengths, this effect is negligible. Thus, any of the  $CO_2$  wavelengths may be efficiently shaped using this DOE. A good Gaussian character of the beam (good beam quality or  $M^2 \approx 1$ ) is important for efficient beam shaping, but not critical. Most commercial  $CO_2$  lasers have a beam quality factor  $M^2 < 1.2$ , which was shown to generate a flat-top profile and does not greatly alter the propagation characteristics. A change of the initial beam size has an effect on the beam shaping, generating the flat-top profile at a shorter distance for a larger initial beam. The propagation remains similar to the ideal case and the beam shaping remains useful. An initial beam phase change has minimal effect on the beam shaping, for typical experimental offset amounts. The axial positioning of the DOE with respect to the beam waist position was found to have a negligible effect on the beam shaping, for typical experimental situations. The radial alignment of the DOE with the beam path was identified as an extremely critical parameter. A radial misalignment causes a sloping profile and the beam disruption as a function of offset amount has been quantified. This result will determine the experimental design required for accurate alignment, as well as the allowed experimental error margin. Different lenses may be used in conjunction with the DOE and the effect on the generated beam profile has been quantified for the useful focal length region.

# Chapter 3

## Waveguides

### 3.1 Introduction

A simple and efficient beam shaping technique is the use of a waveguide. This involves the injection (by focussing) of a laser beam into a waveguide, in which the beam propagates by reflections from the walls, and is emitted at the other end. This results in a high intensity region inside the waveguide and, if propagation losses inside the waveguide are low, the high intensity region is maintained over a relatively long interaction region: the entire length of the guide. Many waveguide configurations exist, some examples are solid fibres (fibre optics), hollow fibres, hollow metal and dielectric waveguides, and photonic crystal fibres. The waveguides of interest in this thesis are the hollow, circular dielectric waveguides (capillaries). The reason for the interest in hollow waveguides, in contrast to solid waveguides, is because a gaseous medium may be placed inside the waveguide, resulting in a simple method of generating nonlinear optical effects in a gaseous medium.

The most important functions of the waveguide in this context, as a beam shaping device, are to maintain a high intensity region over the entire length of the guide and have a high transmission factor. There are two requirements which need to be fulfilled in order to achieve this purpose. The first is the efficient injection of the incident laser light into the waveguide, and the second is the efficient propagation of this light along the length of the waveguide. These two concepts are very closely coupled, since the waveguide propagation characteristics depend on the injection characteristics. To facilitate a clearer understanding of the processes, ideal injection is assumed when the waveguide propagation characteristics are investigated. The ideal injection requirements are investigated before these waveguide propagation characteristics are investigated.

## 3.2 Injection requirements

The efficient injection of the incident laser light into the waveguide cavity is accomplished by focussing of the laser beam. Optimal injection is schematically illustrated in Figure 3.1.



Figure 3.1: Schematic illustration of ideal injection into the waveguide cavity.

For optimal injection, the following requirements must be met:

- Gaussian incident beam
- Directional alignment of beam path with waveguide
- Beam waist positioned at waveguide entrance:
  - Axial alignment of beam waist position with the waveguide entrance
  - Radial alignment of the beam centre with the centre of the waveguide cavity
- Beam size at waveguide entrance optimal relative to waveguide inner diameter

These requirements are discussed below in the context of the experimental situation. This experimental situation is identical to that described in Chapter 1, and refers to a Helium-Neon laser which is focussed with a thin lens. The Helium-Neon laser was used in this investigation due to its good Gaussian character. In order to measure the transmission, power measurements were taken before and after the waveguide, using a sensitive photodiode detector. The characteristics of this specific detector is available in [10]. In this investigation, the above-mentioned requirements for optimal injection were experimentally investigated. This serves to define the method of obtaining optimal transmission, which may then be applied to other laser beams for use in the Raman laser system.

### 3.2.1 Incident beam transverse mode

Ideal injection involves the use of an ideal Gaussian beam. This allows maximum coupling of the incident beam into the lowest order waveguide mode, which has the optimal waveguide propagation properties, and therefore highest transmission. The effect of different incident beam profiles has been thoroughly investigated elsewhere, in terms of the coupling between free-space modes and waveguide modes [11],[12]. For this reason, the injection of the incident laser beam into the waveguide is referred to as *mode coupling* in many texts. For ideal injection, the free-space Gaussian or  $TEM_{00}$  mode is coupled entirely into the lowest order waveguide mode, the  $TE_{10}$  mode<sup>8</sup>. This is also discussed in Section 3.3. The transverse intensity profile of the waveguide-transmitted Helium-Neon beam was experimentally measured, using the scanning slit method as discussed in Appendix B. This intensity profile is presented in Figure 3.2. The absolute transmission for this case was measured by power measurements before and after the waveguide and found to be  $\sim 80\%$ .

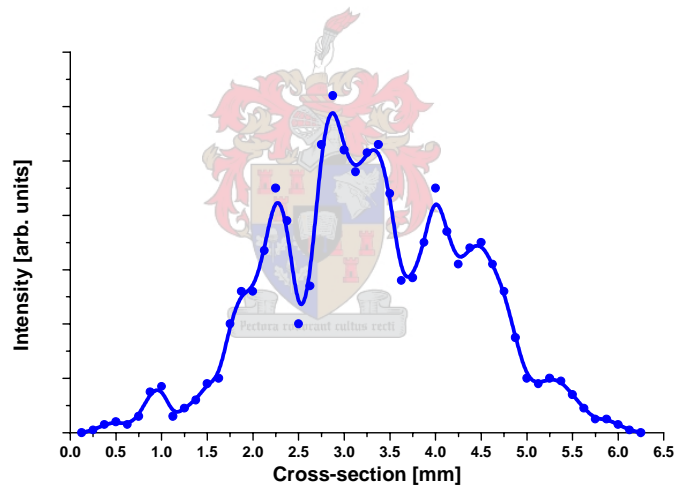


Figure 3.2: Transverse intensity profile of Helium-Neon laser after waveguide transmission: transmission factor of 80%. The line was drawn to enhance the visual appearance.

This profile does not correspond to the expected  $TEM_{00}$  mode which is theoretically emitted from the waveguide [11]. This may be due to imperfections on the inner surface of the waveguide and imperfect injection of the incident radiation. Both these factors result in the propagation of waveguide modes other than the lowest order  $TE_{10}$  mode, and the mixing of these modes results in the intensity profile observed.

<sup>8</sup> The  $TE_{10}$  intensity profile is very similar to the  $TEM_{00}$  intensity profile.

### 3.2.2 Directional alignment

This requirement is obvious, and applies to most beam shaping devices. The effect of the directional misalignment of hollow dielectric waveguides has been investigated experimentally elsewhere [10]. In this work, the qualitative effect of misalignment was investigated, in order to simplify the process of alignment. It was found that the transmitted beam mode patterns are a good indication of the amount of misalignment. In the ideal alignment situation, a small (low divergence) mode pattern (solid spot) is observed. A photograph of this mode pattern due to good alignment of the waveguide is shown in Figure 3.3. As the misalignment increases, the observed mode patterns increase in size due to the presence of higher order modes, which have larger divergences. The observed mode patterns also change: one example is the doughnut mode. A photograph of this doughnut mode, at the same distance from the waveguide, is shown in Figure 3.4. This method of observing the transmitted mode patterns was found to be a very useful and simple method of sensitive alignment of the waveguide in an experimental situation.

The process of directional alignment of the waveguide with the beam path was simplified further by the use of an iris. This iris was placed in the beam path without the waveguide in place. When the waveguide was placed in the beam path, the waveguide angle was varied until the transmitted beam passed through the iris.

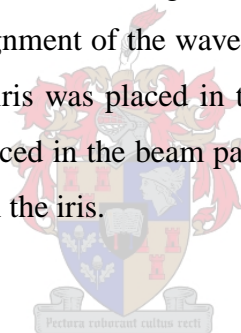




Figure 3.3: Photograph of the mode pattern of the waveguide-transmitted Helium-Neon laser beam in good alignment.

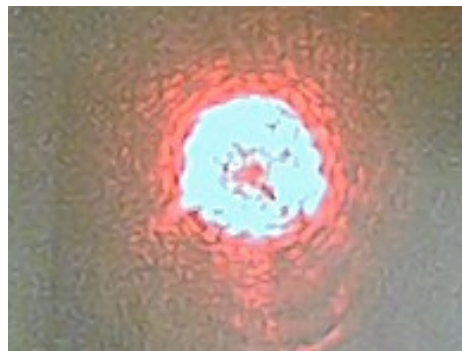
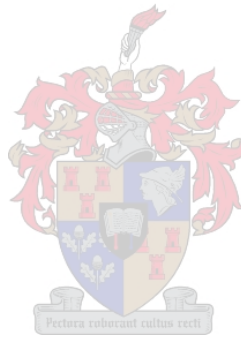


Figure 3.4: Photograph of the mode pattern of the waveguide-transmitted Helium-Neon laser beam with slight misalignment.

### **3.2.3 Beam waist alignment**

#### **Axial alignment**

It is well known that optimal injection of the beam into the waveguide requires the beam waist to be positioned axially exactly at the waveguide entrance [12],[10]. Experimental transmission measurements were attempted by moving the lens position in small increments, and thereby moving the beam waist position relative to the waveguide entrance. It was found that the directional misalignment was much more critical than the beam waist position relative to the waveguide entrance. For this reason, the experimental results are not presented here. The fact that the axial beam waist alignment is not critical is a useful result, since the focal position was found by visual inspection, which is not an extremely accurate method.

#### **Radial alignment**

In the radial direction, a slight misalignment causes a significant drop in the overall transmission. The optimal transversal alignment is thus done by visual inspection of the transmitted beam intensity. The experimental method for small transversal position changes of the waist position is by moving the focussing lens in the required direction. The focussing lens is attached to translation stages in two transversal directions. The position changes referred to here are very small, and the lens is sufficiently larger than the beam size, such that aberrations may be minimized.

### **3.2.4 Choice of waveguide inner diameter**

A smaller inner diameter waveguide, under the assumption of ideal injection and transmission, leads to a higher intensity region inside the waveguide. This is extremely desirable in view of nonlinear optical processes, which are highly intensity dependent. In this work, the waveguides available were glass capillary tubes of various inner diameters. The choice was made to use the waveguides with the smallest inner diameter: 0.6 mm. This choice corresponds to the waveguides used by others in the field of Raman lasers [13],[14].

### 3.2.5 Beam waist size relative to waveguide inner diameter

The focussed beam waist at the waveguide entrance should have an optimal size relative to the waveguide inner diameter, due to the requirements for optimal waveguide propagation. If the focussed waist size is too large, a part of the incident beam will not be injected into the waveguide. This is illustrated in Figure 3.5.

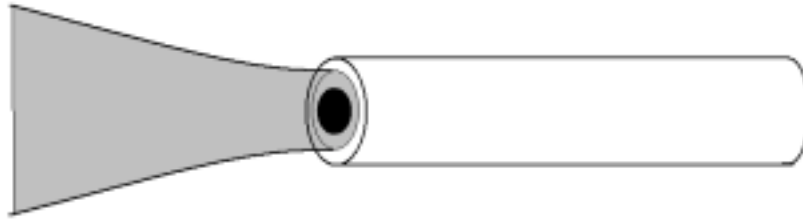


Figure 3.5: Schematic illustration of injection into the waveguide: focussed waist size too large.

If the focussed waist size is too small, the incident beam will undergo large transmission losses at the reflections from the waveguide walls. This situation is schematically illustrated in Figure 3.6.

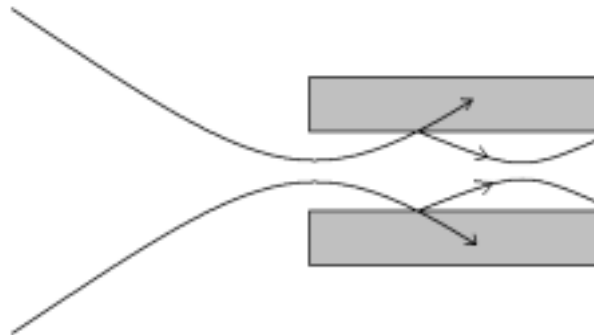


Figure 3.6: Schematic illustration of injection into the waveguide: focussed waist size too small.

The optimal waist size, such that the transmission losses at the walls are minimal, is schematically illustrated in Figure 3.7.

This optimal waist size can be determined by calculating the theoretical transmission function for a specific waveguide, which is the subject of the next section. With a given laser system, the focussing parameters which result in this optimal waist size can be calculated. However, the exact beam waist size and beam waist position in the laser resonator is rarely known, because the

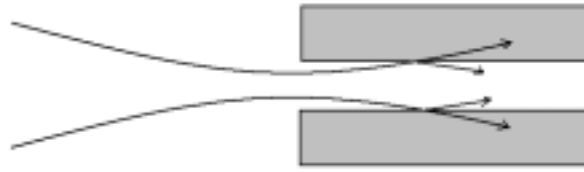


Figure 3.7: Schematic illustration of injection into the waveguide: focussed waist size optimal.

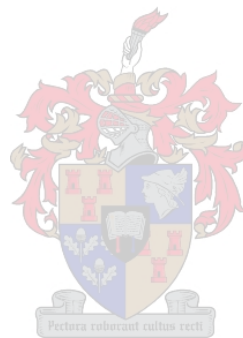
resonator parameters are usually unknown. For this reason, the typical focussing setup discussed in Chapter 1 was employed. For the purposes of finding the optimal focussed waist size for injection into the waveguide, the experimental method was to increase or decrease the focussed waist size. This was done according to the methods outlined in Chapter 1: changes in the distance between the laser and lens, or by using different focal length lenses. Changes in the focussed beam waist size also result in changes in the waist position, and thus the waveguide was continually moved to the focal point, as observed visually. The measured transmission fraction was used as a measure of the injection efficiency.

### 3.2.6 Experimental method

The experimental alignment and focussing methods outlined in the sections above can be used in exactly the same way when any laser beam is required to be focussed into the waveguide. In order to summarize the findings, the complete method is described below.

A typical focussing lens is chosen, such as  $f = 0.3$  m. This is attached to translation stages such that the lens may be moved in the axial as well as two transversal directions. An iris is placed behind the position of the waveguide, without the waveguide in place. The lens is positioned along the beam path and the focal position found by visual inspection. The waveguide entrance is placed at this focal position, with the focussed beam centrally aligned with the entrance cavity. The waveguide end is moved transversely in order to allow the transmitted beam to pass through the iris. The transmitted mode patterns are inspected, and the waveguide end aligned in order to transmit the lowest order mode, which has the lowest divergence. The lens is moved transversely in order to optimise the incident radial position, this is done by observing the transmitted beam intensity. The transmission fraction of this situation may be measured. Now the focussed beam waist size may be changed. This is done by changing the distance between the laser and the

lens, and by using different lenses. Each change of focussed beam waist size requires a complete re-alignment, as described above. In this way, the optimal experimental transmission setup for a given laser beam through the chosen waveguide may be found. Using the Helium-Neon laser, transmission up to  $\sim 95\%$  was achieved with a lens of focal length  $f = 0.3$  m.



### 3.3 Waveguide propagation

The propagation of light in a waveguide can be explained schematically in the figures in the previous section, Figures 3.6 and 3.7. A simpler model, which yields the same results, involves the representation of the incident light as rays, as illustrated in Figure 3.8. These rays are reflected from the inside surface of the waveguide, resulting in propagation along the waveguide. Since the waveguide wall material (glass:  $n \approx 1.5$ ) has a higher index of refraction than the hollow waveguide cavity (gaseous medium:  $n \approx 1$ ), total internal reflection does not occur. At each reflection the laser beam loses some of its energy due to partial transmission at the wall (Fresnel reflections).

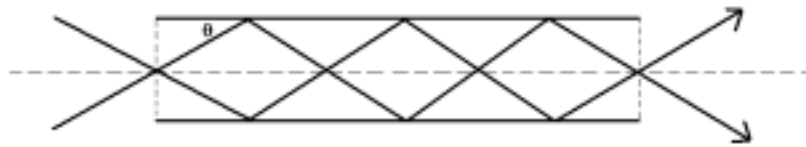


Figure 3.8: Schematic illustration of ray propagation in a waveguide.

In this description of waveguide propagation, the higher order modes in the incident beam correspond to rays which reflect at larger angles  $\theta$  [10], and thus have higher reflection losses [15]. The lower order modes in the incident beam correspond to rays with small grazing angles  $\theta$ , which thus have lower losses and higher total transmission.

The propagation theory of hollow, circular dielectric waveguides has been well established [12]. This theory describes the propagation inside the waveguide in terms of waveguide modes. The lowest order waveguide mode, which has the lowest propagation losses, is the  $TE_{10}$  mode. It may be noted that the  $TE_{10}$  intensity profile has zero values at the waveguide walls. Therefore, in the case of an ideally smooth surface, no optical damage is done to the waveguide material. During the course of this work, damage to the inner surfaces of the waveguides was not observed<sup>9</sup>. For maximal waveguide propagation, the incident Gaussian beam should thus be converted entirely to the  $TE_{10}$  mode. The optimal injection waist size for conversion of the  $TEM_{00}$  free-space mode to the  $TE_{10}$  waveguide mode can be calculated. Such an analytical model, which calculates

<sup>9</sup> Damage to the waveguides did occur at the injection cavity, where the focussed beams damaged the glass when not in good radial alignment.

the transmission of waveguides has been derived elsewhere [12]. This model, henceforth called the Transmission model, gives the transmission fraction which is denoted by  $T$ . This model was applied to the waveguides of interest in this thesis and parameter investigations were done in order to investigate the waveguide propagation characteristics in various cases of interest. According to this model, the transmission fraction  $T$  is given by (notation corresponds to that used by [12], for simplicity):

$$T = \frac{1 - e^{-F \frac{R^2}{r_0^2}}}{F} \quad (3.1)$$

where:

$$F = 1 + \frac{n^2 + 1}{\sqrt{n^2 - 1}} \frac{L}{R} \frac{1}{k^2 r_0^2}$$

and  $n$  is the waveguide dielectric material refractive index

$L$  is the length of the waveguide

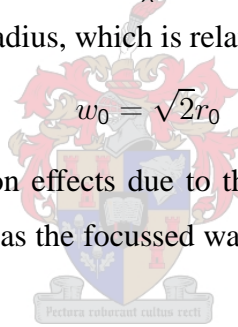
$R$  is the radius of the circular waveguide cross-section

$k$  is the wavenumber,  $k = \frac{2\pi}{\lambda}$

$r_0$  is the beam radius, which is related to the waist size  $w_0$ :

$$w_0 = \sqrt{2} r_0$$

This model neglects diffraction effects due to the finite size of the waveguide aperture, which is a good assumption as long as the focussed waist size  $w_0$  is smaller than  $\frac{1}{3}$  of the waveguide inner diameter.



The transmission of a typical waveguide, calculated using Equation 3.1, as a function of focussed waist size is given in Figure 3.9. The waveguide parameters used are typical values for the glass capillaries used in the Raman laser. The wavelength is that of the Helium-Neon laser, because this laser was used to experimentally investigate the various waveguides:

- Material: Glass  $n = 1.5$
- Length:  $L = 0.6$  m
- Radius of waveguide cavity:  $R = 0.5$  mm
- Wavelength:  $\lambda = 632.8$  nm

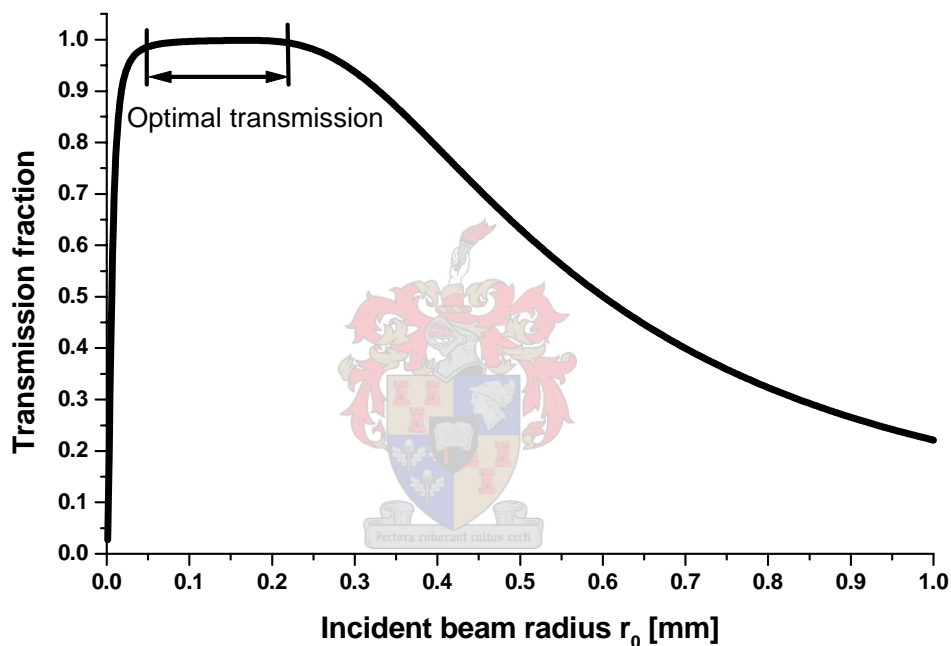


Figure 3.9: The theoretical transmission of a typical waveguide as a function of focussed waist radius.

Figure 3.9 shows that optimal transmission may be achieved by a wide range of incident beam radii. This demonstrates the fact that the focussed beam waist size is not extremely critical. It can now be seen that the focussing situation investigated in Chapter 1 corresponds to a situation for optimal waveguide transmission. The experimental focussed waist of  $w_{01} \approx 0.13$  mm which was found in Chapter 1 and applied to the various focussing parameter investigations, falls in this optimal waveguide transmission region.

### 3.4 Parameter sensitivity testing

The functional dependences of the transmission fraction on the other parameters in the Transmission model, given by Equation 3.1, allow parameter sensitivity testing to be done. This gives an indication of the usefulness of various waveguides, and the usefulness of the waveguides for different laser wavelengths.

#### 3.4.1 Length of waveguide

Long waveguides are usually desirable due to the long interaction region for nonlinear processes. Since each reflection from the waveguide wall results in losses, it can be deduced that long waveguides have lower transmission than short waveguides. Assuming an ideal inner waveguide surface, the dependence of beam waist radius on the transmission for different waveguide lengths is given in Figure 3.10. This shows that longer waveguides have a slightly more critical focussed waist size requirement. This dependence is very small and the transmission characteristics remain very good, theoretically. In reality, the attenuation is much stronger for long waveguides, due to imperfections on the waveguide inner surface which result in scattering losses. The practical situation is such that an experimental design for beam shaping will rarely require a waveguide longer than  $\sim 1 - 2$  m.

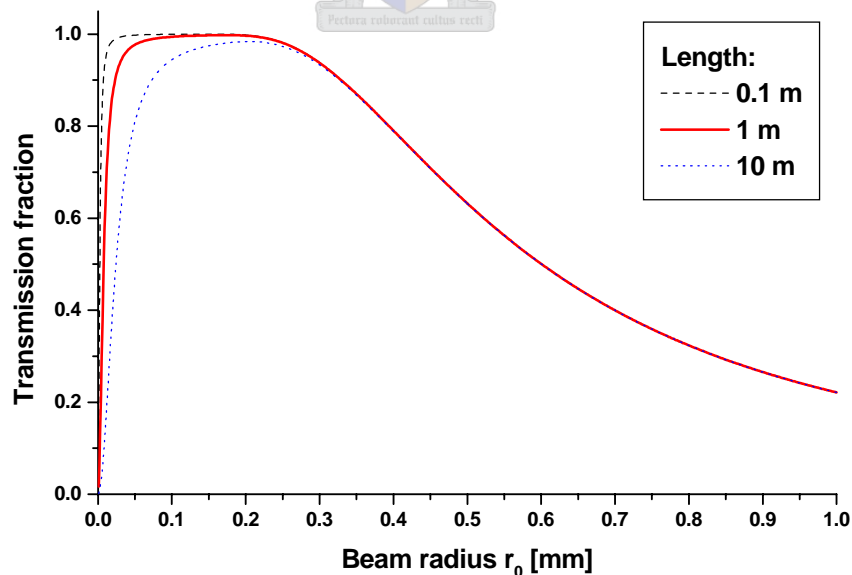


Figure 3.10: The transmission as a function of focussed beam radius, for different waveguide lengths: 0.1, 1, 10 m.

### 3.4.2 Radius of waveguide

The effect of different waveguide cavity radii was investigated, because waveguides of various dimensions were available. Keep in mind that smaller radius waveguides yield considerably higher intensities inside the waveguide, under optimal injection characteristics. Smaller radius waveguides are thus an attractive choice for nonlinear processes. The transmission as a function of focussed beam radius is given for different waveguide radii in Figure 3.11. The waveguide inner radii investigated here are typical glass capillary tube dimensions. This figure shows that small-radius waveguides require a much more critically focussed beam size, and the transmission fraction at this optimal value also drops slightly.

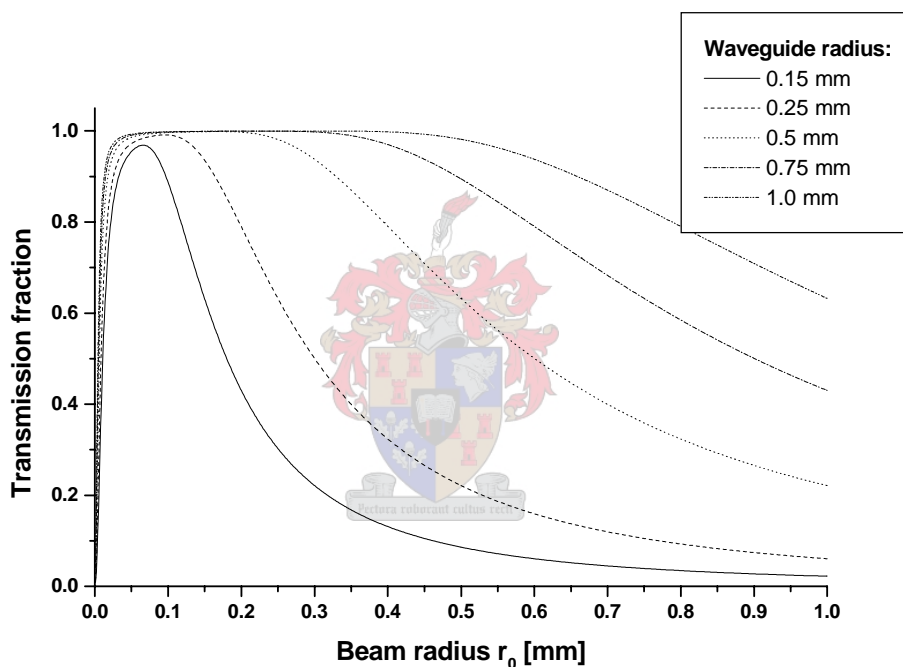


Figure 3.11: The transmission as a function of focussed beam radius, for different waveguide radii: dimensions of typical glass capillary tubes were used.

### 3.4.3 Wavelength of radiation

The transmission characteristics for different wavelengths is of importance, since laser beams of different wavelengths may be used in the same waveguide. In the application of the beam shaping method in this thesis, the Raman laser, wavelengths in the visible and near IR are required to propagate. This was investigated for different wavelengths, using the Transmission model, and the results presented in Figure 3.12. These results show very little effect of different wavelengths on the propagation characteristics. In this investigation, the slight change of index of refraction on the propagation characteristics. In this investigation, the slight change of index of refraction for the different wavelengths was neglected. The effect of different indices of refraction was investigated independently and this is presented in the next section.

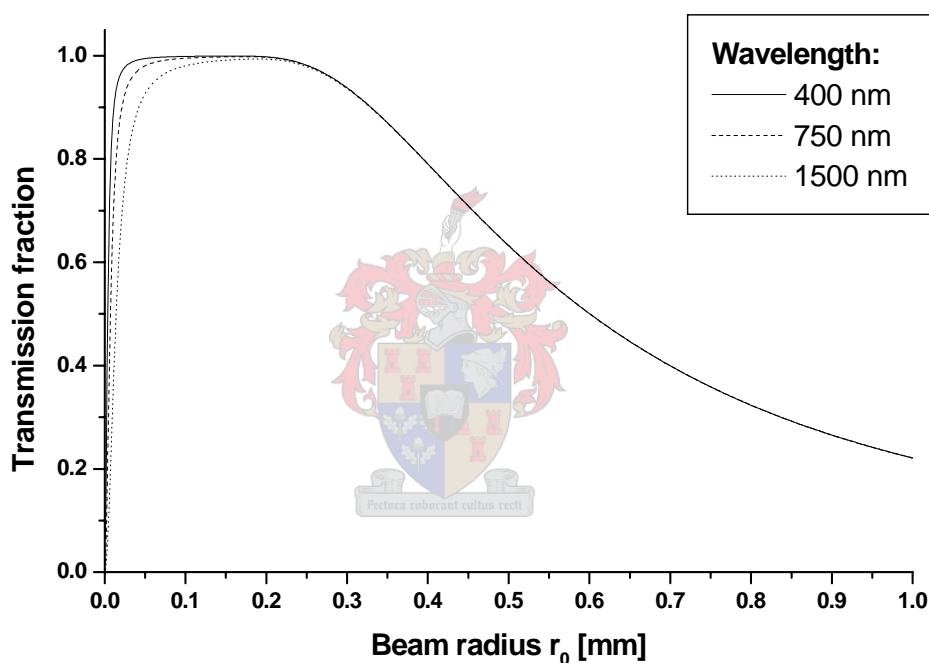


Figure 3.12: The transmission as a function of focussed beam radius for different wavelengths.

### 3.4.4 Index of refraction

The effect of different indices of refraction on the transmission function is important in two contexts. The first is the slight change of index of refraction with wavelength, as mentioned in the previous section. The second is the possible use of different dielectric materials for the waveguide. Figure 3.13 demonstrates the effect of two extreme dielectric material indices of refraction:  $n = 1.2$  and  $n = 2.6$ . This shows that the index of refraction has a negligible effect on the transmission characteristics.

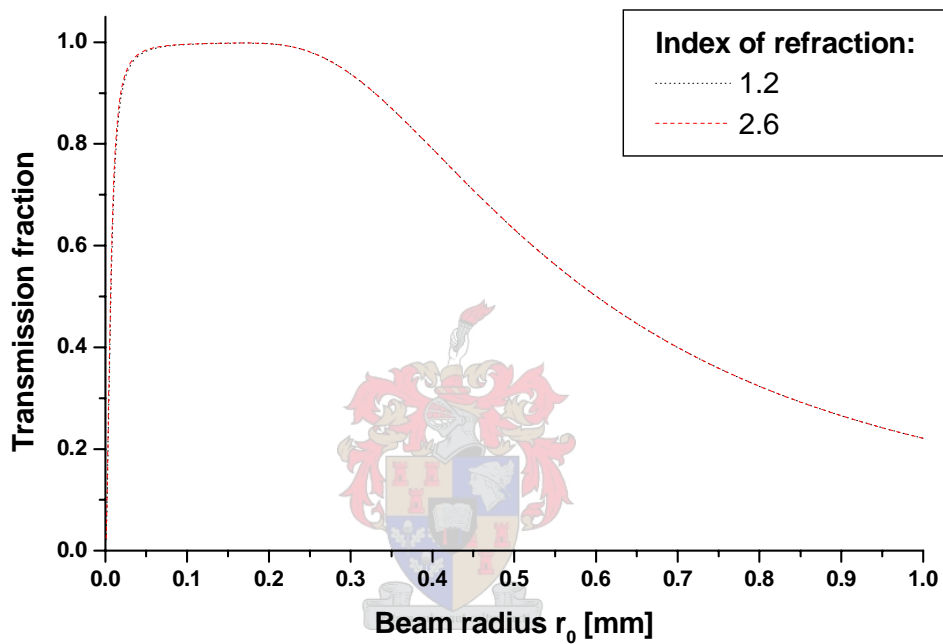


Figure 3.13: The transmission as a function of focussed beam radius for different indices of refraction.

### 3.4.5 Conclusions

The results of the parameter sensitivity tests of the waveguide transmission model serve to identify which parameters are critical to efficient waveguide propagation. It was found that the length of the waveguide has a negligible effect on the transmission characteristics. This model includes Fresnel reflection losses, and therefore the largest losses will be due to scattering from surface imperfections. If high optical quality waveguides are available, the length may be maximized for efficient beam shaping. It was also found that different wavelengths propagate equally well, in the region of interest. It was found that the index of refraction of the waveguide material does not change the transmission characteristics, and various materials may be used, as long as these materials are highly reflecting in the visible wavelength region. The critical parameter which has been identified is the inner radius of the waveguide. Smaller inner diameter waveguides are desirable due to the higher intensities which may be maintained. However, as the inner radius decreases, the required focussed waist size becomes more critical and the peak transmission also decreases slightly.



## 3.5 Experimental investigation

### 3.5.1 Introduction

The experimental method of alignment and beam waist size optimisation as discussed in Section 3.2 was applied to the different laser beams to be used in the Raman laser (refer to Chapters 4 and 5). The optimal transmission values were measured, in order to characterize the waveguides for use with the given laser systems. The choice was made to use the waveguides of inner diameter 0.6 mm and length 60 cm in the Raman laser. Of the readily available glass capillary tubes, these have the smallest inner diameter. Larger waveguides were also investigated but were found to have comparable transmission values. The laser systems which were investigated as pump sources were two different dye lasers and an optically pumped parametric oscillator (OPPO). In this investigation, the waveguide was placed inside the Raman cell. This makes accurate alignment more challenging, since the waveguide entrance cannot be observed when the waveguide is placed inside the Raman cell.



### 3.5.2 Dye laser

Transmission experiments were done with dye laser beams at  $\lambda = 440$  nm and 540 nm. The characteristics of these lasers are given in Sections 5.2.1 and 5.3.1 respectively. In order to find the transmission values, energy measurements were taken with the Laser Precision Corporation Rj-7620 energy-ratiometer and the RjP-735 energy probe, before and after the waveguide respectively. Since the dye laser is pulsed, averaged measurements were taken. In this case, a lens of focal length  $f = 0.4$  m was found to result in optimal transmission of approximately 75%. This is significantly lower than the 95% transmission obtained with the Helium-Neon laser.

The laser beams of the Helium-Neon and the dye lasers differ in wavelength and beam quality. The Transmission model has been well-established and is known to be correct, and the investigation of the functional dependence in Section 3.4.3 has shown the wavelength dependence to be negligible. The only other difference between the laser beams of the Helium-Neon and the dye laser, are the beam quality of each. It may therefore be concluded that the poor (non-Gaussian) beam quality of the dye laser beam was responsible for the loss of approximately 20%.

The Raman cell was fixed to the optical table and the cell was closed off by two  $CaF_2$  windows. The measured transmission of this system was repeatedly found to be in the region of 50 – 60%<sup>10</sup>.

The Fresnel reflection loss  $R$  at each  $CaF_2$  window surface<sup>11</sup> is given by [15]:

$$R = \frac{\mu \frac{n_t - n_i}{n_t + n_i} \lrcorner_2}{\mu \frac{n - 1}{n + 1} \lrcorner_2} = \frac{\mu \frac{1.435 - 1}{1.435 + 1} \lrcorner_2}{\mu \frac{1.435 - 1}{1.435 + 1} \lrcorner_2} = 0.032$$

The calculation of the total transmission of the Raman laser system in this case, including 2 reflective surfaces, the waveguide and another 2 reflective surfaces results in a value of  $\sim 66\%$ . The discrepancy between the experimental values of 50 – 60% and the theoretical value of  $\sim 66\%$  can be explained by the difficulty of aligning the waveguide with the beam path when it is placed inside the Raman cell. With a high-precision alignment technique for the Raman cell, up to  $\sim 66\%$  transmission should be achieved in this configuration.



<sup>10</sup> The alignment of the waveguide and Raman cell with the beam path was done repeatedly, with both dye laser systems.

<sup>11</sup> Index of refraction of  $CaF_2$  at 540 nm is  $n = 1.435$ .

The beam profile of the transmitted beam for the case of the dye laser at 440 nm (and 60% total transmission) was measured using the scanning slit method, and the resulting intensity profile at a distance of 40 cm from the Raman cell exit window is shown in Figure 3.14. A photograph of the corresponding mode pattern is given in Figure 3.15.

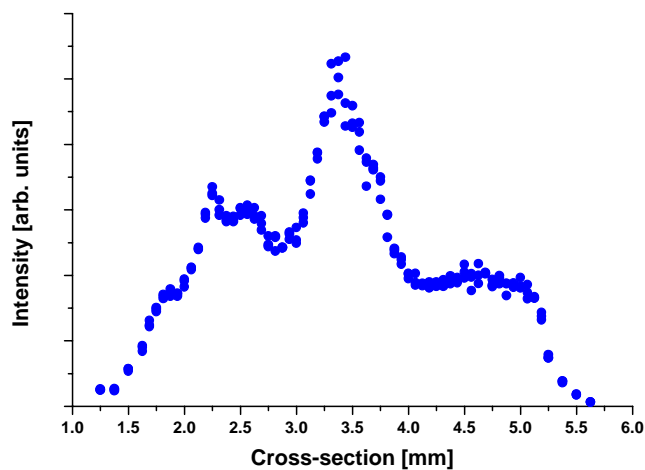


Figure 3.14: Measured intensity profile of dye laser after the Raman laser configuration, including windows and waveguide, total transmission  $\sim 60\%$ .

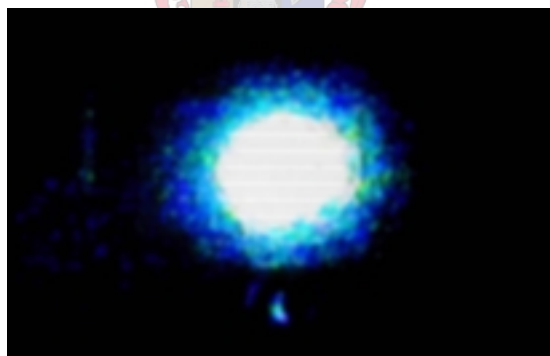


Figure 3.15: Photograph of the mode pattern of dye laser after the Raman laser configuration, including windows and waveguide, total transmission  $\sim 60\%$ .

The transmission of the waveguide was investigated as a function of incident pulse energy, using the dye laser at 540 nm. The reason for this investigation is the possibility of heating of the waveguide walls by the laser pulse energy, and thus a possible change in the transmission characteristics. This experiment was conducted at a repetition rate of 10 Hz and the incident dye laser energy was varied by adjusting the voltage supply of the excimer pump laser. The results of this investigation are shown in Figure 3.16, where the pump energy refers to the pulse energy of the dye laser. It can be concluded that heating of the waveguide does not have an effect on the transmission in this regime.

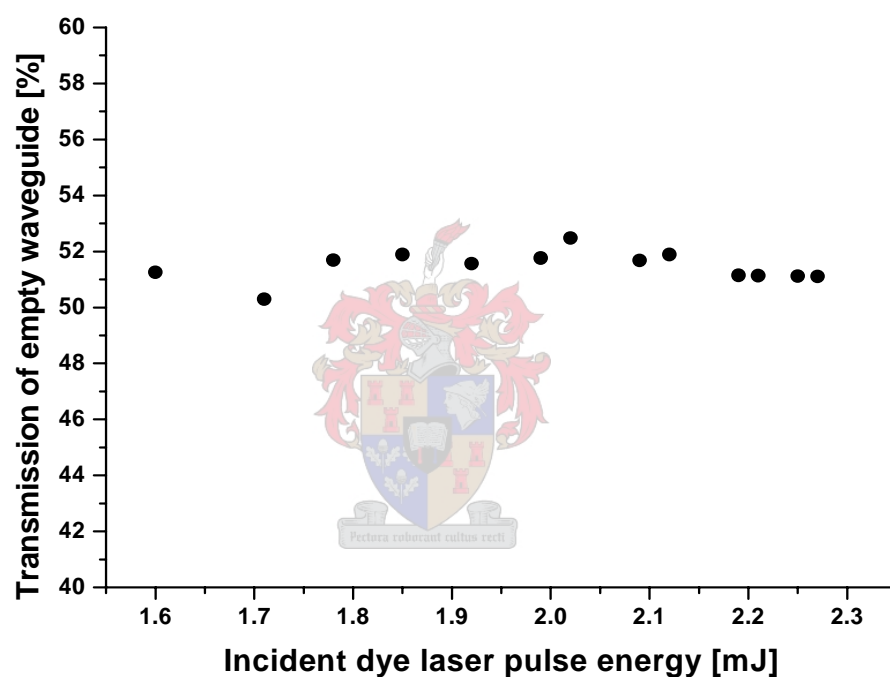


Figure 3.16: Transmission of empty waveguide as a function of incident pulse energy, using the dye laser at 540 nm and 10 Hz repetition rate.

The effect of different repetition rates on the transmission of the waveguide was also investigated, since this may also lead to heating effects. This experiment was conducted with a dye laser pulse energy of 2.1 mJ. The results are presented in Figure 3.17. It can be concluded that the transmission does not greatly differ for different repetition rates.

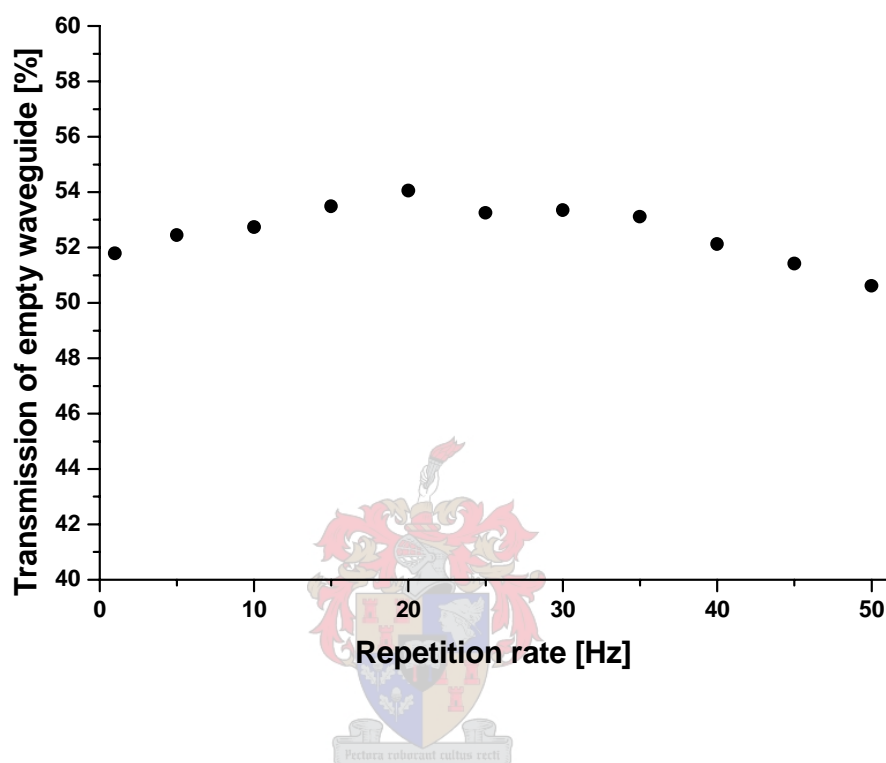


Figure 3.17: Transmission of empty waveguide as a function of repetition rate, using the dye laser at 540 nm and 2.1 mJ incident pulse energy.

### 3.5.3 Optically pumped parametric oscillator

The optically pumped parametric oscillator (OPPO) was investigated as a source for the Raman laser, and thus the waveguide transmission characteristics were investigated. The optimal focussing lens was found to be  $f = 0.3$  m in this case. The characteristics of the OPPO system are given in Section 5.4.

The beam quality of the OPPO laser beam was poor, resulting in less efficient mode coupling and a lower waveguide transmission fraction of  $\sim 40\%$ . Nevertheless, the OPPO pulse energies were  $\sim 10$  mJ, resulting in experimental transmitted pulse energies up to  $\sim 4$  mJ. Since the pulse lengths were 8 ns FWHM, the peak powers were an order of magnitude larger than those of the dye laser systems<sup>12</sup>. This is desirable for stimulated Raman scattering as will be discussed in the next chapter. The waveguide can thus be regarded as a useful beam shaping device for the OPPO laser beam, for use in the Raman laser. The poor beam quality can be illustrated by a photograph of the mode pattern, shown in Figure 3.18.



Figure 3.18: Photograph of the beam spot of the OPPO laser tuned to  $\lambda = 440$  nm, illustrating the poor beam quality.

<sup>12</sup> Peak power ignores the spacial size of the beam. Using identical waveguide dimensions, the intensities generated inside the waveguide are thus also an order of magnitude larger than with the dye laser systems.

# Chapter 4

## Stimulated Raman Scattering

### 4.1 Introduction

The process of Stimulated Raman Scattering (SRS) was utilized to create a Raman laser, also known as a Raman shifter. A pump laser beam undergoes stimulated vibrational Raman scattering in molecular  $H_2$ , which results in the formation of laser radiation at shifted wavelengths. Using a tunable laser as the pump source, the Raman-shifted laser radiation is also tunable. In conjunction with a tunable laser system in the visible region of the spectrum, this system allows easy access to the near and middle IR, making it a valuable tool for the spectroscopy of molecules and atoms.

The goal of this work was to characterize the Raman laser in conjunction with the available tunable sources. The Raman laser is a relatively simple, small and cost-effective method of obtaining tunable laser radiation in the infrared and even in the ultraviolet, when a visible tunable source is available. In this work, the viability of the Raman laser as a source of tunable, pulsed infrared laser radiation was investigated, for use in future spectroscopic studies. Raman lasers have been widely used as an efficient method of extending the tuning range of given tunable sources. The interest in the viability of the Raman laser here lies in the fact that the available tunable dye lasers, which are 20 years old, have much lower pulse energies than most new dye lasers. The viability of using such low pulse energies demonstrates the usefulness of the Raman laser as a wavelength-shifting device.

The available OPPO system is a broadly tunable system (from 400 – 2000  $\mu\text{m}$ ) and was also investigated as a possible source for the Raman laser. Even though the OPPO system yields tunable laser radiation in the infrared, use of the Raman laser may be preferred in some instances, due to (possibly) higher efficiencies in certain cases.

In both instances, with dye lasers and the OPPO, the tuning range is not restricted and tunable infrared from 0.7 to 7  $\mu\text{m}$  has been achieved by Schmidt and Hartig [14], using a dye laser as pump source for their Raman laser, also using a glass waveguide.

The experimental results allow conclusions to be made about the viability of the system for a given application, and lay the foundation for the efficient operation of the system in future work.

## 4.2 Theoretical description

### 4.2.1 First-order Stokes formation

Stokes-shifted Raman scattering is schematically illustrated with a quantum-transition diagram in Figure 4.1. An incident photon of frequency  $\nu_0$  is scattered by a scattering molecule with ground state  $a$  and excited state  $b$ . The molecule absorbs some of the energy of the incident photon, such that the scattered photon has a frequency of  $\nu_0 - \Delta\nu_r$ . The Raman mode frequency  $\Delta\nu_r$  is the frequency difference between the two states of the molecule:  $a$  and  $b$ . The virtual state is not a state of the molecule, but rather a representation of the scattering process. This has the advantage that a photon of any incident frequency such that  $\nu_0 > \Delta\nu_r$  can be scattered, and the frequency difference between the incident and scattered photon is equal to  $\Delta\nu_r$ , independent of the frequency of the incident photon. Since the molecule absorbs some of the incident energy ( $h\Delta\nu_r$ ), this is an inelastic scattering process. The above-mentioned description applies to Stokes scattering. The inverse process of anti-Stokes scattering may also occur. In this process, the molecule is initially in the excited state  $b$ , the incident photon is inelastically scattered such that it absorbs energy from the molecule, and thus the molecule is left in the ground state  $a$ . Both the processes may be spontaneous or stimulated.

The stimulated Raman scattering process differs from the corresponding spontaneous process in that the scattered radiation has the following properties:

- Coherence
- Directionality
- Exponential intensity dependence (linear dependence for spontaneous Raman scattering)
- Parametric process, i.e. the phase-matching criterion is automatically satisfied.

For these reasons, laser radiation can easily be produced. For the SRS process, the growth of the Stokes wave in the small-signal limit (neglecting saturation effects) can be described by:

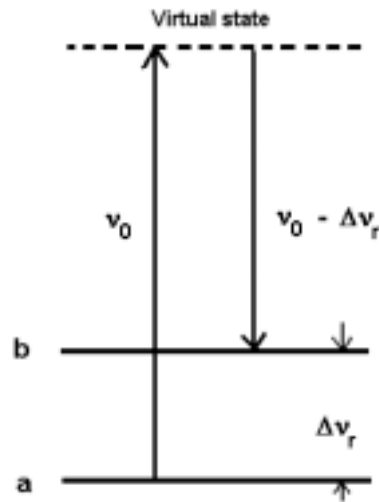


Figure 4.1: Quantum-transition diagram representing Stokes-shifted Raman scattering.

$$I'(\nu', z) = I'(\nu', 0) e^{Gz} \quad (4.1)$$

where  $I'(\nu', z)$  is the Stokes intensity that is created at frequency  $\nu'$  and interaction distance  $z$

$I'(\nu', 0)$  is the background Stokes intensity, which is provided by black-body radiation and spontaneous Raman scattering, or a seeding laser lasing at the Stokes frequency  $\nu'$ .  $z$  is the interaction length.

$G$  is the Raman gain coefficient and is given by [16] as:

$$G = N_a \sigma \frac{\lambda'^2}{h\nu' \Delta\nu'} I_0 \quad (4.2)$$

where  $N_a$  is the number of scattering molecules in the initial energy level

$\sigma$  is the differential cross-section of SRS for the given scattering molecule

$\lambda'$  is the wavelength of the Stokes-shifted radiation

$$\nu' = \frac{c}{\lambda'}$$

$\Delta\nu'$  is the Raman linewidth

$I_0$  is the pump laser intensity, approximated as a constant in the small-signal

limit

## 4.2.2 The Raman gain coefficient

The description of the Raman gain coefficient in Equation 4.2 allows the following conclusions to be made:

- The gain coefficient is linearly dependent on the number of scattering molecules ( $N_a$ ) and thus the gas pressure. The pressure dependence was investigated experimentally and results presented in the next chapter.
- The gain coefficient is linearly dependent on the differential cross-section of the gas used. The gas used was molecular hydrogen, which has a relatively large differential cross-section compared to other gases [17].
- The gain coefficient is linearly dependent on the pump laser intensity, in the small-signal limit. This partly explains the requirement for a beam shaping technique.

Note that no conclusions are made about the wavelength dependence, because the differential cross-section is wavelength dependent. This dependence is complex and a more complete description may be found in [16] or [17]. A quantification of this dependence is unnecessary in this context. It is sufficient to know that the Raman gain coefficient decreases with increasing wavelength [18],[19].

The Raman gain coefficient as given by Equation 4.2 does not contain a bandwidth dependence. This has been investigated elsewhere, where it has been found that the pump laser bandwidth does not influence the Raman gain coefficient in most cases of interest [20]. Within this regime, the Stokes-shifted radiation has the same bandwidth as the pump laser. The limitation of this regime of gain independence on bandwidth has been quantified by [20] as the acceptance bandwidth:

$$\Delta\nu_{\max} = \frac{c}{4(n_p - n_s)L} \quad (4.3)$$

where

$c$  is the velocity of light

$n_p, n_s$  are the indices of refraction of the pump and Stokes frequencies in the Raman medium

$L$  is the length of the Raman gain medium

If the pump laser bandwidth is larger than the acceptance bandwidth, the Raman gain coefficient decreases. The form of this decrease has not yet, to my knowledge, been quantified.

A calculation of the acceptance bandwidth for the Raman laser investigated in this work was not done, because the indices of refraction of hydrogen for different wavelengths and hydrogen pressures are not readily available. The index of refraction of any gas is  $n \sim 1$ . However, Trutna *et al* [20] quote a value of  $4.9 \text{ cm}^{-1}$  as the minimum value of the acceptance bandwidth for hydrogen in the pressure range of  $0 - 800 \text{ kPa}$ , at a wavelength of  $1.064 \text{ }\mu\text{m}$ . This is used as a general comparative value in this work.

### 4.2.3 Higher-order Stokes formation

The formation of the first Stokes wave from the pump has been described, in the small-signal limit: the first Stokes wave grows exponentially out of the pump laser wave. This process involves only partial depletion of the pump laser wave. The first Stokes wave may also act as the pump for the second Stokes wave, with an identical exponential dependence and also a partial depletion. This second Stokes wave can then act as the pump for the formation of the third Stokes wave, and so on. The formation of the different orders of Stokes have a temporal dependence which is experimentally investigated and discussed in Section 5.2.4. A characteristic of the Stokes formation, which was experimentally verified in the above-mentioned section, is that the higher order Stokes pulses have shorter pulse lengths than the lower order or pump pulses. A schematic illustration of the higher-order Stokes formation using a quantum-transition diagram is given in Figure 4.2.

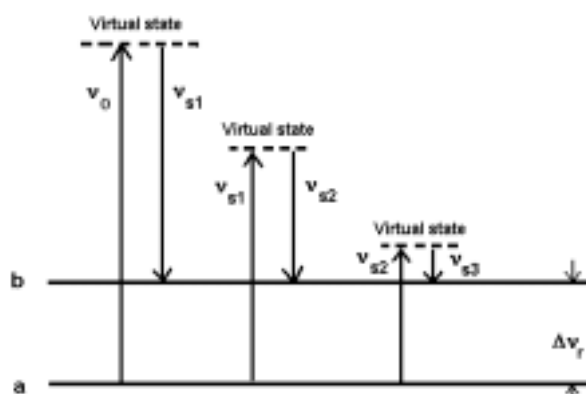


Figure 4.2: Quantum-transition diagram representing three orders Stokes-shifted Raman scattering.

The equivalent frequency-shifting process, for three orders of Stokes, is shown schematically in Figure 4.3. This figure illustrates the important concept of the constant frequency shift of  $\Delta\nu_r$ , which is a characteristic of the Raman medium. Note that in this figure, the pump is in the blue region of the spectrum, the first Stokes in the green, the second Stokes in the red, and the third Stokes in the near IR. This corresponds to one of the experimental situations, as discussed in the next chapter. Another characteristic of the Stokes formation is the fact that the bandwidth of the Stokes corresponds to the bandwidth of the pump [20].

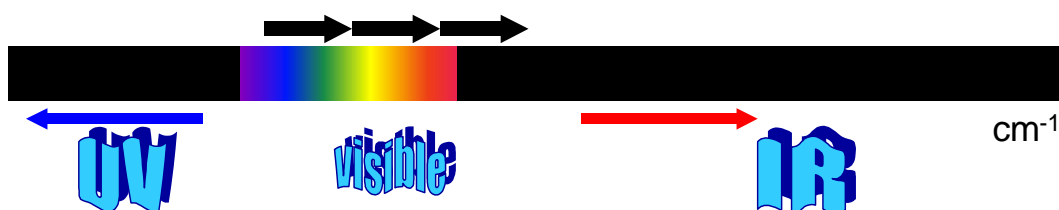


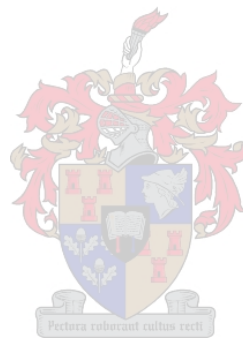
Figure 4.3: Schematic illustration of the frequency-shifting process of three orders of Stokes formation.

#### 4.2.4 Four-wave mixing effects

The description of stimulated Raman scattering in the previous two sections is the simplest form of the process. In reality, the process is usually accompanied by four-wave mixing effects. This involves intricate coupling between the different Stokes and anti-Stokes waves, due to four-wave frequency mixing. A detailed description of the various different third-order nonlinear susceptibilities which result in the formation of each Stokes or anti-Stokes order is extremely complex. A calculation of the expected Stokes outputs would not yield useful results, since small changes in any of the factors in the Raman gain coefficient result in exponentially larger changes to the Stokes output and the mixing of the different orders of Stokes and anti-Stokes. More complete theoretical descriptions may be found in [16] and [17]. It is sufficient to know that the different orders of Stokes and anti-Stokes are in competition with each other, and that this competition should be manipulated in some way in order to maximize the formation of a chosen order of Stokes or anti-Stokes. Therefore, the yield of Stokes output cannot be calculated and should be investigated experimentally.

### 4.2.5 Threshold

The intensity of the Stokes wave has been shown to have an exponential dependence on the Raman gain coefficient and the interaction length. Ignoring losses in the system, no physical threshold for this process exists. However, the lower section of the exponential dependence results in a very small Stokes intensity, which is not observable or measurable. Thus, an *effective threshold* exists for the intensity of the incident pump laser, below which no observable Stokes intensity is generated. In addition to this effect, losses of the system also contribute to a higher effective threshold value. An experimental investigation of the threshold was done and the results are presented in the next chapter, Section 5.3.4.



## 4.3 Design of the Raman laser

The design of the Raman laser which was investigated in this thesis is discussed in the context of the theory dealt with in the previous section. The basic requirement is that efficient Stokes-shifted laser radiation can be generated. This should be done in a simple, cost-effective and flexible way.

### 4.3.1 Beam shaping

A very simple method of laser beam shaping for maximizing the SRS process in a gaseous medium is the use of a hollow dielectric waveguide. The efficient application of the hollow waveguide results in a high intensity region  $I_0$  over a long interaction region  $z$ . Thus, two of the factors in the exponential dependence of the SRS process are maximized. The waveguide has been characterized for efficient use in the Raman laser in Chapter 3. Besides allowing a longer interaction length and high intensity region for the pump laser beam, the different Stokes orders are also confined efficiently to the interaction region. Experimentally, no SRS was observed without the use of the waveguide.

### 4.3.2 Gaseous medium

The choice of a gaseous medium for the Raman laser is due to various factors. The first is the fact that molecular gases are *centrosymmetric*, which means that nonlinear processes of the even orders cannot be excited [21]. Therefore, since SRS is a third-order nonlinear process, this allows less competition (due to no second order processes) and more efficient stimulated Raman scattering. The second reason for the choice of a gaseous medium is the transparency of gases in the visible and infrared range, which is the wavelength range considered in this work. Gases also have high damage thresholds compared to other media.

Although the density of gases is much lower than solids, this density is variable by adjusting the pressure. This was found to have advantages in the Raman laser, as discussed in the next chapter. Since the density  $N_a$ , which is directly proportional to the gas pressure, occurs in the Raman gain coefficient, high pressures should be used to maximize this factor. This determines the design of the Raman cell as a high-pressure gas cell.

Molecular hydrogen was chosen as the medium for SRS in the Raman laser. The first reason has been discussed in Section 4.2.2: a relatively large susceptibility for SRS and thus a

large differential cross-section  $\sigma$  in Equation 4.2. The second reason for the choice of hydrogen is the large vibrational frequency shift, or Raman mode frequency:  $\Delta\nu_r = 4155 \text{ cm}^{-1}$ .

### 4.3.3 Wavelength range

Using the dye laser as pump with the dye Coumarin-440 (tunable in the range  $\sim 420 - 460 \text{ nm}$ ), the wavelength regions which may be reached by the Raman laser are illustrated schematically in Figure 4.4.

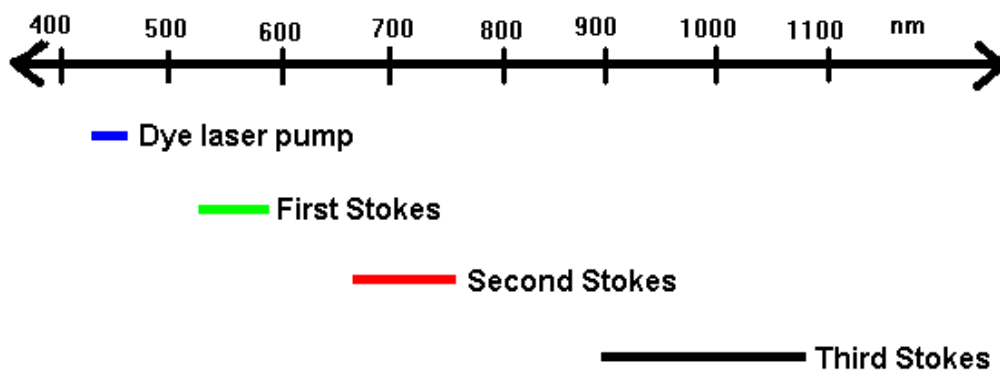


Figure 4.4: Illustration of the wavelength regions attainable with the dye laser at around 440 nm, including the corresponding tunability ranges.



It can be seen that the higher order Stokes have larger tuning ranges. This can be explained by the fact that the Stokes shift is a fixed frequency shift, but the Stokes wavelength is dependent on the pump wavelength. The calculation of the Stokes-shifted wavelength is done as follows:

$$\begin{aligned}
 \nu_{S1} &= \nu_P - 4155 \text{ cm}^{-1} \\
 \frac{1}{\lambda_{S1}} &= \frac{1}{\lambda_P} - 4155 \text{ cm}^{-1} \\
 \lambda_{S1} [\text{cm}] &= \frac{1}{\frac{1}{\lambda_P [\text{cm}]} - 4155 \text{ cm}^{-1}} \quad (4.4)
 \end{aligned}$$

Similarly, the second Stokes component may be calculated by replacing the pump wavelength with the first Stokes wavelength.

#### 4.3.4 Competition between Stokes orders

As mentioned in Section 4.2.4, the different orders of Stokes and anti-Stokes are in competition with each other. The importance of this competition is the fact that the formation of a chosen order of Stokes may be optimised by manipulation of certain factors. This required manipulation of the factors is different for every system, and should thus be investigated experimentally.

If a certain wavelength region is required, there are various possible ways of reaching this wavelength region with the Raman laser. These different methods refer to the different orders of Stokes, from correspondingly different pump wavelengths. This process is schematically illustrated in Figure 4.5, which shows how a wavelength in the red region of the spectrum may be reached by first Stokes formation due to a pump in the green region, or by second Stokes formation due to a pump in the blue region. The relative efficiency of these two methods is determined not only by the competition between the different Stokes orders, but also by the efficiency of the pump laser wavelengths, which depends on the dye efficiencies in the case of dye lasers.

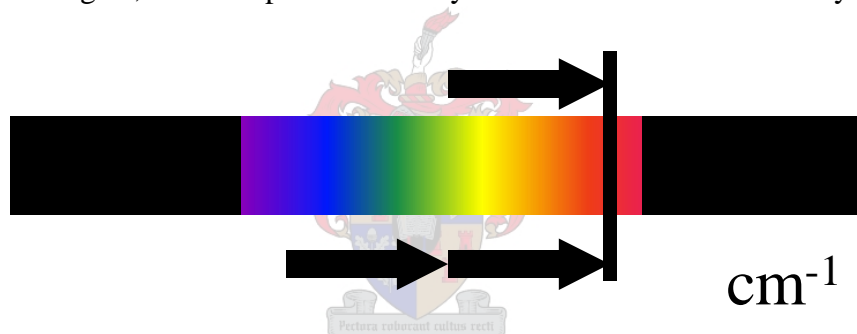


Figure 4.5: Schematic illustration of two methods of reaching a certain wavelength region with the Raman laser, by first or second Stokes formation.

## Chapter 5

# Experimental characterization

### 5.1 The Raman laser system

The Raman laser system under consideration here consists of a cylindrical high pressure stainless steel cell, 83 cm in length and having a 4 cm inner diameter, closed off by removable  $CaF_2$  windows<sup>13</sup> of diameter 25 mm and thickness 6.35 mm. A hollow dielectric waveguide is placed inside the Raman cell. The waveguide chosen, as discussed in Section 3.5, was a glass waveguide of length 0.6 m and inner radius 0.3 mm. The Raman cell has a three-way ball valve which allows a connection to the hydrogen gas supply, a closed position and a connection to a rotation pump for removal of the gas. The cell has vertical adjustment on each of two stands, and transversal alignment is done by moving the cell by hand. Further alignment is done as outlined in Section 3.2.6.

The system can easily be assembled and disassembled and mobility is thus an advantage. During the course of this thesis work, the system was moved to various laboratories. An optically pumped parametric oscillator (OPPO), a frequency-tripled Nd:YAG laser and two dye laser systems were successfully used as pump laser sources for generating shifted wavelengths. The experimental results obtained and the subsequent discussions of the different pump laser systems are presented individually. This is followed by general experimental conclusions. The experimental setup is similar in each case: this is illustrated in Figure 5.1.

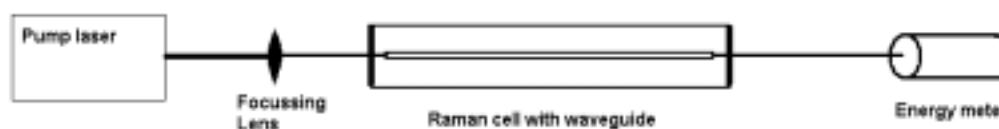


Figure 5.1: Schematic illustration of the experimental setup.

<sup>13</sup>  $CaF_2$  is transparent in the range 0.13 – 12  $\mu\text{m}$ [22].

## 5.2 Dye laser at 440nm

### 5.2.1 Experimental conditions

The dye laser under consideration is pumped by a XeCl excimer laser at 308 nm, giving approximately 180 mJ per pulse in approximately 30 ns FWHM. The dye laser energy was measured with the Laser Precision Corporation Rj-7620 energy-ratiometer and the RjP-735 energy probe, and found to be in the region of 2.5 – 3 mJ for the wavelength  $\lambda = 440$  nm, using the dye Coumarin-440. The spectral response of this probe is constant for the wavelength region 0.18 – 3  $\mu\text{m}$  ( $\pm 0.5\%$ ) [23]. Using the wavelength 440 nm as pump, the Stokes wavelengths generated are 538 nm, 694 nm and 974 nm for the first, second and third Stokes, respectively. This calculation was done with Equation 4.4. The experimental situation corresponds to the wavelength ranges demonstrated in Section 4.3.3, in Figure 4.4.

### 5.2.2 Observation of SRS

Stokes-shifted radiation was observed and the different orders separated using Schott filters. At the time of this experimental investigation, suitable filters were not available to separate the second and third Stokes wavelengths. A discussion of the filters used and the method of extracting the required data from the measured data is presented in Appendix D. The beam profile of the generated second Stokes (and possibly including some third Stokes) was measured, using the scanning slit method - this is presented in Figure 5.2. The corresponding mode pattern is given in Figure 5.3.

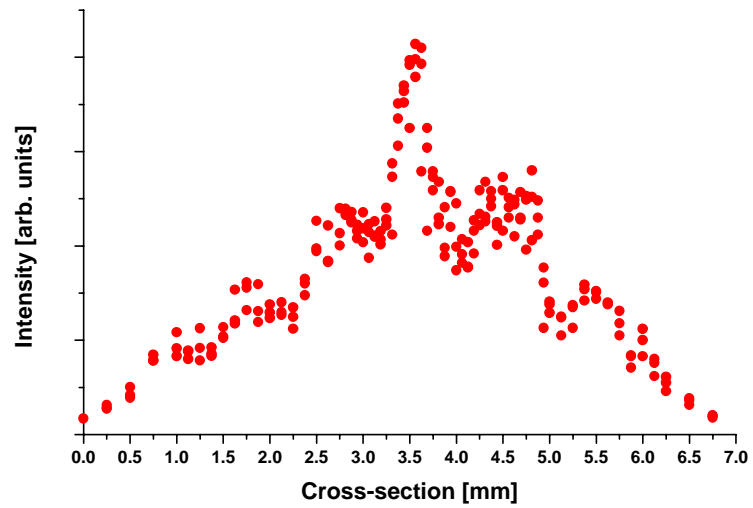


Figure 5.2: Measured intensity profile of the second Stokes radiation at 694 nm.



Figure 5.3: Photograph of the mode pattern of the second Stokes radiation at 694 nm.

### 5.2.3 Pressure dependence

The pressure of the hydrogen in the Raman cell has an effect on the Raman gain coefficient, given by Equation 4.2. As has been discussed, the different orders of Stokes are in competition with each other. The experimental measurements of the pressure dependence of the different Stokes orders illustrate this concept, which results in optimal pressure regions for the generation of the different Stokes orders. These results were obtained with the dye laser at 440 nm and 2.8 mJ pulse energy, with total Raman cell transmission of 60%. The results are presented in Figure 5.4. The first Stokes signal reached a peak value around 800 kPa, where negligible 2nd and 3rd Stokes was measured. At higher pressures, the first Stokes signal was partially depleted and the second and third Stokes signal reached a peak value at around 1400 kPa. This is most likely the peak due to the second Stokes, while the peak at around 2300 kPa is, in all probability, due to the third Stokes signal. From the results of this investigation, it can be concluded that the pressure in the cell, which is easily varied, can be used as a control parameter in the Raman laser in order to select one of the Stokes orders.

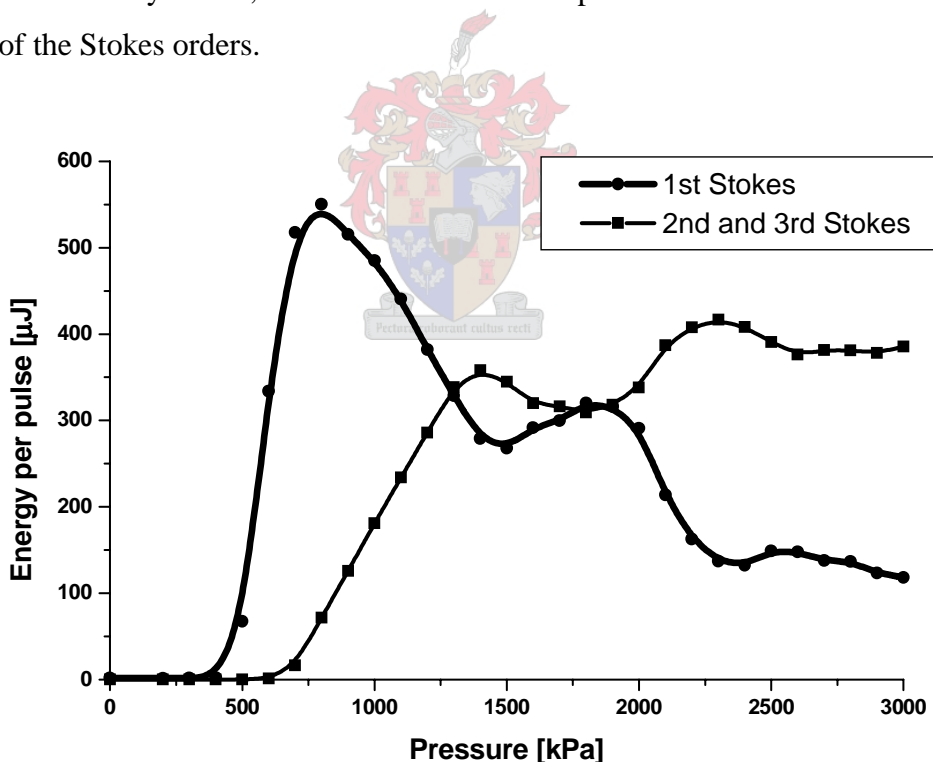


Figure 5.4: Measured Stokes pulse energy as a function of hydrogen pressure.

The growth of the first Stokes signal as a function of pressure was measured again, using a different alignment situation. The comparison of results is given in Figure 5.5. The total transmission through the Raman laser system, which is an indication of the pulse energy available for SRS, is 1.8 and 1.7 mJ for the two different measurements. It can thus be seen that the higher incident energy results in a steeper growth of the Stokes wave as a function of pressure. The slight difference in peak value between the two cases cannot be quantified, due to the experimental error margin of the energy meter<sup>14</sup>. The growth of the lower energy measurement is less steep and its peak is found at a slightly higher pressure. It can also be noted that the higher energy measurement generates a second peak at almost 2000 kPa. This second peak is possibly due to four-wave mixing effects. From these results, the optimal conversion efficiency to the first Stokes was found to be approximately 30 – 35 %.

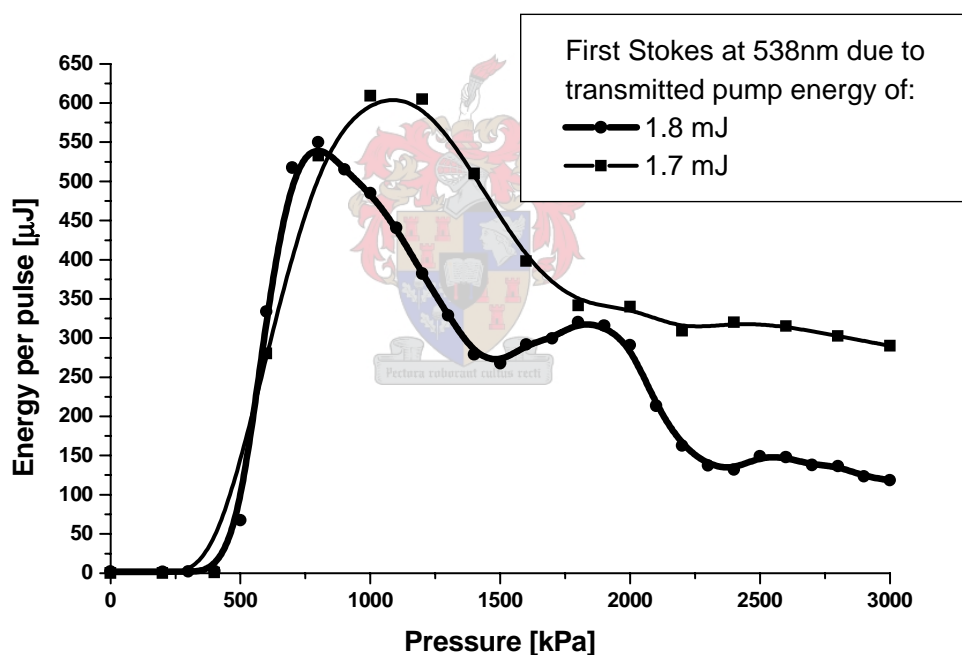


Figure 5.5: Measured first Stokes pulse energy as a function of pressure for two pump pulse energies.

<sup>14</sup> A different radial position of the beam on the energy meter head results in a different absolute energy value.

Three measurements of the second Stokes signal pressure dependence were done for different alignment situations. This is presented in Figure 5.6. Once again it can be seen that the slope and the optimal pressure peak changes for different pump energy values. From these results, the optimal conversion efficiency to the second Stokes was found to be approximately 20%.

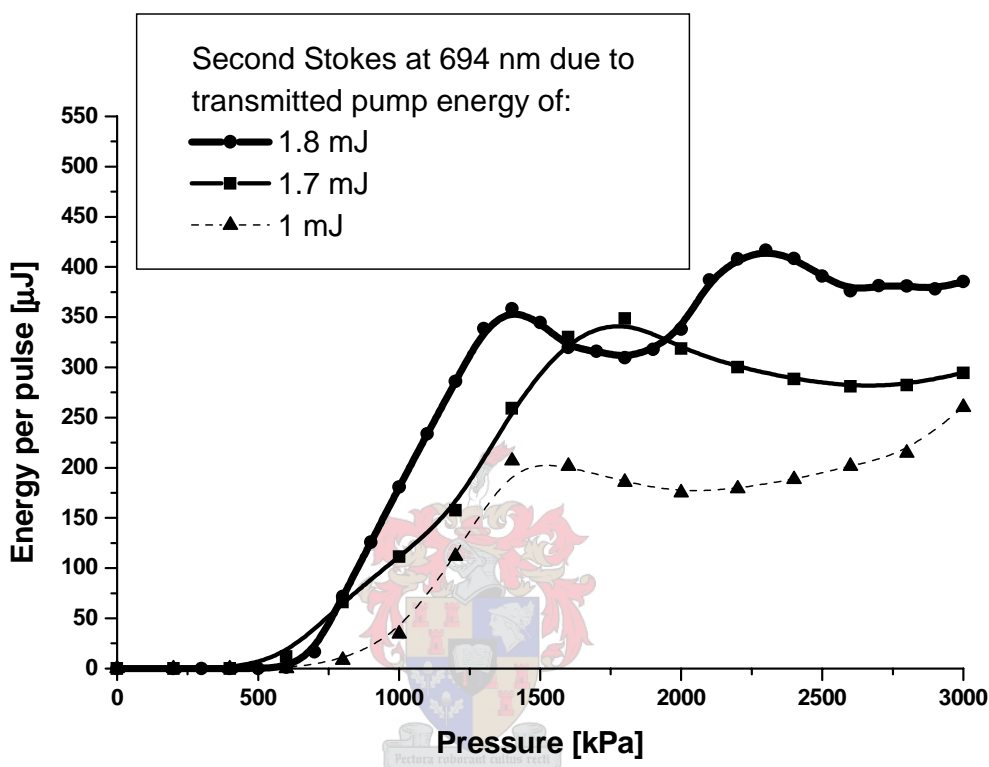


Figure 5.6: Measured second (and possible third) Stokes pulse energy as a function of pressure for three pump pulse energies.

In conclusion, the pressure dependence of the Stokes-shifted signal demonstrated the fact that the pressure may be used efficiently as a wavelength-selective control parameter. In order to optimise the formation of a given Stokes signal, the optimal pressure peak needs to be found by experimental investigation.

### 5.2.4 Temporal dependence

The generated Stokes pulses in the above experimental situation were measured with a high-speed silicon photodiode (Thorlabs DET210) and Tektronix TDS-520 oscilloscope. The oscilloscope was triggered on the pump laser, in order to observe the relative delay, if any, between the different Stokes pulses. The pulses were separated using the method outlined in Appendix D and corrections for the relative spectral response of the detector was done. The results are presented in Figure 5.7. A delayed effect is observed, which may be attributed to the threshold condition of SRS, refer to Section 4.2.5. The initial pump pulse grows to a peak value, above the threshold for SRS, after which it is partially depleted by the formation of the first Stokes pulse. This first Stokes pulse in turn acts as the pump for the growth of the second Stokes pulse. The irregular pulse shape is an inherent quality of the dye laser, due to mode beating. It can be seen that the Stokes-shifted pulses become shorter for every order of Stokes.

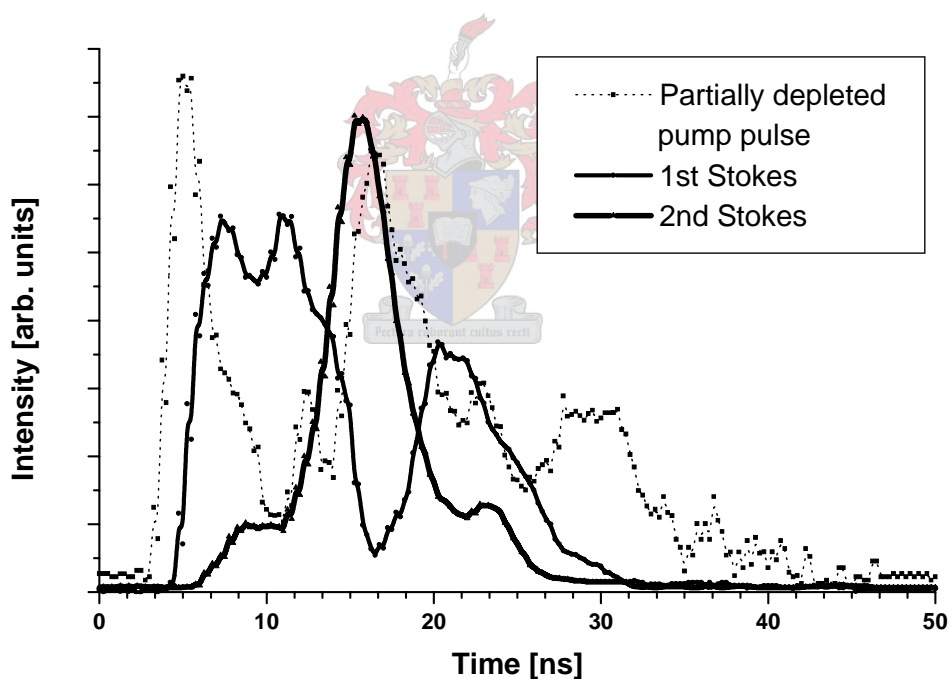


Figure 5.7: Measurements of the partially depleted pump pulse, the corresponding first Stokes pulse and the second (and possibly third) Stokes pulse.

Figure 5.8 shows typical transmitted dye laser pulses with and without SRS. This illustrates the partial depletion of the pump pulse by the growth of the Stokes orders. It is also clearly illustrated that the Stokes formation only starts after the initial pulse rises above a certain threshold value.

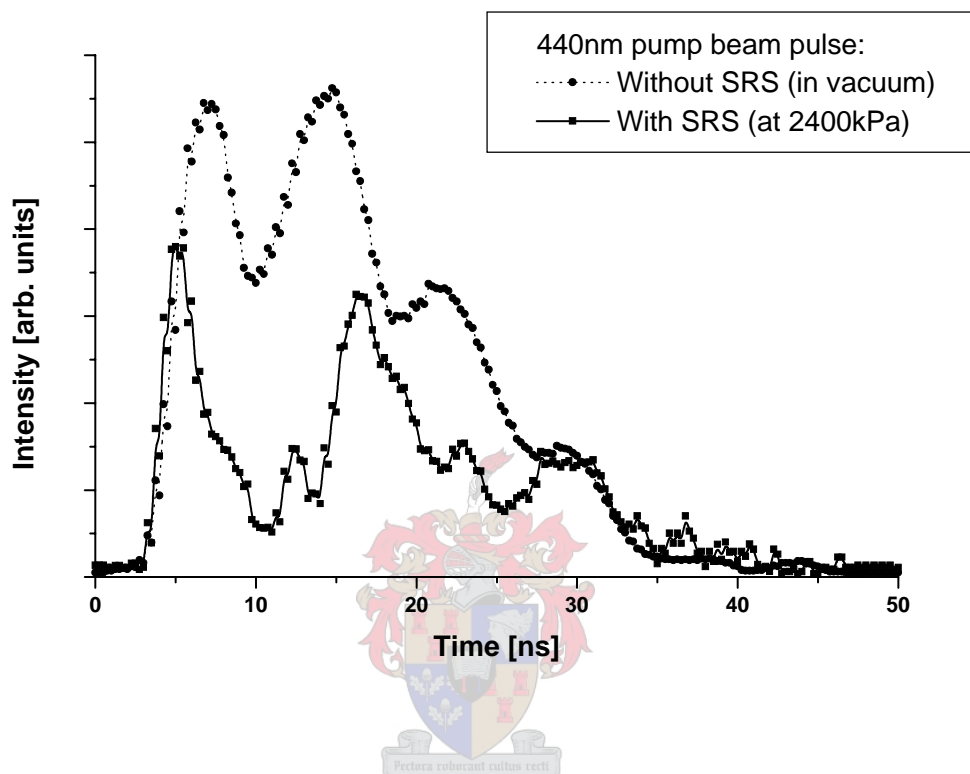


Figure 5.8: Measurements of the pump pulse with and without hydrogen, illustrating the partial depletion of the pump pulse due to SRS.

## 5.3 Dye laser at 540nm

### 5.3.1 Experimental conditions

In the work presented in this section, a different dye laser system and different XeCl excimer laser was used than in the previous investigations. The experimental setup was identical, with the exception of the XeCl excimer laser's maximum pulse energy of 140 mJ.

Using the same energy probe and meter, the dye laser pulse energy was found to be in the region of 1 – 2 mJ for the wavelength  $\lambda = 540$  nm, using the dye Coumarin-540. The energy per pulse was varied in the range 1 – 2 mJ by varying the excimer laser pulse energy. The reason for the use of a pump wavelength of 540 nm is because this results in a first order Stokes wavelength at 696 nm, which corresponds to the second Stokes in the experimental situation in the previous section, 694 nm. This is of interest for the investigation of the efficiency of generating a certain wavelength, in this case around 695 nm, by either first or second Stokes formation. This is discussed and illustrated in Section 4.3.4. In this investigation, the appropriate filters for complete separation of the different wavelengths was available.

### 5.3.2 Observation of SRS

The formation of the first-order Stokes at 696 nm was observed visually, and various measurements were taken. A photograph of the Stokes formation is given in Figure 5.9. It can be seen that the 540 nm (green) is cut off by the filter, and the transmitted Stokes wavelength at 696 nm is visually observed as a dark red spot.

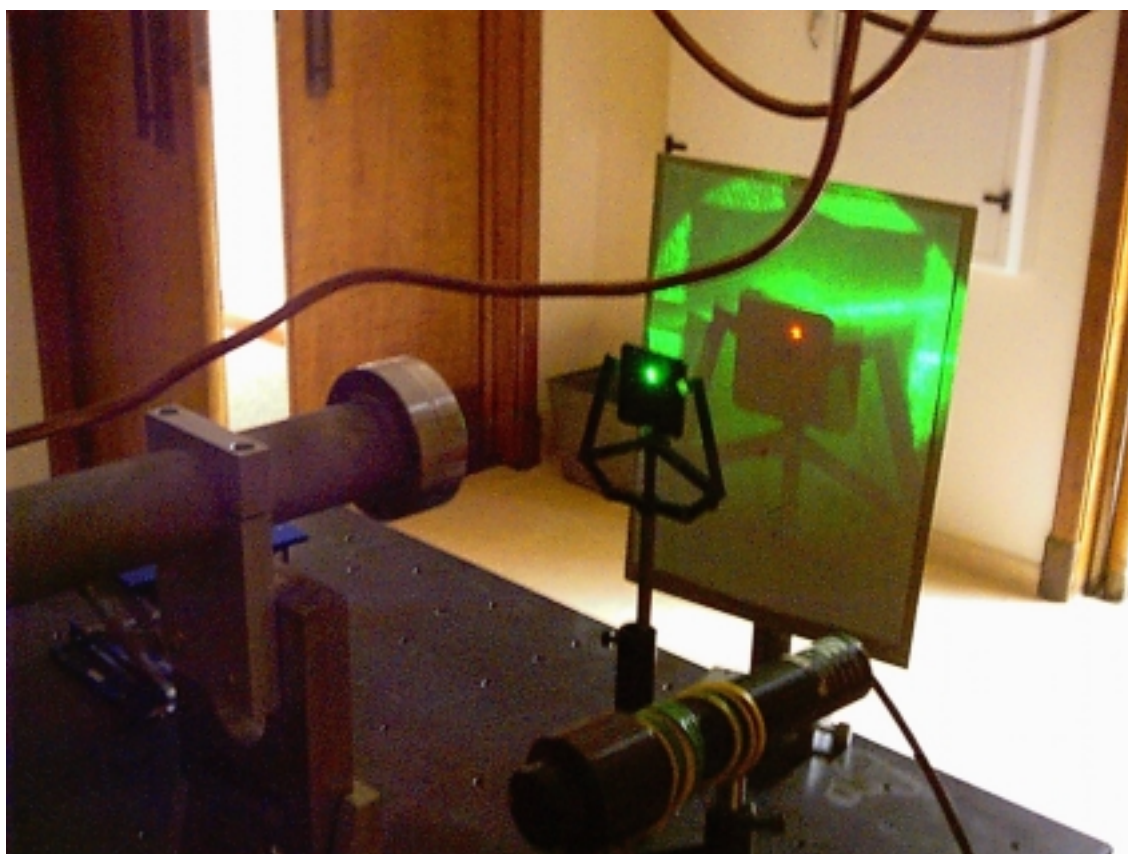


Figure 5.9: Photograph of first Stokes formation at 696 nm, due to a dye laser pump at 540 nm.

### 5.3.3 Pressure dependence

The investigation of the pressure dependence of the first Stokes energy was done for different incident dye laser energies. The results are presented in Figure 5.10. This demonstrates the fact that higher incident energies yield higher Stokes-shifted energies. The optimal pressure peak for first Stokes formation is observed to be at high pressures in this case, such as 2600 kPa for 2.25 mJ incident energy. It can also be deduced that the peak for first Stokes formation shifts to lower pressures as the incident energy is increased, in this regime. The conversion efficiency to the first Stokes was found to be approximately 20%, by taking into account the 53% waveguide transmission factor in this case.

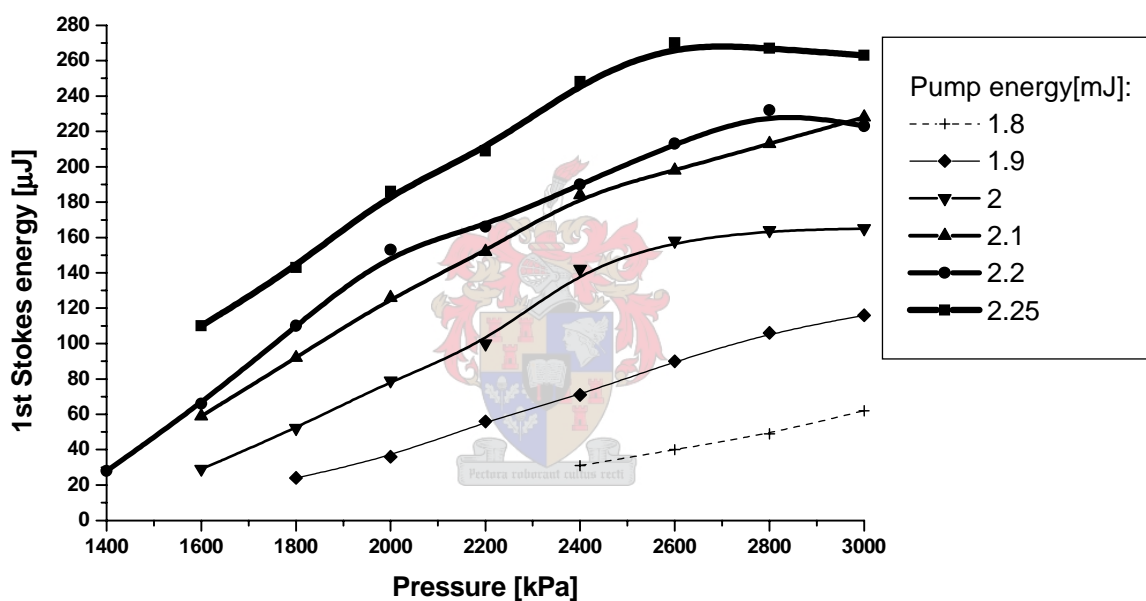


Figure 5.10: Measurements of the first Stokes pulse energy as a function of pressure, for different incident dye laser energies.

### 5.3.4 Threshold investigation

The Stokes energy as a function of dye laser pump energy, at a fixed pressure of 3000 kPa, is given in Figure 5.11. The figure contains measurements for two different alignment situations. The first measurement corresponds to a transmission of  $\sim 53\%$  and the second to  $\sim 60\%$ . It can be seen that, as expected, the better alignment situation results in higher Stokes energies at the same incident pump energy values. The theory of SRS predicts an exponential growth as in Equation 4.1 in the small-signal limit. Experimentally, the growth of the Stokes intensity as a function of incident intensity corresponds to a small section of the exponential dependence and can thus be approximated as a linear dependence. Similar results have been reported by various researchers [13],[14]. By assuming a linear dependence, an effective threshold value can be found. This effective threshold is discussed in Section 4.2.5. The thresholds for the two cases under consideration here are: 1.63 and 1.29 mJ for measurements 1 and 2 respectively. The theoretical threshold intensity may be calculated from this, by using the waveguide cross-sectional area (using  $r = 0.3$  mm) and the FWHM of the dye laser pulse (30 ns). Since the input energy is the total energy of the dye laser incident on the waveguide, the transmission factors of 0.53 and 0.6 are included in the calculation - only the energy coupled into the waveguide is utilized. The respective thresholds are found as approximately:  $1 \times 10^7$  W/cm<sup>2</sup> and  $0.9 \times 10^7$  W/cm<sup>2</sup>.

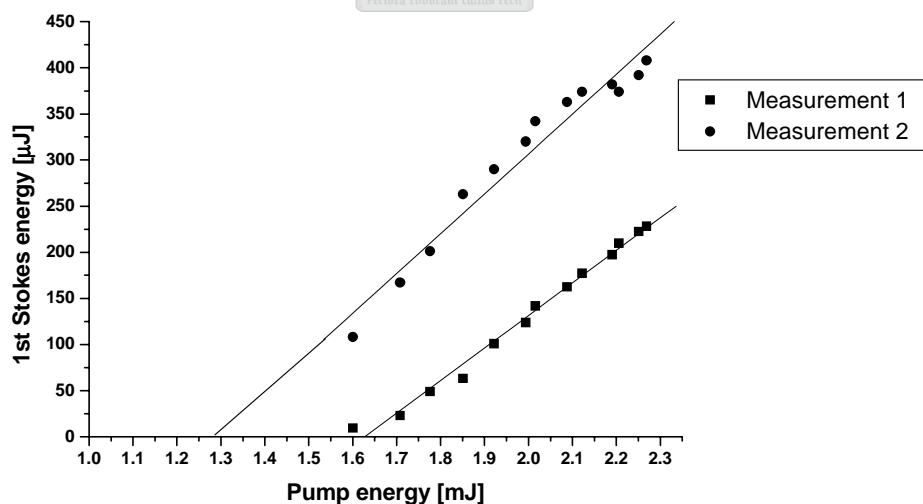


Figure 5.11: Measurements of the Stokes pulse energy as a function of incident dye laser pulse energy, illustrating the effective threshold of SRS. The two measurements correspond to different alignment situations.

Figure 5.12 demonstrates the pulse-to-pulse standard deviation of the Stokes-shifted energy measurements (solid circular data points) as a function of incident pulse energy. The corresponding first Stokes energy (hollow square data points) is also plotted, in order to show the growth above the threshold. It can be seen that as the incident energy increases further above the threshold, the Stokes pulse-to-pulse deviation decreases. The reason for this is the nature of the threshold condition: near the threshold, one pulse may generate a large amount of Stokes while the next pulse may generate very little Stokes. This may be explained by the fact that the SRS process is dependent on the amount of background radiation available at the Stokes frequency. This amount of background radiation naturally fluctuates, which results in a larger pulse-to-pulse deviation at low Stokes energies. As the incident energy is increased, the Stokes output becomes more stable. It is thus desirable to operate the Raman laser sufficiently above the threshold. The dye laser pulse-to-pulse deviation was measured to be 2 – 3%.

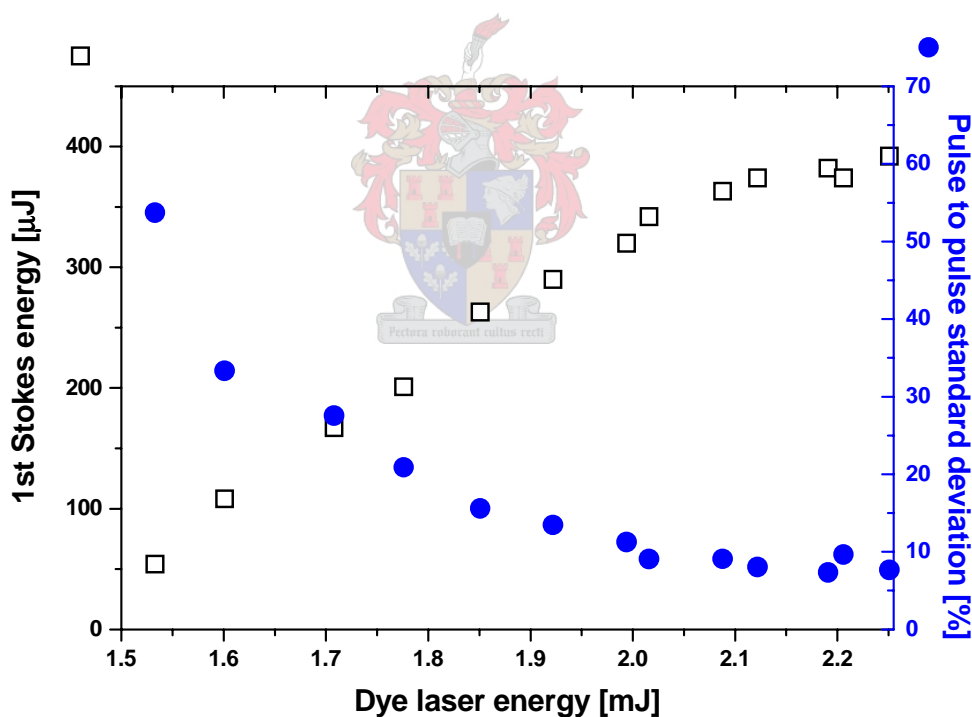


Figure 5.12: Measured pulse-to-pulse deviation as a function of incident energy (solid circular points), illustrating unstable operation near the threshold. The corresponding Stokes energy is also shown (hollow square points).

## 5.4 Optically pumped parametric oscillator

### 5.4.1 Experimental conditions

The optically pumped parametric oscillator (OPPO) is pumped by the frequency-tripled output from a Nd:YAG laser, which consists of an oscillator and one amplifier stage. The oscillator is seeded (end-pumped) with a cw diode laser. The two harmonic generators, which are placed after the amplifier, are optimised for the generation of the frequency-tripled wavelength of 355 nm. The OPPO is currently operated without a grating or dye laser seed. The parametric BBO<sup>15</sup> crystal is placed inside a resonator, which consists of two flat mirrors. These windows may be adjusted for optimal OPPO output. It was observed that the beam quality of the OPPO output is poor, and critically dependent on the adjustment of the resonator windows. Tunability is achieved by changing the angle of the BBO crystal with respect to the pump laser beam. The tunability is controlled by computer.

The power meter used was the Fieldmaster GS power meter. The probe is only sensitive above  $\sim 0.9$  mJ for the given pulses, of approximately 10ns FWHM, at 10Hz. The relative spectral response was corrected in real time, by adjusting the wavelength on the Fieldmaster. The reason for the use of the Fieldmaster rather than the Precision Laser Corporation energy meter used in the previous investigations, is possible damage to this probe head, due to the higher peak powers - as a result of the shorter pulse lengths ( $\sim 8$  ns) and higher pulse energies ( $\sim 10$  mJ). Calculation of the peak power density yields a value of  $\sim 1.25$  MW/cm<sup>2</sup>, which is more than the specified 1 MW/cm<sup>2</sup> damage threshold.

---

<sup>15</sup>  $\beta$ -Barium borate

## 5.4.2 Tunability and energy measurements

The OPPO output energy was measured from 400 nm to 1650 nm, and the results are presented in Figure 5.13. This illustrates the broadband tunability of the system. At the time these measurements were taken, the Nd:YAG pump laser was not operating optimally, and since then higher OPPO pulse energies have been measured.

There are three different resonator window pairs, which have reflection coatings optimal for different wavelength ranges. The different tuning ranges are correspondingly indicated by blue, green and red data points. The BBO crystal allows two wavelengths to be generated simultaneously, at slightly different exit angles. These correspond to the signal and idler signals as illustrated in the figure. These two signals are easily separated by an iris. The specified tuning range of the OPPO is from 400 – 2200 nm. Experimental measurements above 1650 nm was not achieved in this case, due to optical damage of the resonator windows.

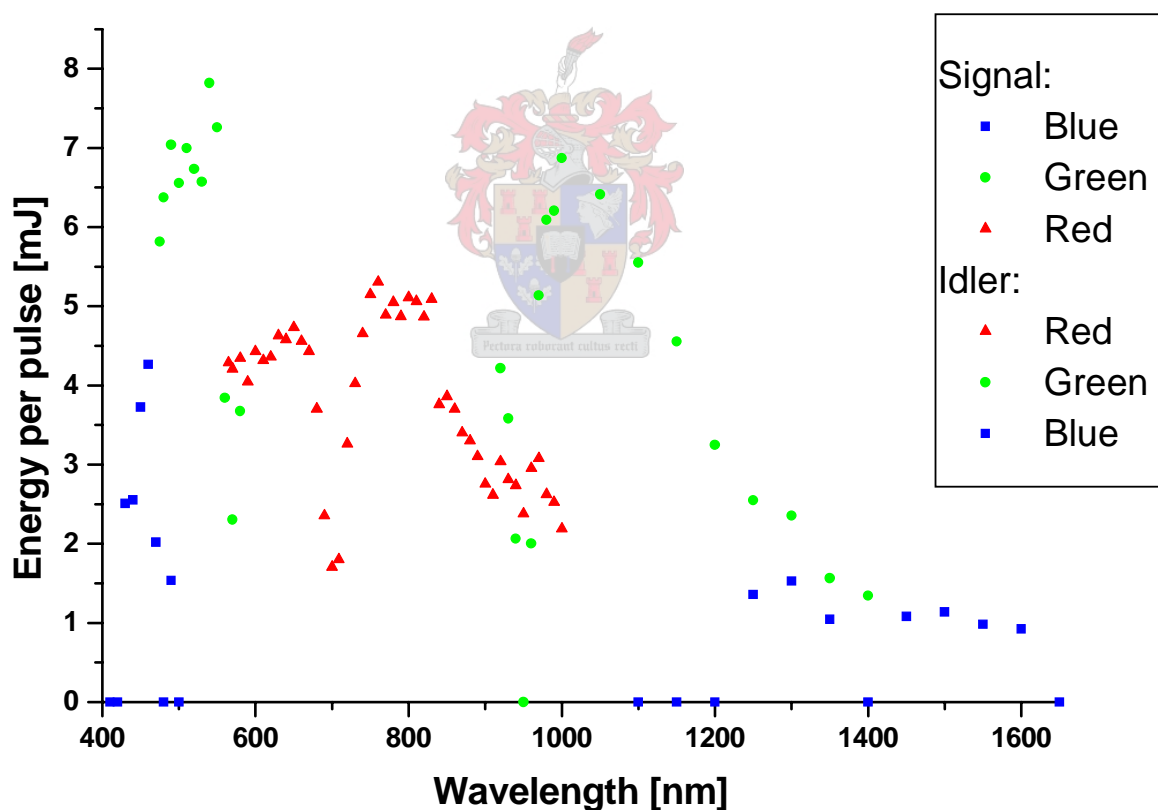


Figure 5.13: Measurements of the OPPO pulse energy as a function of wavelength: the blue, green and red indicated regions correspond to the resonator windows used.

### 5.4.3 Observation of SRS

Using a pump wavelength of 440 nm, first Stokes formation was visually observed at 538 nm. The pulse energy of the Stokes output was too low to be measured with the given apparatus. In order to demonstrate the conversion of visible wavelengths to the IR, 600 nm was chosen as pump and the resulting Stokes wavelength at 799 nm was observed with an IR-sensitive material. The Stokes formation was very weak and a large pulse-to-pulse deviation could be observed with the IR-sensitive material (near the threshold). For this reason, the energy could not be measured directly. The pulse-shapes were measured with a high-speed photodiode (Thorlabs DET210) and Tektronix TDS-520 oscilloscope. The partially depleted pump pulse at 600 nm was measured with a neutral-density filter in front of the photo-diode, in order to attenuate the signal. The Stokes pulse at 799 nm was measured without any attenuation. The results, which are therefore not on the same intensity scale, are presented in Figure 5.14. The measurements were taken relative to the trigger of the Nd:YAG pump laser. The step-like appearance of the measurements is due to the oscilloscope. Similar to the dye laser results, a delayed effect is observed. The Stokes shifted pulse is generated after the pump pulse has risen above a threshold value, after which the Stokes pulse grows and the pump pulse is partially depleted by this growth. This delayed process again demonstrates the effect that the Stokes pulse has a shorter pulse length than the pump pulse.

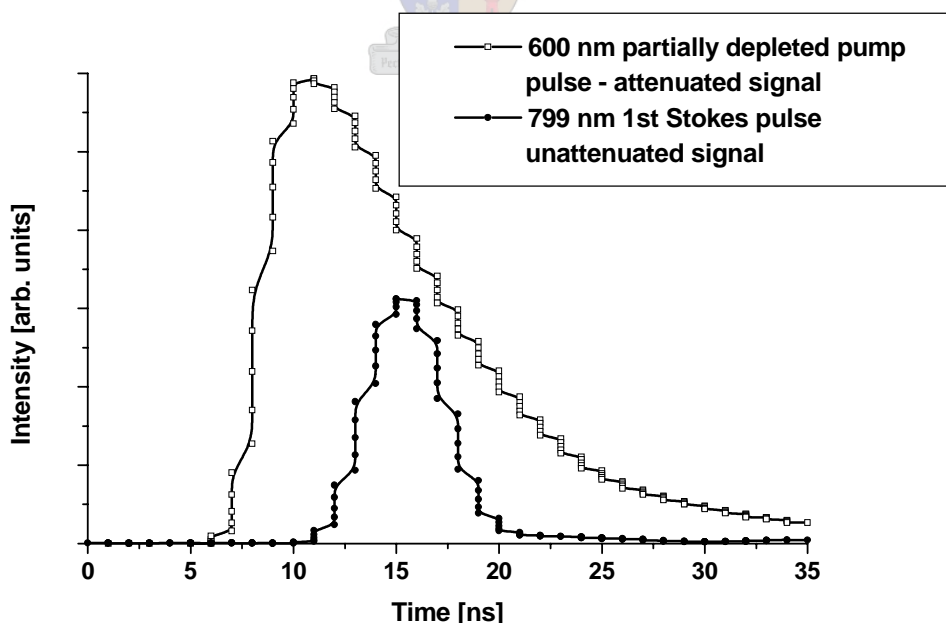


Figure 5.14: Measurements of the temporal dependence of the first Stokes formation at 799 nm, using the OPPO as pump laser at 600 nm.

#### 5.4.4 Low Stokes output

The difficulty of obtaining sufficient SRS using the OPPO as pump laser was unexpected, since the peak intensities are almost an order of magnitude higher than those of the dye lasers. An example of this difficulty can be illustrated by the following experimental result.

After good alignment of the Raman laser system, an OPPO pulse energy transmitted through the waveguide was found as 4.18 mJ in a 8 ns pulse at 440 nm, with a standard deviation of 0.35 mJ. If this is compared to the experimental specifications of the dye lasers, a large Stokes output is expected. However, using the Laser Precision Corporation energy-meter, the measured Stokes output at 3000 kPa, was less than 50  $\mu$ J. This could not be accurately measured due to the large pulse-to-pulse deviation, resulting in some pulse energies below the minimum detectable energy by the detector. This large pulse-to-pulse deviation is an indication that the process is near the threshold.

The low Stokes output implies a decrease of the Raman gain coefficient. This decrease may be attributed to the fact that the bandwidth of the OPPO is very large, 6 – 8  $\text{cm}^{-1}$  at 495 nm [24]. The dependence of the Raman gain coefficient on the bandwidth is discussed in Section 4.2.2, where the acceptance bandwidth is defined in Equation 4.3. As mentioned, an accurate calculation of the acceptance bandwidth for the Raman laser was not done, but the value of 4.9  $\text{cm}^{-1}$  mentioned in [20] may be used as a comparative value. It can be seen that the OPPO bandwidth is larger than this value, which results in the low gain coefficient. It should be mentioned that the bandwidth of the dye lasers are in the range 0.02 – 0.1  $\text{cm}^{-1}$  [25], depending on the wavelength.

The bandwidth of the frequency-tripled Nd:YAG laser at 355 nm, is 0.003  $\text{cm}^{-1}$  when the oscillator is injection seeded [26]. Using this system, similar pulse energies as the OPPO output could be applied to the Raman laser. This configuration is investigated in the next section. The positive results obtained using the Nd:YAG laser supports the bandwidth argument as discussed above.

## 5.5 Nd:YAG at 355 nm

### 5.5.1 Experimental conditions

The frequency-tripled output of the Nd:YAG laser at 355 nm, which is used to pump the OPPO, was used directly after transmission through the OPPO system, in the absence of the OPPO resonator windows. Measurements were taken with three different incident energy values: 1, 1.5 and 3 mJ. These energy values correspond closely to the values used in previous experiments, and refer to the values after waveguide transmission. The different pulse energies are chosen by adjusting the Q-switch delay of the Nd:YAG laser. Considerably higher energies than those used in this investigation are possible, but the possibility of optical damage to the Raman cell windows and the Laser Precision energy probe limited these energy values.

The different orders of Stokes were separated by a diffraction grating. The different wavelengths which are observable after separation by the grating can be seen in Figure 5.15. The grating considerably attenuates the signal, and this attenuation is also wavelength-dependent. Thus, the relative energy values for the different orders of Stokes are not directly comparable. Nevertheless, the results are useful and good conclusions may be made about the SRS process. Measurements were made of the first three orders of Stokes, which corresponds to  $\lambda = 416, 504$  and 637 nm, refer to Equation 4.4.

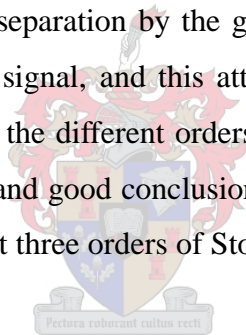




Figure 5.15: Photograph of Raman laser operation using the frequency-tripled Nd:YAG. Three orders of Stokes are visible, as well as the fluorescence of the 355 nm pump.

### 5.5.2 Pressure dependence

The pressure dependence of the Stokes formation was investigated for three different incident laser energies. The Stokes energy dependence on pressure, due to a pump energy of 1 mJ per pulse is given in Figure 5.16. The formation of third order Stokes was visually observed, but this was very near the threshold and not stable enough for a good measurement. In the figure, the growth of the first Stokes is seen, similar to before, and this reaches a peak value. The second Stokes starts to grow at a higher pressure, and it can be seen that this process starts to deplete the first Stokes signal. The fact that both the first and second Stokes remain almost constant at higher pressures is an indication of the competition in the four-wave mixing processes.

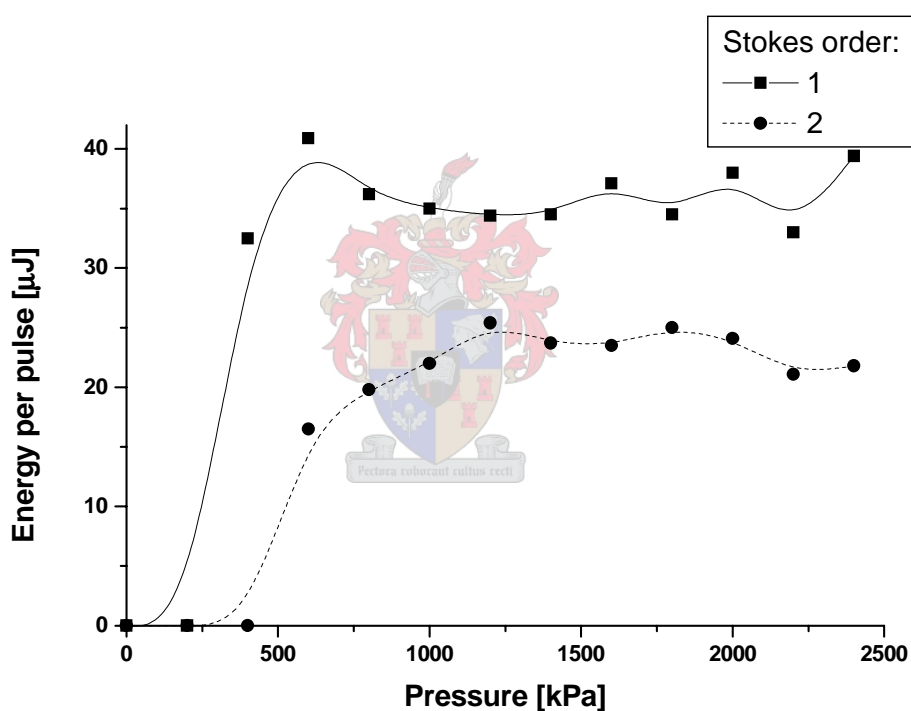


Figure 5.16: Measured Stokes energy as a function of pressure: 1 mJ incident energy.

The measured pressure dependence due to a pump energy of approximately 1.5 mJ is given in Figure 5.17. The peak of the first Stokes is not seen, because it is below 200 kPa, which was the lowest pressure at which measurements were taken. It can also be deduced that this peak will be more critically dependent on the pressure. The partial depletion of the first Stokes and corresponding growth of the second Stokes is observed. The partial depletion of the second Stokes and the corresponding growth of the third Stokes is also observed. Similar to above, the third Stokes signal does not drop, but remains almost constant, due to four-wave mixing effects.

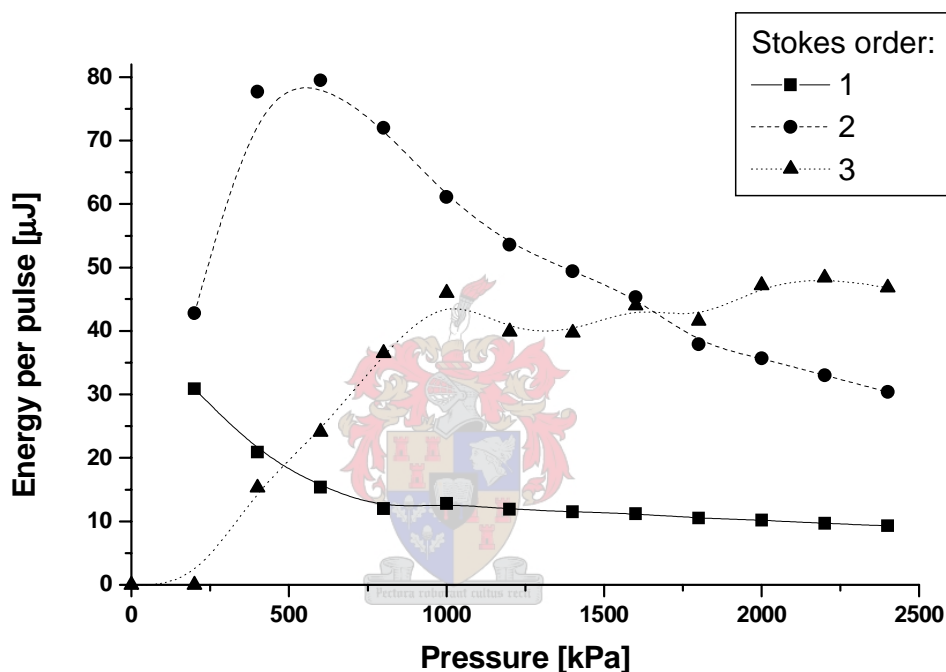


Figure 5.17: Measured Stokes energy as a function of pressure: 1.5 mJ incident energy.

The Stokes-formation pressure dependence due to a pump energy of approximately 3 mJ per pulse is given in Figure 5.18. The first Stokes peak is again not observed, because it lies between 0 and 200 kPa. The partial depletion and growth of the different orders of Stokes is again observed.

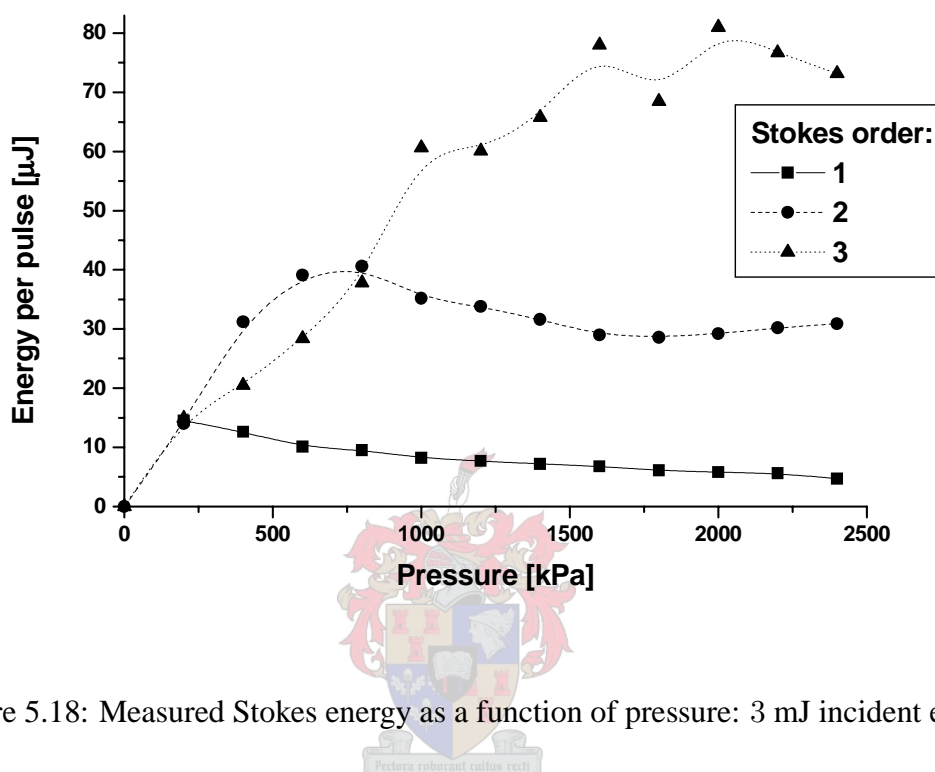


Figure 5.18: Measured Stokes energy as a function of pressure: 3 mJ incident energy.

The results of this investigation of pressure dependence supports the results found with the dye laser systems. In every different experimental situation, an optimal pressure value exists for the generation of a specified order of Stokes. These optimal pressure values are different in different situations, due to the various factors influencing the Raman gain coefficient.

## 5.6 Raman laser conclusions

For the purposes of characterization of the Raman laser system for use as a tunable laser source in the IR, some conclusions can be made from the experimental results.

The use of the dye lasers demonstrated their usefulness as pump sources for the Raman laser. Stokes formation was successfully observed at the available, relatively low, dye laser energies. The optimal conversion efficiency for the dye laser at 440 nm was found to be approximately 30 – 35 % for the first Stokes, and approximately 20 % for the second Stokes. The optimal conversion efficiency for the dye laser at 540 nm was approximately 20 %. The reasons for the lower conversion in the latter case are the lower pulse energies and the longer wavelength, both of which decrease the Raman gain factor.

The two experimental systems above both reach the 694 – 696 nm wavelength range, either by first or by second Stokes formation. This has been discussed in Section 4.3.4. The conversion efficiency is similar in the two cases, yielding slightly higher pulse energies ( $\sim 350 \mu\text{J}$ ) at 694 nm due to second Stokes formation from the dye laser at 440 nm. This is in comparison to the  $\sim 260 \mu\text{J}$  at 696 nm, due to first Stokes formation from the dye laser at 540 nm. This is not a general result, and the relative efficiency of achieving a chosen wavelength by different orders of Stokes should be investigated experimentally.

The pressure dependence of the Stokes output shows a definite optimal pressure value for each of the Stokes orders. This demonstrates the fact that, in a given experimental system, the pressure should be the control parameter for selection of a certain Stokes order, for optimal conversion to a certain wavelength. It was also found that the peak pressure values are different in every situation, requiring an experimental investigation for a given system.

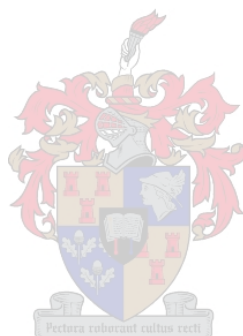
It was found that the SRS process has a threshold value. This threshold value is dependent on the gain factor and will differ for different experimental situations. It was found that stability of the Raman laser output requires operation sufficiently above the threshold value.

Although sufficiently large outputs in the IR were not directly demonstrated, this was due to a lack of current application in the IR, and such a conversion may easily be done using the principles applied in this thesis. Using similar systems, quasi-continuous tunability has been demonstrated from 700 nm to  $7 \mu\text{m}$ , using dyes in the region of 550 – 720 nm [14].

The use of the OPPO as pump source for the Raman laser unexpectedly showed low Raman conversion. The Stokes output had extremely low energy ( $< 50 \mu\text{J}$ ) and was unstable (large pulse-

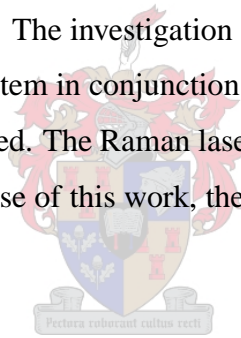
to-pulse deviation), which means that the system is near the threshold for the SRS process. This was unexpected, due to the higher peak intensities of the OPPO output. The reason for the low efficiency of the process was found to be the relatively large bandwidth of the OPPO output, which lowers the gain factor significantly. Use of the OPPO may be shown to be more practical when it is operated with a dye laser seed, which narrows the bandwidth to  $1.8 \text{ cm}^{-1}$  [24].

Use of the frequency-tripled Nd:YAG laser demonstrated some characteristics of the SRS process, and some conclusions may be made about the pressure and intensity dependences. As before, optimal pressure values were observed for the different Stokes orders. A general conclusion which may be made is that the peak shifts towards lower pressures for higher incident pulse energies. The position of the peak also becomes more critically pressure-dependent. It is shown that, for a given system, the optimal pressure for each Stokes order should be found before the system may be used most efficiently.



# Conclusions

In the work done in this thesis, three beam shaping devices were investigated and characterized as far as possible, using numerical, analytical and experimental methods. The analytical investigation of focussing of a Gaussian beam led to the description of an experimental method suitable to change the focussed waist size by small amounts. This was experimentally applied to the waveguides. The DOE under investigation was numerically modelled and the sensitive parameters were identified. This allows more efficient use of the DOE in an experimental situation. Various waveguides were experimentally investigated as beam shaping devices. This resulted in the discovery of the most efficient alignment techniques. The waveguide was used efficiently as beam shaping device in the Raman laser system. This system was applied successfully to generate tunable laser radiation at shifted wavelengths. This was achieved with the relatively low pulse energies of the available dye lasers. Various aspects of the design and parameters for the effective use of the system has been identified. The investigation of an OPPO as pump source did not yield positive results, but the use of the system in conjunction with the Raman laser is still viable, if the OPPO is operated with a dye laser seed. The Raman laser has therefore been characterized for use with the available sources, and because of this work, the system will easily be applied to generate tunable IR in the future.



# Bibliography

- [1] H. Kogelnik and T. Li (1966). *Laser beams and resonators*, Applied Optics **5** no. 10, p. 1550.
- [2] Peter W. Milonni and Joseph H. Eberly (1988). *Lasers*. John Wiley and Sons.
- [3] E.G. Rohwer (1994). *Development of an infrared laser system for molecular isotope separation*. Ph.D. Thesis, Department of Physics, University of Stellenbosch.
- [4] Russell L. McCally (1984). *Measurement of Gaussian beam parameters*, Applied Optics **23** no. 14, p. 2227.
- [5] Hans Peter Herzig - editor (1997). *Micro-optics: Elements, systems and applications*, Chapter 3: *Binary Optics Fabrication* by M.B. Stern. Taylor and Francis Publishers.
- [6] Markus Rossi and Jyrki Saarinen (2002). *Replication of micro-optics is cost-effective*. Laser Focus World supplement: Nontraditional Optics, August 2002.
- [7] Joseph W. Goodman (1968). *Introduction to Fourier Optics*. McGraw-Hill Publishing Company.
- [8] Max Born and Emil Wolf (1975). *Principles of Optics*, Fifth edition. Pergamon Press.
- [9] Anton du Plessis (2002). *Optical modelling using diffraction theory*. M.Sc. Seminar, Department of Physics, University of Stellenbosch.
- [10] J.A. du Plessis (1992). *Spectral characteristics of stimulated Raman scattered radiation in a waveguide*. M.Sc. Thesis, Department of Physics, University of Stellenbosch.
- [11] John J. Degnan (1973). *Waveguide Laser Mode Patterns in the Near and Far Field*, Applied Optics **12** no. 5, p. 1026.
- [12] J.P. Crenn (1982). *Optical theory of Gaussian beam transmission through a hollow circular dielectric waveguide*, Applied Optics **21** no. 24, p. 4533.
- [13] P. Rabinowitz, A. Kaldor, R. Brickman and W. Schmidt (1976). *Waveguide H<sub>2</sub> Raman laser*, Applied Optics **15** no. 9, p. 2005.
- [14] W. Hartig and W. Schmidt (1979). *A broadly tunable IR waveguide Raman laser pumped by a dye laser*, Appl. Phys. **18**, p. 235-241.

- [15] Eugene Hecht (1998). *Optics*, Third Edition. Addison Wesley Longman.
- [16] Guang S. He and Song H. Liu (1999). *Physics of nonlinear optics*. World Scientific Publishing Company.
- [17] Amnon Yariv (1975). *Quantum electronics*, Second Edition. John Wiley and Sons.
- [18] K. Sentrayan, L. Major, H. Bryant, A. Michael and V. Kushawaha (1992). *Laser wavelength, pressure and temperature dependence on the stimulated Raman scattering gain in H<sub>2</sub>*, Spectroscopy Letters **25** no. 5, p. 627.
- [19] William K. Bischel and Mark J. Dyer (1986). *Wavelength dependence of the absolute Raman gain coefficient for the Q(1) transition in H<sub>2</sub>*, J. Opt. Soc. Am. B **3** no. 5, p. 677.
- [20] W.R. Trutna Jr, Y.K. Park and R.L. Byer (1979). *The dependence of Raman Gain on Pump Laser Bandwidth*, IEEE Journal of Quantum Electronics **QE-15** no. 7, p. 648.
- [21] Nikolai B. Delone and Vladimir P. Krainov (1988). *Fundamentals of nonlinear optics of atomic gases*, A volume in the Wiley Series in Pure and Applied Optics. John Wiley and Sons.
- [22] [www.korth.de](http://www.korth.de), Korth Kristalle GMBH.
- [23] *Fax communication* between UGK Deutschländer of the University of Stellenbosch and Carmine Amelio of Laser Precision Corporation, June 29 1988.
- [24] *OPO Broadband operation - bandwidth*, Lambda-Physik specifications manual.
- [25] Lambda-Physik FL2002 *Dye laser Operator's manual*.
- [26] *Operation and maintenance manual for the Powerlite 8000 Series laser*, Continuum, 1993.

## Appendix A

### Gaussian beam terminology

A Gaussian beam can be described by its transverse intensity profile, which is given by:

$$I(r) = \frac{c\epsilon_0}{2} |A|^2 \frac{w_0}{w(z)} e^{-2\frac{(x^2+y^2)}{w^2(z)}}$$

In this relation,  $w(z)$  is the beam spot size. This beam spot size is defined as the beam radius at  $\frac{1}{e^2}$  of the peak intensity, as illustrated in Figure 5.19. In this thesis, the concept of beam spot size is simply referred to as the beam size<sup>16</sup>.

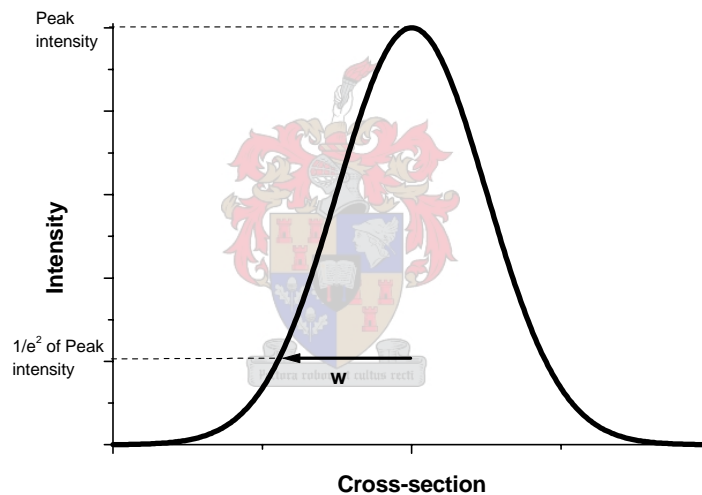


Figure 5.19: Illustration of Gaussian intensity profile and the beam size  $w$ .

Gaussian beams have the unique characteristic that the transverse profile remains Gaussian on propagation through free space. The propagation of a Gaussian beam is illustrated in Figure 5.20. The narrowest part of the Gaussian beam is the beam waist, denoted by  $w_0$ . The usual convention is to choose  $z = 0$  at the waist position. This figure also shows the Rayleigh Range  $z_0$ , which is a measure of the waist region, such that  $w(z_0) = \sqrt{2}w_0$ .

<sup>16</sup> Some beam propagation texts refer to the beam radius at  $\frac{1}{e}$  of the peak intensity, denoted by  $r$ . This can easily be shown to relate to the beam size as follows:  $w = \sqrt{2}r$ . [4]

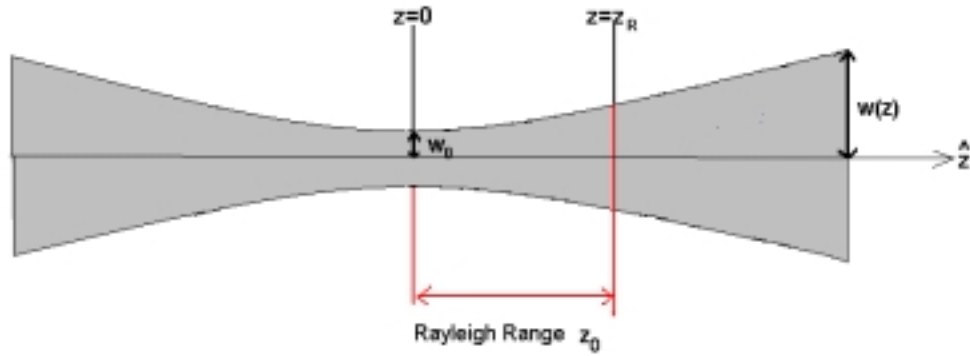


Figure 5.20: Schematic illustration of the Gaussian beam parameters.

According to the Gaussian Beam Solution of the Paraxial Wave Equation, the free-space propagation of a Gaussian beam may be described very simply by the following relations [2]:

$$w(z) = w_0 \sqrt{1 + \frac{z^2}{z_0^2}} \tag{A.1}$$

$$z_0 = \frac{\pi w_0^2}{\lambda} \tag{A.2}$$

The intensity profile of a super-Gaussian of the  $n$ th order, with peak intensity equal to unity, is given by:

$$I(r) = e^{-2 \frac{x^2 + y^2}{w^2(z)}} \tag{A.3}$$

The beam quality of a laser beam is quantified by the beam quality factor, or  $M^2$  value. An ideal Gaussian beam has a beam quality factor of  $M^2 = 1$ . Any deviation from the Gaussian beam propagation is quantified by the beam quality factor, which is related to the given beam size  $W$  and the corresponding Gaussian beam size  $w$  as follows:

$$W = Mw$$

It should be noted that beam quality factors are such that:

$$M^2 \geq 1$$

## Appendix B

### Scanning slit measurement

The transverse intensity profile of a laser beam may be measured by scanning a narrow slit across the beam. In the paper by R.L. McCally [4], it has been shown that power measurements across the beam profile directly yield the Gaussian intensity profile. This paper also shows that relatively large slit widths give extremely accurate results. According to this paper, a slit width of  $\frac{1}{7}$  of the beam size  $w$  gives the beam size to an accuracy of 0.083%.

Since the beam size is the parameter to be measured, the necessary slit width will not always be known beforehand. For this reason, a qualitative rule is applied: if the measured profile becomes flattened at its peak, this is most likely due to a slit width which is too large. A slit width which is too small causes a diffraction pattern instead of the Gaussian transverse profile. These two extreme cases can easily be distinguished from the correct profile.

The experimental setup used for the profile measurements of the Helium-Neon laser in this thesis is identical to that given in [10]. A photodiode detector, which measures the incident power, is placed behind a narrow slit and the slit is scanned transversely across the beam.

In the case of beam profile measurements of pulsed lasers in this thesis, the energy per pulse was measured with the Laser Precision Corporation Rj-7620 energy-ratiometer and the RjP-735 energy probe. Averaged measurements were taken, in most cases over 100 pulses, by the average function of this energy meter. In the process of the scanning slit method, the energy per pulse passing through the slit was measured. This profile measurement yields the intensity profile, assuming no change of the intensity profile during the pulse duration.

## Appendix C

### Phase profile calculation

The phase profile of a Gaussian beam is given by:

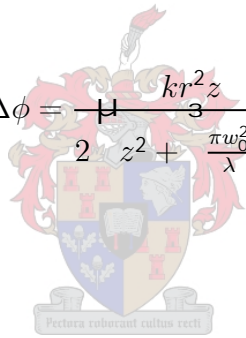
$$\phi = k \frac{r^2}{2R(z)} + kz - i\eta$$

Where:

$$R(z) = \frac{1}{z} \left[ z^2 + z_0^2 \right] \text{ is the radius of curvature of the wavefront}$$

$$\eta = \arctan \frac{z}{z_0} \text{ is the Guoy phase shift}$$

Since the Guoy phase shift is independent of radial coordinate, it may be ignored in this investigation. Similarly, the  $kz$  term may be ignored. Using Equation A.2 the following description of the phase profile may be found:

$$\Delta\phi = \frac{kr^2z}{2 \left[ z^2 + \frac{\pi w_0^2}{\lambda} \right]}$$


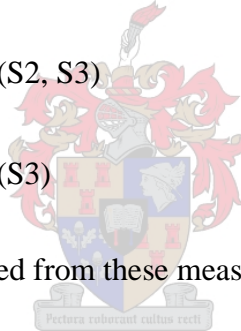
## Appendix D

### Use of Schott cutoff filters

During the experiment using the dye laser at 440 nm as the pump for the Raman laser, suitable filters for the ideal separation of the different orders of Stokes were not available<sup>17</sup>. Such an ideal situation would involve the following process (fourth and higher Stokes formation is neglected):

*The notation below is as follows: P - pump at 440 nm; S1 - first Stokes at 538 nm; S2 - second Stokes at 694 nm; S3 - third Stokes at 974 nm.*

1. Measurement of entire signal: (P, S1, S2, S3)
2. Measurement with ideal filter 1: (S1, S2, S3)
3. Measurement with ideal filter 2: (S2, S3)
4. Measurement with ideal filter 3: (S3)



The desired data can be extracted from these measurements as follows:

1.  $P = (P, S1, S2, S3) - (S1, S2, S3)$
2.  $S1 = (S1, S2, S3) - (S2, S3)$
3.  $S2 = (S2, S3) - (S3)$
4.  $S3 = (S3)$

The available filters which were used are:

- GG10 filter: Approximate transmission: 20% of P, 100% of S1, 100% of S2, 100% of S3<sup>18</sup>

<sup>17</sup> Cutoff filters allow transmission of higher wavelengths but not lower wavelengths.

<sup>18</sup> This is not entirely correct, but a necessary assumption in order to separate the given wavelengths.

- OG570 and RG610 filter: Transmission only for S2 and S3 at  $\sim 100\%$

The measurements taken were:

1. Measurement 1: Entire signal (no filters).
2. Measurement 2: Use of GG10 filter.
3. Measurement 3: Use of OG570 and RG610 filters together.

The separation was done as follows:

1.  $P = (\text{Measurement 1} - \text{Measurement 2})/0.8$
2.  $S1 = \text{Measurement 2} - \text{Measurement 3} - (0.2 * P)$
3. S2 and S3 could not be separated

The above-mentioned method was the general method of separating the wavelengths in this experimental situation. Although not an entirely accurate method, this was the best possible method with the available apparatus. It should therefore be noted that the absolute pulse energies have a reasonable degree of inaccuracy in this case.